Republic of Iraq
Ministry of Higher Education
and Scientific Research
University of Babylon
College of Engineering
Electrical Engineering
Department

Accurate Self-Calibration Techniques for Micro-Electro-Mechanical System

A Thesis
Submitted to the College of Engineering / University of Babylon
in Partial Fulfillment of the Requirements for the Degree of Doctor of Philosophy in Engineering / Electronics and communications

By

Anwer Sabah Ahmed Shayal

Supervised by

Prof. Dr. Qais Al-Gayem

2023 A.D **1445 A.H**

ABSTRACT

The zero-bias error and scale-factor error of a Micro-Electro-Mechanical System (MEMS) and Nano-Electro-Mechanical System (NEMS), are caused by technical flaws and aging. The inertial navigation system's accuracy could be substantially harmed by raw readings without calibration. To use a MEMS triaxial accelerometer, self -test and calibration processing is therefore required.

These systems need to be produced with high reliability to achieve the required task that was made for it. Therefore, the self-test and calibration became an important issue for researcher. In this work, the design, simulation, and hardware implementation of a built-in self-test and calibration of three algorithms are suggested and presented for the purpose of the calibration to compensate for the errors and faults in the MEMS and NEMS. These three proposed suggested algorithms are carried out using the COMSOL Multiphysics software in conjunction with MATLAB. The practical continents were taken through the Arduino and MPU6050 sensor, which was programmed in the C language.

The first proposed algorithm used Akima interpolation to make the imperfect readings from the sensing element closer to the compensated readings computed by GA and saved in the lookup table. The key to this algorithm is the piecewise function, which is a set of polynomials with degrees no greater than three that may be applied to increasingly bigger intervals between the given points. Using this technique, the scale factor calibration errors are 0.41%, 0.42%, 0.43% for X, Y, Z axes respectively, while the bias errors are 0.026, 0.025, 0.024 for the X, Y, Z axes respectively. The bias stability is 2.216 µg, 2.22 µg, and 2.23 µg for X, Y, Z axes respectively.

The second proposed calibration algorithm employed Akima interpolation in conjunction with the Sigma-Delta Modulator (ΣΔ) for the digital interface. The principle of the oversampling is employed for the purpose of the noise sources removing that related to the sensing element and the quantization circuit. These sources are the Brownian noise, resulting from the random motion of material particles in the proof mass and sensing fingers, amplification, switching, and quantization to improve the quantizer's effective resolution employed in this method. This system takes in an analogue signal and outputs it as a digital signal, which is discrete. Antialiasing filtering, sampling hardware, and a quantizer make up the bare minimum. Using this technique, the scale factor calibration errors are 0.32%, 0.33%, 0.31% for X, Y, Z axes respectively, while the bias errors are 0.011, 0.014, 0.012 for the X, Y, Z axes respectively. The bias stability values are 1.34 µg, 1.23 µg, 1.12 µg for X, Y, Z axes respectively.

The third algorithm based on the Kalman Filter (KF) with modification to obtain the Transformed Unscented Kalman Filter (TUKF) for the three axes accelerometer MPU6050 with the triangulation on the output to get the best stability output for the X, Y, Z axes. The transformed Kalman filter has been employed in addition to the Delaunay triangulation to be as a tracker for the three axes accelerometer. The bias and noise are well removed with good stability. Practical results were read using Arduino microcontroller from the MPU6050 accelerometer in the temperature range from (-15^{o} C) to (80^{o} C) which gave the robustness of the algorithm used to show the effectiveness of this method. Using this technique, the scale factor calibration errors are 0.22%, 0.24%, 0.26% for X, Y, Z axes respectively, while the bias errors are 0.017, 0.0115, 0.014 for the X, Y, Z axis respectively. The bias stability is 0.116 µg, 0.12 µg, 0.18 µg for X, Y, Z axes respectively.

As it can be seen that the third algorithm (using TUKF) is the best with respect to the results of the bias errors and the bias stability.

ACKNOWLEDGMENT

I would like to thank the family of the Electrical Engineering department at the University of Babylon especially my supervisors Prof. Dr. **Qais Al-Gayem** for their patience, support, and valuable guidance. This thesis wouldn't have been possible without the priceless supervision of Prof. Dr. **Qais Al-Gayem**.

I would also want to send my heartfelt estimate to all my **teachers** in the Electrical Engineering department for their invaluable advice that opened the knowledge gates for me, and enriched my thinking capabilities.

I would like to express my deepest gratitude to my mother and wife, **Wisal**, for their huge support, which provided the necessary support to finalize this work.

Also, special thanks go to all my dear friends, especially my friend **Mohanned Al-Jaafery**, for his invaluable assistance.

TABLE OF CONTENTS

1 Abstract i

2 Acknowledgment iv

3 Table Of Contents v

4 Table Of Figures ix

5 List Of Tables xiii

6 List Abbreviations xiv

7 List Symbols xv

1 Chapter One: Introduction 1

1.1. Introduction 1

1.2. Definition of Micro-Electro-Mechanical System (MEMS) 1

.1.3 Literature Review 4

1.4. Problem Statement 13

.1.5 Research Objectives 13

1.6. Research Main Contribution 14

1.7. Dissertation Organization 15

1.8. Publication 15

2 Chapter Two: The Theory of The Mechanical Sensing Element and Self-Test Methods 17

2.1. Introduction 17

2.2. Sensing Mechanical Element 17

2.3. Sensing Element Design 20

2.4. Capacitive Accelerometers 27

2.5. Self-test and calibration methods 31

2.6. Capacitive test 32

2.6.1. Capacitor Network Model 32
2.6.2. Charge Control 34
2.7. Capacitance to frequency 41
2.7.1. Pierce oscillator 41
2.8. Electrical Stimulus 44
2.8.1. Direct parameter extraction 44
2.9. Capacitance to voltage 50
2.10. Estimation 51
2.10.1. Least squares 52
2.10.2. Maximum Likelihood 54
2.11. Filtering 57
2.11.1. Kalman filter 57
2.11.2. Kaiser filter 58
2.12. Neural networks 59
3 Chapter Three: The Proposed Self-Test and Calibration Algorithms 62
3.1. Introduction 62
3.2. Definition of the MEMS Sensor Model 65
3.3. Scaling of The NANO Sensing Element 68
3.4. Failure Mechanism 69
3.5. Compensation Voltage Calculation By GA 71
3.6. Method (1): Akima Interpolation Based 74
3.7. Interpolation of Akima with Modifications 79
3.8. Method (2): A Sigma-Delta Modulation Based 80
3.8.1. Method Description 81
3.8.2. Second-order ΣΔ Modulator 84
3.8.3. ΣΔ Modulator with High-Order 85
3.8.4. Architecture of Cascaded ΣΔ modulator 86
3.8.5. The Decimation Filter 87

3.8.6. Capacitive ΣΔ MEMS Accelerometer Noise Sources 89
3.9. The Proposed Sigma-Delta Modulator (ΣΔ) System Model 93
3.10. The Method of Calibration 95
3.11. Method (3): Three Axis MEMS Calibration Using Kalman Filter and Delaunay Triangulation Algorithm 95
3.11.1. Method description 96
3.11.2. Transformed Unscented Kalman Filter TUKF Calibration Method 98
3.11.3. Model of Measurement and Process for the Accelerometer 99
3.11.4. Formulation of TUKF 100
3.11.5. Delaunay Triangulation Algorithm 103
3.12. Experiment setup 106
3.13. Chapter Summary 108
4 Chapter Four: Experimental Results, Statistical Analysis and Discussion 110
4.1. Introduction 110
4.2. Sensing Element Dimensions Calculation 110
4.3. Method (1): Akima Interpolation 111
4.3.1. BIST Calculation Using GA 111
4.4. Method (2): Sigma-Delta Modulation 118
4.4.1. Noise removing 118
4.4.2. Fault and Calibration Process 122
4.5. Method (3): Kalman Filter 123
4.5.1. Comparison With Previous Works 130
4.6. Comparison Of The Three Algorithms 133
4.7. Chapter Summary 133
5 Chapter Five: Conclusions and Suggested Future Work 142
5.1. Conclusions: 142
5.2. Suggestions for Future Works 143
6 Appendix A 150

7 References 145

TABLE OF FIGURES

Figure 1-1 The Components of MEMS are Schematically Shown 4
Figure 2-1 The Lumped Parameter Model of an Accelerometer Comprises The Seismic Mass The Spring with The Element of Damping..... 18
Figure 2-2 Analog Force Feedback Displaying The Net Electrostatic Force Applied to The Proof Mass 25
Figure 2-3 An Accelerometer With a Closed Loop and an Analog Force-Feedback 26
Figure 2-4 The Typical Architecture of a Capacitive Surface-Micromachined Accelerometer That Operates in-Plane 30
Figure 2-5 The Categories of The Many Different MEMS Testing Techniques ... 32
Figure 2-6 Topology of The Accelerometers Sensor for: (a) Differential Figuring out Approach With Vertical Set of Experience Combdrive Capacitors; (b) Set of Experience Combdrive Capacitors Diagonal; and (c) In The Modulation Node Group, S_1 and S_8 Have Sensing and Modulatory Functions, Respectively 34
Figure 2-7 A Condensed Version of The Block Diagram That Represents The BIST Architecture..... 35
Figure 2-8 BIST Electronics for Charge Control..... 37
Figure 2-9 The Time-to-Digital Converter (TDC) That is Extremely Straightforward 38
Figure 2-10 Check Setup Chart..... 42
Figure 2-11 Delay Control Using PMOS Transistors M_3 and M_4 42
Figure 2-12 Mapping Response Using Translated Lower Back to an Electrical Sign 45
Figure 2-13 Circuit for Measuring Capacitance 47

Figure 2-14 The Proposed DAC Method Utilized for Excitation Production Signal 50
Figure 2-15 The Structure of The BP Neural Network 60
Figure 3-1 The Proposed Self-Test and Calibration System 63
Figure 3-2 The Process Algorithm Design Steps for the GA-based Methodology . 64
Figure 3-3 Voltage That is Being Sensed Versus Acceleration Applied 66
Figure 3-4 Self-Test Voltage Versus Displacement 68
Figure 3-5 The Dual Axis (X,Y) Sensing NEMS Element 69
Figure 3-6 The Dual Axis (X,Y) Sensing MEMS Element 72
Figure 3-7 The Z Axis Sensing MEMS Element 73
Figure 3-8 A Requirement That Must Be Satisfied in Order to Determine The Angle of a Parallel with The Graph 74
Figure 3-9 Over Shoot of Akima Elimination 80
Figure 3-10 Single -Bit First -Order ΣΔ Modulator (a) General Circuit (b) Linear Circuit 81
Figure 3-11 Architecture of Second-order ΣΔ modulator 84
Figure 3-12 ΣΔ Modulator Cascading Utilizing Third-Order Second-Stage 86
Figure 3-13 Sinc Filter Construction 87
Figure 3-14 Sinc Filter Addition Block 88
Figure 3-15 Sinc Filter Subtraction Block 88
Figure 3-16 Sigma-Delta Modulator of the MEMS Capacitive Accelerometer 94
Figure 3-17 The Triangulation Process Result for TUKF Output 104
Figure 3-18 The Approximation Process for The TUKF Output Point 105
Figure 3-19 Flow Chart of The Akima Interpolation 105
Figure 3-20 The Orientation of The Accelerometer (a) 0^o (b) 30^o 106
Figure 3-21 The Orientation of The Accelerometer (a) 50^o (b) 90^o 107

Figure 4-1 Central Plate Width Calculation 111
Figure 4-2 Sensing Element at No Fault Case 112
Figure 4-3 The Effect of Sensing Fingers Fault on the Output Voltage at Different Cases 114
Figure 4-4 The Effect of Spring Fault on the Output Voltage at Different Cases . 115
Figure 4-5 Sensing Element Resonance Frequency Response Before Calibration Case 116
Figure 4-6 Sensing Element Resonance Frequency Response at Calibration Case 116
Figure 4-7 Autocorrelation of the Error Signal When D=8 119
Figure 4-8 Autocorrelation of the Error Signal When D=12 119
Figure 4-9 Frequency Response of the Quantized Output D = 8 120
Figure 4-10 Frequency Response of the Quantized Output D = 12, ... 121
Figure 4-11 The Spectrum Output of The Sigma-Delta (ΣΔ) Accelerometer for various Finger and Spring Faults 123
Figure 4-12 The Margin of Error for The Linear Acceleration That Was Experimentally Calibrated in One Direction 124
Figure 4-13 Diagram of Data Structure That is Used in The Allan Variance Algorithm 125
Figure 4-14 Allan deviation before applying TUKF algorithm 125
Figure 4-15 Photographs of the experiment setup (a) Inside The Chamber (b) Data Collecting by The Laptop 127
Figure 4-16 Allan deviation after the (TUKF) and the Delaunay Triangulation of the 3-axis (X,Y,Z) 132
Figure 4-17 IMU 0^{o} Orientation 135
Figure 4-18 IMU 10^{o} Orientation 136

Figure 4-19 IMU 20º Orientation.....137
Figure 4-20 IMU 30º Orientation.....138
Figure 4-21 IMU 40º Orientation.....139
Figure 4-22 IMU 90º Orientation.....140

LIST OF TABLES

Table 2-1 Sensing Element Parameters 20
Table 2-2 Discussion Pertains of The Optimization Error with Inputting a Single Tone 48
Table 2-3 Discussion Pertains of The Optimization Error with Inputting a Three Tone 49
Table 3-1 Proposed Calibration Algorithms 62
Table 3-2 Common MEMS Faults 70
Table 3-3 The outline of Transformed Unscented Kalman Filter 101
Table 4-1 Bias Values for The Fingers and Spring Faults 113
Table 4-2 BIST Values Using GA to Minimize the Bias Values 117
Table 4-3 Bias Values Minimization After Akima interpolation 118
Table 4-4 The Values of Signal to Noise Ratio Versus Number of Bits and Pole Value Before Noise Shaping. 122
Table 4-5 The Values of Signal to Noise Ratio Versus Number of Bits and Pole Value After Noise Shaping. 122
Table 4-6 The Collected Data From MPU6050 Sensor Before TUKF Algorithm 126
Table 4-7 The Collected Data From MPU6050 Sensor After TUKF Algorithm .. 128
Table 4-8 Comparison Between The Present Work and The Previous Works 131
Table 4-9 Comparison Between The Three Proposed Algorithms 133

LIST ABBREVIATIONS

ARW	Acceleration Random Walk
BI	Bias Instability
BIST	Built-In Self-Test
BP	Back Propagation
CDS	Correlation Double Sampling
CMFB	Common-Mode Feedback
DNL	Differential Nonlinearity
DUT	Device Under Test
GA	Genetic Algorithm
HARM	High-Aspect-Ratio Micromachining
IC	Integrated Circuit
IMU	Inertial Measurement Unit
KF	Kalman Filter
LS	Least Squares
MEMS	Micro Electromechanical System
ML	Maximum Likelihood
NEMS	Nano Electromechanical System
OSR	Over Sampling Ratio
SNR	Signal to Noise Ratio
TA	Triaxial Accelerometer
TDC	Time-To-Digital Converter
TUKF	Transformed Unscented Kalman Filter
VDL	Vernier Delay Line

LIST SYMBOLS

C_1	Capacitance between fingers
l_e	Electrode length
h_e	Electrode height
A	Electrode area
d_0	Electrode separation
C_T	Total capacitance of proof mass
N_e	Total number of proof mass electrodes
N_{te}	Total number of proof mass test electrodes
L_p	Length of the central plate
k	Spring constant
L_r	Spring length
H_r	Spring height
W_r	Spring width
r	COMSOL structure
d_d	Desired response
Y_n	Compensated sensor output
$\tilde{A}^s$	Accelerometer output
a	Applied acceleration
f_{res}	Resonance frequency

CHAPTER ONE

Introduction

Chapter One: Introduction

1.1. Introduction

This chapter presents an introduction and a definition to the Micro-Electro-Mechanical-System and Nano-Electro-Mechanical System. Structure and components for these systems also presented. Literature review for the previous and most relevant works in the last years in the field of the calibration belongs to these systems. Finally, the problem statement, research objectives, main contribution and organization are presented.

1.2. Definition of Micro-Electro-Mechanical System (MEMS)

Micro-Electro-Mechanical-System (MEMS) and Nano-Electro-Mechanical System (NEMS) are both acronyms for "microelectromechanical system," which is the process name given to a method of production that is utilized in the production of tiny integrated devices or systems that incorporate both mechanical and electrical components. MEMS and NEMS are used interchangeably in this dissertation. They may be as tiny as a few micrometers or as big as millimeters in size and are manufactured using methods that are part of the batch manufacturing method for Integrated Circuits (IC). On a smaller scale, these machines (or systems) have the capability of sensing, control, take action or actuation effect in the scale of micro [1].

Due to the fact that MEMS are interdisciplinary in nature, it is necessary to use the design, engineering, and manufacturing experience of a wide variety of technological domains. In addition to fluid engineering, optics, instrumentation, and packaging, these fields include chemistry, chemical engineering, integrated circuit manufacturing, mechanical engineering, materials science and electrical engineering [2], [3]. Another sign of the complexity of this technology is the wide variety of different businesses and areas of application that make the use of MEMS technologies. MEMS technology has a broad range of potential applications across a

number of industries, such as the automotive, medical, electrical, communication, and military sectors [4], [5]. The accelerometers in airbag sensors are just one example of a modern MEMS device. Other examples include the heads in inkjet printers, the read/write heads in computer disc drives, the chips in projection displays, blood flow sensors, optical equipment switches, microvalves, biological sensors, and many more. Each of these goods is produced in large quantities and distributed to customers on a commercial scale.

It is considered to be one of the most promising technologies for the 21st century. By merging the two distinct areas of research, MEMS have the potential to completely transform the industrial and consumer product sectors. The methods and technologies that are created utilizing it and are based on microsystems have the potential to have a substantial influence on all of our lives. The first revolution in the area of micromanufacturing was the semiconductor microfabrication revolution [6], [7]. The second revolution in the field of micromanufacturing was the microelectromechanical system (MEMS) revolution.

MEMS approach enables the construction of compact devices that integrate both mechanical and electrical components. Integrated Circuits (ICs) can be as large as a few millimeters in size and are produced utilizing batch production procedures. Their dimensions might be ranging from a few micrometers to several millimeters anywhere [6], [8]. These devices or systems possess the capacity to perceive, regulate, and implement actions at the micro level, while simultaneously producing effects at the macro level.

It was within the United States that the acronym MEMS was first introduced. In spite of the fact that different MEMS devices use different language, a MEMS device may be defined by the process by which it is produced. The electronic components

of the device are manufactured using IC technology. On the other hand, the micromechanical components of the device are manufactured through the utilization of micromachining mechanisms, which involve the intricate manipulation of silicon as well as other substrates. Micromachining techniques like bulk machining operations, surface micromachining, but also High-Aspect-Ratio Micromachining (HARM), among others, are applied in the production of mechanical and electromechanical parts and components [9], [10]. These techniques either add new structural layers or remove sections of the silicon in a selective manner. In contrast to integrated circuits, which are intended to take use of the electrical qualities that silicon contains, MEMS is capable of making use of either the mechanical properties that silicon possesses or both its electrical and mechanical capabilities.

A diagrammatic representation of this subject may be seen in figure1-1. Microsensors are able to detect changes in their environment by monitoring information or phenomena relevant with mechanical, thermal, magnetic, chemical, or electromagnetic fields. This allows the microsensors to detect changes in their surroundings. This information is then analyzed by microelectronics, which transmits a signal to the microactuators, directing the microactuators to react and bring about some type of change in the world around them [6], [11]. Micro-electromechanical systems (MEMS) have been initially created in the 1970s, and ever since that time, there has been an increasing demand for the creation of these systems.

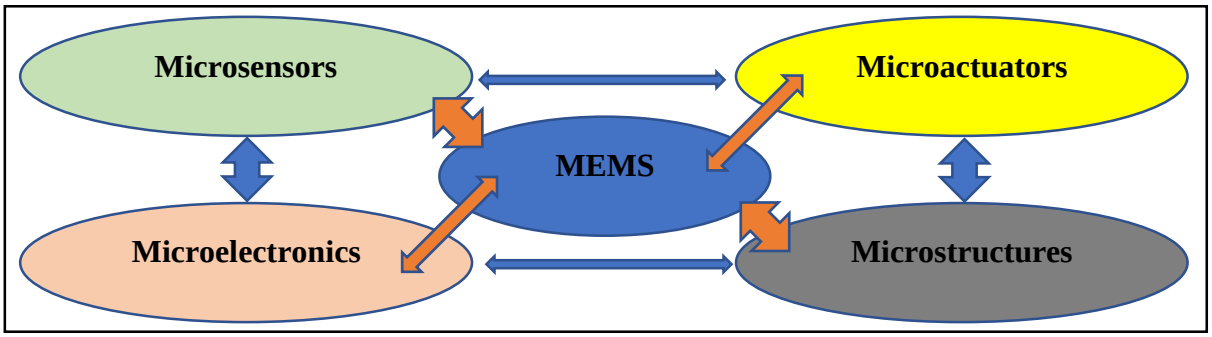

Figure 1-1 The Components of MEMS are Schematically Shown [12]

The wide gap that exists between the projected and actual performances of MEMS has been a persistent and systemic issue. Because of the inherent variability of the manufacturing process, no two MEMS have ever been able to work in an identical manner. It is frequently necessary to calibrate the device in the plant, which can add up to as much as three-fourths of the total cost of production. These kinds of problems provide obstacles for microsensors, which need to have improved precision while still having reduced costs [12].

1.3. Literature Review

Due to the requirement to find calibration algorithms as well as techniques for these systems to address the issues that result after manufacturing and ageing, the problem of microsystem calibration has attracted the attention of a large number of investigators in the fields of control and electronics. In the next section of the chapter, a reasonable number of the strategies and procedures will be discussed that have been used in this context throughout the course of the preceding years.

In 2012 Frosio et al. [13] produced a generic specification that, given certain assumptions, may be reduced to the classic quadratic cost function. The correctness of the technique that has been proposed has been evaluated making use of both simulated data and real data. They demonstrated that the conventional quadratic cost function that is used during autocalibration is a feasible approximation that can be

used to achieve a maximum probability approximate solution of such parameters of a linear detection modelling of a MEMS accelerometer. This was carried out by demonstrating that this function can be used. In addition, the results of the experiments demonstrated that automated model selection could be effectively carried out by using Akaike Information Criterion AIC.

In 2013 Gietzelt et al. [14] came up with a non-iterative calibration method for accelerometers. The method was designed with an emphasis on having a low execution time and using a little amount of memory. The secondary objective is to examine and contrast various calibration techniques that are based on 3D ellipsoid fitting. They examined the execution speeds of the algorithms, as well as the accuracy of the calibrations, and the number of quasi-static tests that are necessary for a valid calibration. Moreover, this approach has been successfully implemented on a sensor node, and it records the measurement results on a micro-SD card in a continuous fashion while simultaneously calibrating the collected data on the fly.

In 2014, Kim et al. [15] developed an accurate calibration methodology that effectively simulates accelerometers with gyroscopes in inertial measurement devices. This concept incorporates a range of error variables to enhance accuracy. The error variables encompassed in their study are bias, sensitivity, coning angle, and azimuth angle. The process of calibrating accelerometers and gyroscopes entails the utilization of non-linear Gauss-Newton regression methodology. Both modelling and testing of a high precision 2-axis rotation gimbal motion system are utilized to illustrate the usefulness of the recommended calibration procedures.

In 2015 Jafari et al. [16] proposed a new calibration approach for Skew Independent Inertial Measuring Units (SRIMUs) that makes use of micro mechanical systems. The comprehensive picture of an SRIMU measurement is constructed

through the process of taking into consideration the consequences of bias, scale factor errors, along with misalignments. In order to achieve a higher level of precision, the calibration procedure models and adjusts for the effect that the accelerometers' lever arms have on the table's center. Two separate Kalman Filters (KFs) are compared and contrasted for the purpose of determining the error parameters of accelerometers and gyroscopes. A technique known as Prediction Error Minimization (PEM) chaotic modelling is used in order to concurrently simulate the influence of bias instabilities with randomness noise just on calibrating Kalman filters. This is carried out in order to limit the number of estimates that are incorrectly biased.

In 2015 Fei, H. et al. [17] investigated an experimental employing the Allan variance technique. The objective of this study was to examine five prevalent variations of MEMS gyroscopes, utilizing the auto CRG20 MEMS gyro testing platform as the primary tool for experimentation. The theory, which is built on time-series data, is used to construct the equation that describes the state of the system. Allan variance study show that the discrete Kalman filter is capable of successfully reducing the signal's noise while improving the stability and reliability of MEMS gyros is when discrete Kalman filter is introduced and contrasted with a basic filter order filter. This conclusion was reached after comparing the discrete Kalman filter to a basic filter order filter. Comparing to this dissertation work, this dissertation work used the Transformed Unscented Kalman Filter (TUKF) which gives better results in terms of stability bias stability and Acceleration Random Walk (ARW).

In 2016, Xin Lu et al. [18] proposed a technique for accelerometer calibration that relied on maximum likelihood estimate. This approach was based on maximum likelihood estimation. It does this by first correcting for the inaccuracies described

earlier, then establishing its alignment between the axis of the accelerometer and the inertial sensor. Since it produces a calibration procedure that does not need any specialized equipment, the method is very user-friendly. For the purpose of determining whether or not the proposed strategy is useful, they employed a sensor-based experiment that is relatively inexpensive as well as numerical simulation.

In 2017 Ye et al. [19] conducted research on the autocalibration of the a Triaxial Accelerometer (TA) for use in MEMS. Firstly, a six-point experimental approach was proposed for a one-of-a-kind six-parameter second-degree model, as well as its G-optimality has been determined using the most effective Design of Evaluation (DoE) that is available. Using a novel linearization approach, the TA model including autocalibration could be condensed into the predicted second-degree form. This makes it possible to employ the indicated optimum experimental strategy. It is also advised to use an iterative strategy that guarantees convergence in order to properly estimate the model parameter. The results of the experiment that were intended make it abundantly evident that the calibrating approach that was recommended is both effective and precise.

In 2019 Mundla Narasimhappa et al. [20] introduced a theoretical framework that is adaptive and robust, which serves as the foundation for the development of the Modified Sage Husa Adaptive Robust Kalman Filter (MSHARKF). The MSHARKF algorithm incorporates a novel adaptive scale factor within the Adaptive Robust Kalman Filter (ARKF) algorithm, resulting in modifications to the state of the ARKF algorithm following each iteration. MSHARKF is implemented in the measurements of the MEMS IMU in order to reduce the amount of random noise and drift inaccuracy. The Allan Variance analysis reveals that the raw data from MEMS

Inertial Measurement Units (IMUs) is primarily affected by two significant sources of random noise, namely Angle Random Walk (ARW) and Bias Instability (BI).

In 2019 Sheng et al. [21] presented a technique for an upgraded wavelet threshold de-noising coupled with something similar to a gradient Radial Basis Function (RBF) neural network, with the intention of better correcting mistakes based on the indoor inertial navigation system. In order to evaluate the random errors produced by a MEMS gyroscope, they used the traditional wavelet threshold techniques and made use of the Allan variance. After that, they improved the methods and developed a whole new threshold function. The technology seems to function well based on the results of the experiments, which is highly significant for improving the accuracy of indoor inertial navigation that relies on MEMS gyroscopes.

In 2020, Ghanipoor et al. [22] came up with an original approach for calibrating devices by rotating them while employing Inertial Measurement Units (IMUs). A decision was made to develop a generic nonlinear model of the inertial measurement unit (IMU) output, with the aim of incorporating various influences. The influences encompassed in this study comprised of scale factor, biases, lever arm, and misalignment. The utilization of the Transformed Unscented Kalman Filter (TUKF), also known as TUKF, was employed to estimate the error parameters associated with gyroscopes and accelerometers. In order to carry out the calibration procedures, a turntable equipped with three axes was used to provide the input signals. The findings of the experiments demonstrated that applying the suggested technique resulted in an improvement in the dependability of the outputs of the gyroscope and accelerometer by 66% and 63%, respectively, as compared to calibrated signals that were generated to use the least square approach.

In 2020 Li et al. [23] worked to find a solution to the problem of the accelerometer's long-term stability. To mitigate the issue of long-term drift inaccuracy exhibited by accelerometers, there is a growing trend towards the adoption of externally integrated microstructures which generate physical stimulation. The piezoelectric MEMS microvibrator functions as an acceleration stimulus, providing a uniform acceleration for the integrated accelerometer. The analysis of the motion status of the microvibrator is conducted using an optical displacement sensing system. The system consists of a device called a Vertical Cavity Surface Emission Laser (VCSEL) along with photodiodes (PDs). Experimental results have demonstrated that the self-calibrated accelerometer exhibits a level of accuracy below 1.5% when exposed to a 15 g acceleration stimulus.

In 2021 Fu et al. [24] elucidated a technique for calibrating a single-camera Inertial Measurement Unit (IMU) with high precision. This approach closely integrated the visual data from other cameras. Because doing so can minimize the lower constraint on the covariance of the predicted extrinsic parameters, which ultimately improves calibration accuracy, several extra cameras have been specifically included in the monocular surveillance system in order to help with calibration. This is because theory shows that doing so can help improve calibration accuracy. Likewise, they offer two degenerative motion circumstances that affect the calibration precision of the resulting multicamera sensory systems. These circumstances should be avoided whenever possible in practical applications because they have a negative impact on the precision of the calibration. Even more importantly, they explain how an accurate extrinsic calibration has to include at least a certain degree of motion in order for it to be used as a realistic benchmark.

In 2021, Xin Zhang et al. [25] proposed a calibration methodology for low-cost Inertial Measurement Units (IMUs). The nonlinear scale factors of the sensors were effectively calculated in order to achieve this. To obtain data for calibration purposes, it is necessary to manipulate each sensor that is affixed to a rigid object by employing two distinct motion patterns. The first motion pattern tilts and rotates the rigid object, and the second motion pattern positions this same rigid object on a stable platform inside a variety of different orientations. The proposed methodology was subjected to analysis and experimentation, utilizing both artificially generated datasets and real-world data sources. The technique employed in this study resulted in a noteworthy enhancement in performance, specifically a 64.12% improvement in acceleration error and a 47.90% improvement in angular velocity error.

In 2021 Li et al. [26] presented Calib-Net . The proposed methodology employs a rudimentary deeply convolutional neural network to precisely calibrate an affordable inertial measurement unit (IMU). By making use of a mathematical calibration model that has been painstakingly created, Calib-Net is able to give compensatory aspects of gyroscope readings in a dynamic manner. Dilation convolution is the method that Calib-Net employs for the purpose of extracting spatiotemporal characteristics from IMU inputs. They do a quantitative and qualitative evaluation of their proposed system by using datasets that are accessible to the public. The results of the tests indicated that their Calib-Net provides greater calibration performance compared to other methods. Furthermore, the anticipated alignment achieved through the utilization of their Calib-Net is comparable to the outcomes derived by the Visually Inertial Odometry (VIO) system.

In 2021 Zengke Li et al. [27] introduced an improved and resilient filtering technique employing a dual state model, incorporating the chi-square distribution of

the squared Mahalanobis distance. The implementation of an enhanced and resilient Kalman filter has resulted in notable improvements in position gains. Specifically, advancements of 33% and 30% have been attained in the north and east components, respectively. The implementation of the robust filter has resulted in a notable decrease of 57% in the magnitude of azimuth error. Consequently, it can be inferred that the enhanced robust filter holds the potential to offer improved performance. The reduction in azimuth error has been observed in both loosely coupled and tightly coupled systems.

In 2022 Dong et al. [28] proposed a calibration methodology was that relied on the rotational principle and employed a double turntable centrifuge. This methodology aimed to address installation errors and obtain accurate input acceleration values during accelerometer calibration. The purpose of this procedure was to obtain accurate input acceleration during the calibration process of the accelerometer. The pivotal step in the procedure involves rotating the sub-turntable in a manner that aligns with the input axis of the accelerometer perpendicular to the vector representing the centripetal acceleration. Inaccuracies in the angle and radius of the installation were modelled. On the basis of these models, one is able to make precise measurements of the nonlinearity, asymmetry, nonlinearity, scale factor calibration, and static radius.

In 2022 Chen et al. [29] developed a novel error model was for the time measurement of the gyro-asynchronous accelerometer. This was carried out in order to account for how the placement of Pedestrian Navigation System (PNS). This study aims to investigate the impact of asynchronous timing of gyro-accelerometer on pedestrian navigation. In this study, a filtering model is developed to effectively align the asynchronous time of the gyro-accelerometer. Additionally, a systematic

approach is proposed for detecting zero velocity by analyzing the rate of attitude change.

In 2023 Chenguang Wang et al. [30] proposed an accelerometer denoising method based on empirical mode decomposition to remove noise generated during the accelerometer calibration process. Firstly, a new design of the accelerometer structure is introduced and analyzed by finite element analysis software. Then, an algorithm combining EMD and TFPF is proposed for the first time to deal with the noise of the accelerometer calibration process. The reconstruction results show that the algorithm can effectively suppress the random noise generated during the calibration process. The results of spectrum analysis show that EMD + TFPF can effectively protect the characteristics of the original signal and that the error can be controlled within 0.5%.

Inn 2023 Oliver Dürr et al. [31] utilized the Bayesian techniques for the calibration of MEMS accelerometers. These devices have garnered substantial interest in various practical applications and typically require calibration through error-correcting functions. The parameters of these error-correcting functions are determined during a calibration process. However, due to various sources of noise, these parameters cannot be determined with precision, making it desirable to incorporate uncertainty in the calibration models. Bayesian modeling offers a natural and complete way of reflecting uncertainty by treating the model parameters as variables rather than fixed values. In addition, Bayesian modeling enables the incorporation of prior knowledge, making it an ideal choice for calibration. Nevertheless, it is infrequently used in sensor calibration.

As was presented in the previous review, there are problems that have not been addressed in the process of examining and calibrating microsystems, the most

important of which are the high instability, bias error and noise present in these systems.

1.4. Problem Statement

As it became clear from the review that mentioned previous researches, that there are some requirements in order to solve some problems of calibration of the MEMS/NEMS systems that have not been considered so far, such as:

1. The need for the MEMS/NEMS calibration system with less Allan deviation.
2. Developing an algorithm for bias drift and noise compensation of the MEMS/NEMS accelerometer axis.
3. The need to develop microcontroller software for the purpose of stabilizing the output of the sensor and reducing the effect of dynamic disturbance.
4. The need to design a MEMS/NEMS calibration system with minimal complexity and hardware components.

1.5. Research Objectives

The aim of this dissertation is to design a robust and effective self-test and calibration method by making use of the Kalman filter in addition to the Lock-up table and Sigma-Delta modulator interface with a minimum error rate suitable for MEMS/NEMS as summarized below:

1. Utilizing the Akima interpolation algorithm cooperation with the Look-up table for the purpose of treating the malfunction of the MEMS/NEMS sensor resulting from manufacturing defects or the change in its characteristics due to aging.
2. Utilizing the GA for the bias compensation calculation in the case of the error.

3. Developing an algorithm in collaboration with the Transformed Unscented Kalman filter algorithm to compensate for noise generated from heat within MEMS/NEMS.
4. Stabilizing the bias of the MEMS system and recording experimental results for the MPU6050 commercial sensor using Allan deviation for comparison with a number of previous studies in this regard.
5. Design Sigma-Delta Modulator MEMS/NEMS for digital interface with enhanced calibration accuracy utilizing lookup table.
6. Practical implementation of programming algorithms related to Kalman filter and Delaunay Triangulation with Arduino and the MPU6050 3-axis sensor.

1.6. Research Main Contribution

The major contributions of this work within the dissertation can be summarized as below:

1. Design a three axis MEMS/NEMS accelerometer in COMSOL software and study the factory defects effects of the spring and proof mass and take the advantage of the genetic algorithm (GA) to calculate the appropriate proof mass voltage when fault is found.
2. Building an acceleration sensor system in MATLAB for the purpose of simulating the effect of noise and bias.
3. Design a program to implement Kalman filter with triangulation algorithm to be implemented in Arduino microcontroller for the purpose of addressing the instability in the MPU6050 sensor to find the bias instability with the lowest value (0.116 μg) at temperatures between (-15^{o} C) and (80^{o} C).

1.7. Dissertation Organization

This dissertation has been arranged into five chapters and it is explained as below:

- Chapter one: a general introduction to the nature of work in the thesis, MEMS/NEMS, literature survey related to the most known calibration techniques based on various algorithm in the last twenty years, thesis objective and main contribution were presented.
- Chapter two: provides an overview of some of the methodologies for calibrating systems and testing micro electro-mechanical devices, including a classification of built-in self-testing procedures that are really non-intrusive, cost-effective, and mainly non-intrusive during testing.
- Chapter three: provides the description for a number of design methodologies that will be used in the calibration of micro and nano systems.
- Chapter four: illustrates the results of methodologies for self-test and calibration used in micro and nano system.
- Chapter five: in this chapter the conclusions of this thesis are presented and the future research directions are suggested.

1.8. Publication

1- A. S. Ahmed and Q. Al-Gayem, "Micro Accelerometer Built-In Self-Test and Calibration Using Genetic Algorithm and Interpolation Method," in 2022 IEEE International Conference on Semiconductor Electronics (ICSE), 2022: IEEE, pp. 49-52.

2- A. S. Ahmed and Q. Al-Gayem, "Self-test and calibration methods for micro electro-mechanical systems," TELKOMNIKA (Telecommunication Computing Electronics and Control), vol. 21, no. 1, pp. 186-194, 2023.

CHAPTER TWO

The Theory of The Mechanical Sensing Element and Self-Test Methods

Chapter Two: The Theory of The Mechanical Sensing Element and Self-Test Methods

2.1. Introduction

This chapter presents a comprehensive introduction to the MEMS sensing element, including its construction, the accelerometer, and the fundamental techniques utilized in the domains for self-test along with calibration for the micro electro mechanical systems (MEMS). These techniques include capacitively, capacitance to frequency, electrical stimulation, estimate, filtering, and neural networks. In addition, this chapter discusses the MEMS sensing element. The testing and integration for the Micro-Electro-Mechanical Systems (MEMS) Built-In Self-Test (BIST) is notably more complex in comparison to Integrated Circuits (ICs).

2.2. Sensing Mechanical Element

Numerous micromachined accelerometers of varying types have been extensively explored and documented in the academic literature. However, it is worth noting that a significant proportion of these accelerometers exhibit a common mechanical sensing element, as depicted in Figure 2-1: a proof mass that is suspended in space from a reference frame using some kind of mechanical device. In accordance with the second law of Newton, the proof mass will be shifted in the direction of any inertial force that is produced by acceleration [32]. Mathematically speaking, the using the domain of Laplace if all conditions were perfect [33]:

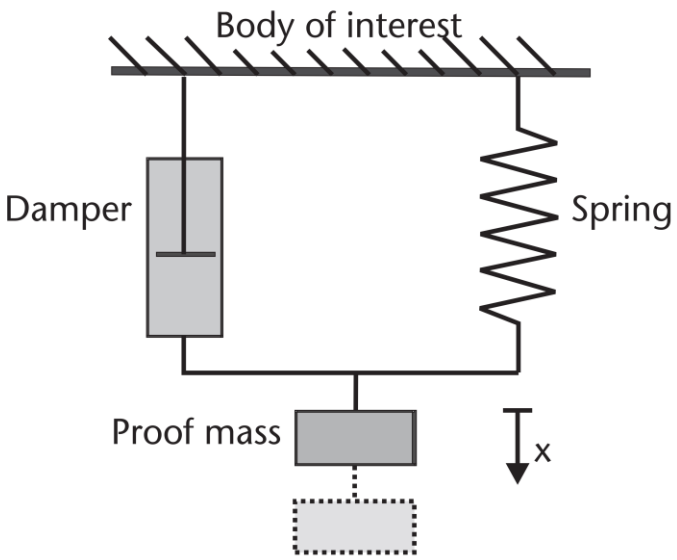

Figure 2-1 The Lumped Parameter Model of an Accelerometer Comprises The Seismic Mass The Spring with The Element of Damping [34]

$$\frac{x(s)}{a(s)} = \frac{1}{s^2 + 2s\omega n^2 + m{\omega_n}^2} \tag{2.1}$$

within the provided context, the symbol *x* is utilized to represent the intended acceleration. The symbol *b* is employed to denote the damping coefficient. The symbol *m* is utilized to signify the mass of the proof mass. The symbol *k* represents the mechanical spring constant of the suspension system. Lastly, the symbol *s* is employed to denote the Laplace operator. The determination of the natural resonant frequency of this system is accomplished by [35]:

$$\omega_n = \sqrt{\frac{k}{m}} \tag{2.2}$$

The open loop sensor sensitivity can be expressed as [36]:

$$S = \frac{m}{k} \tag{2.3}$$

The utilization of an accelerometer at a frequency below its resonant frequency is a common practice. However, it is important to consider a significant design trade-off that arises when sensitivity increases and resonant frequency decreases in relation to the mass-stiffness ratio (*m/k*). The potential trade-off can be partially alleviated by incorporating a sensor component into a closed-loop control system that provides force feedback. The damping factor of an accelerometer plays a crucial role in determining its dynamic performance. In order to achieve optimal bandwidth, it is necessary for the sensing element to exhibit a substantial level of damping. This can be demonstrated by the following equation [37]:

$$b = 2m\omega_n \tag{2.4}$$

The damping observed in micromachined accelerometers is primarily attributed to the motion of the proof mass within a viscous fluid medium. However, it is important to note that the damping coefficient should not be regarded as a constant. Furthermore, it demonstrates a positive correlation with both the displacement linked to the seismic mass as well as the frequency of its oscillation. The subject matter under consideration is frequently denoted as "squeeze film damping" within scholarly discourse [31].

All accelerometers that are micromachined share the common attribute of necessitating the detection of displacement of a proof mass via a position-measuring connection circuit, which is subsequently transformed into a signal of electricity. The position measuring interface has a significant impact on the characteristics and performance of an accelerometer. The main factors include low levels of noise, high levels of linearity, strong dynamic reaction and low consumption of electricity. The ideal situation is the interface circuit should be modelled by an ideal gain block,

which establishes a linear correlation between the displacement of its seismic mass and the corresponding electrical signal [38].

2.3. Sensing Element Design

In this section the design structure of the sensing element MEMS with its simulation will be discussed. The sensing element parameters are as shown in table 2-1:

Table 2-1 Sensing Element Parameters

Description	Value
Test voltage, left side	0[V]
Test voltage, right side	0[V]
Silicon thickness	2[µm]
Oxide thickness	1.6[µm]
Proof mass length	670[µm]
Proof mass width	355[µm]
Number of self- test fingers	3
Number of sense fingers	21
Finger width	4[µm]
Finger length	114[µm]
Finger gap	1[µm]
Self- test finger gap	3[µm]
Self -test finger starting position	3[µm]+(w_f+g_st)
Sense finger starting position	(l_PM-(n_f-1)*3*(w_f+g_f)-w_f)/2

Relative permittivity	4.5
Density	2320[kg/m^3]
Thermal conductivity	34[W/(m*K)]
Coefficient of thermal expansion	2.6×10^{-6}[1/K]
Heat capacity at constant pressure	678[J/(kg*K)]
Young's modulus	160×10^9[Pa]
Poisson's ratio	0.22

Air fills the space between the electrodes (fingers), and the absolute permittivity and vacuum permittivity of air. The capacitance between the electrodes can be calculated as in equation 2.5 [39]:

$$C_1 = \varepsilon \frac{A}{d} = \varepsilon \frac{(l_e)(h_e)}{d}, \qquad l_e = \frac{(C_1)(d)}{(\varepsilon)(h_e)} \tag{2.5}$$

where l_e, h_e, and d is the electrode length, electrode height, electrodes separation respectively.

At rest, a moveable electrode and two fixed electrodes have the same capacitance. The computation of the overall system capacitance between the moving comb and any fixed comb array involves multiplying the capacitance of one capacitor by the number of electrodes were in by each comb *(N_e)* [39]:

$$C_T = (C_1)(N_e) \tag{2.6}$$

While designing the sensing element, state the maximum distance that the moveable mass will travel. One capacitor gains capacitance while the other capacitor gets the lower value as the proof mass advances along the measurement axis.

The system's acceleration should be assessed by measuring this change in capacitance. Equation 2.5 uses the moveable mass displacement (Δd) to calculate the capacitance difference (ΔC_T) [40].

$$\Delta C_T = N_e \varepsilon A \left(\frac{1}{d - \Delta d} - \frac{1}{d + \Delta d} \right) \tag{2.7}$$

The subsequent step entails the computation of the measured proportions that are of the center plate of the movable mass. The length of the central plate (L_p) can be determined using Equation 3.4. The width of the electrodes, denoted as in equation, is a parameter that must be determined by the designer, considering the design rules associated with the manufacturing process. The variable (N_{te}) denotes the total number of testing fingers that are connected. It is necessary to provide a proposal about the spacing between the sensors and the test combs (Δs) [39].

$$L_p = 3\big((N_e + N_{te})/2\big)(w_e + d) - 2d + (\Delta s) \tag{2.8}$$

The designer is also responsible for proposing the width of the middle plate, which is denoted by W_p. This variable, on the other hand, has an effect on the ultimate springs magnitudes as well as the sensing element overall width. If the width of the center plate is increased, then the overall width of the sensing element will also be increased; however, the magnitude of the springs will be decreased.

The constant (k) of the spring system has to be estimated as in equation 2.9, in order for there to be a proportionate movement on the mass in response to a particular

acceleration (a), which will lead to make a capacitance difference. Then the acceleration to make these sensing elements are able to monitor is expressed in terms of G-force.

$$k = \frac{F}{x} = \frac{m \cdot a}{x} = \frac{\delta \cdot V_M \cdot a}{x} = \frac{\delta \cdot a \cdot \left(V_e + V_u + V_p\right)}{x} = \frac{\delta \cdot a \cdot \left(V_e + V_u + L_p \cdot W_p \cdot H_p\right)}{x} \tag{2.9}$$

The variable F represents the external force exerted on the moving mass (m) as a result of the acceleration applied (a). The symbol δ represents the density of the material. (2320[kg/m^3] for polysilicon), x is the maximum moveable mass displacement, V_M is the moveable mass volume composed from electrodes volume (V_e) and the junctions lies between the moveable mass and springs (V_u) in addition to the central plate volume (V_p). H_p, W_p and L_p are central plate dimensions (thickness, width, length). It is necessary to divide the spring constant by the two springs in order to obtain the model of the sensing element (equation 2.10) [39].

$$k_r = \frac{k}{2} = \frac{\delta \cdot a \cdot \left(V_e + V_u + L_p \cdot W_p \cdot H_p\right)}{2x} \tag{2.10}$$

The lengths of the spring's four components may be determined with the help of the following equation 2.11, provided that each of the spring's four sides were constructed in such a way that they had the same length [39].

$$L_r = \sqrt[3]{\left(\frac{\pi^4}{96}\right)\left(\frac{E H_r W_r^3}{k_r}\right)} \tag{2.11}$$

where E is the Young's Modulus, H_r and W_r are the spring height and width respectively.

To make linear, negative feedback, you have to add more than one feedback voltage (V_F) to a bias voltage (V_B) on both poles. This action creates a net electrostatic force on the mass, which may be expressed as the following equation [41]:

$$F = F_1 - F_2 = \frac{1}{2}\varepsilon A\left[\frac{(V_B + V_F)^2}{(d_0 - x)^2} - \frac{(V_B - V_F)^2}{(d_0 + x)^2}\right] \tag{2.12}$$

Where A is the electrode area, V_B and V_F are the electrode bias voltage and feedback voltage respectively, x and d_o are the distance between electrodes and displacement distance respectively.

Due to the fact that such proof mass deflection would be minimal while the control system is operating in closed loop mode, it is safe to infer that $d_o{}^2 << x^2$. With this assumption and some rearrangement, the following results may be obtained [42]:

$$F = F_1 - F_2 = 2\varepsilon A\left[\frac{d_0 x(V_B^2 + V_F^2) + V_B V_F d_0^2}{d_0^4}\right] \tag{2.13}$$

Using the limit at x is approach to zero, the solution to (2.13) is as follows [32]:

$$F = F_1 - F_{2,}\ , limx \longrightarrow 0,\ -2\varepsilon A\left[\frac{V_B}{d_0^2}V_F\right] \tag{2.14}$$

which is a connection characterized by a continuous cycle of destructive feedback. This scenario pertains to the assumption of employing a basic controller, specifically a pure proportional controller. The relationship that exists between the electrostatic feedback force and the degree of deflection of the seismic mass for various bias voltages is depicted in figure 2-2. The feedback force acts to restore the proof mass to its nominal position, provided that the displacement is small, which is typically the case when the machine is operated within its normal settings. However, when the seismic mass was displaced further from its equilibrium position, then the feedback

force will initially exhibit nonlinearity before ultimately undergoing a change in polarity. This would lead to something like a latch-up or electrostatic pull-in condition, which would ultimately result in the sensor becoming unstable. When a sensor is subjected to an acceleration that is more than the sensor's normal dynamic range, the result might be a sensor that experiences larger deflections. For instance, the scenario involves a motor vehicle encountering a road surface irregularity commonly referred to as a pothole. This sort of analog feedback has a number of drawbacks, the most significant of which is its propensity for instability. Including mechanical stoppers as a possible solution is one way to address the problem.

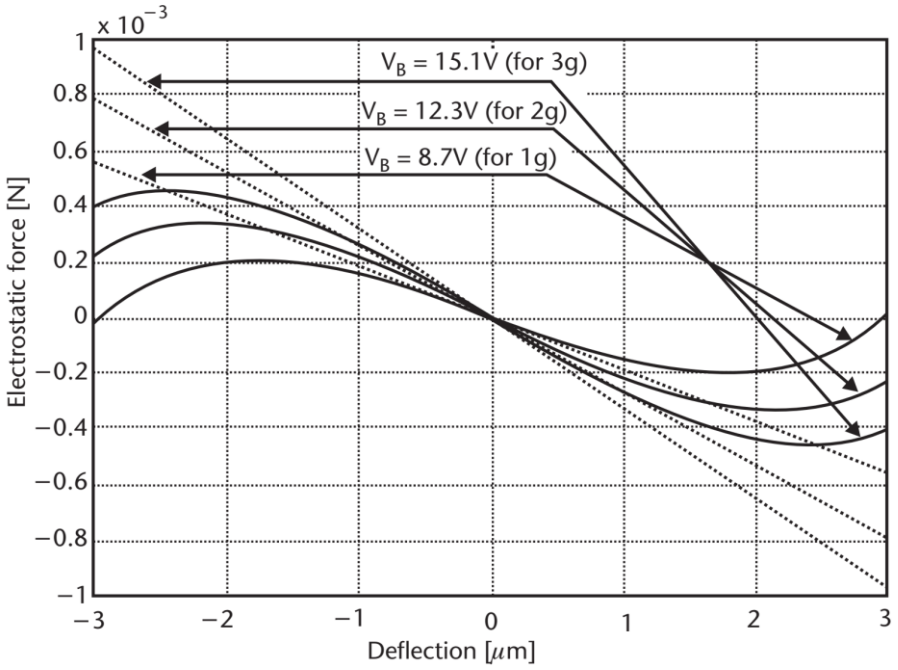

Figure 2-2 Analog Force Feedback Displaying The Net Electrostatic Force Applied to The Proof Mass [43]

The implementation of these stoppers would effectively prevent the proof mass from experiencing deflection in close proximity to the electrodes, thereby mitigating the occurrence of electrostatic pull-in. The sensing may also be included into an

electrostatic feedback system in the form of such a sigma-delta type control system, The schematic representation, as depicted in figure 2-3, can be observed.

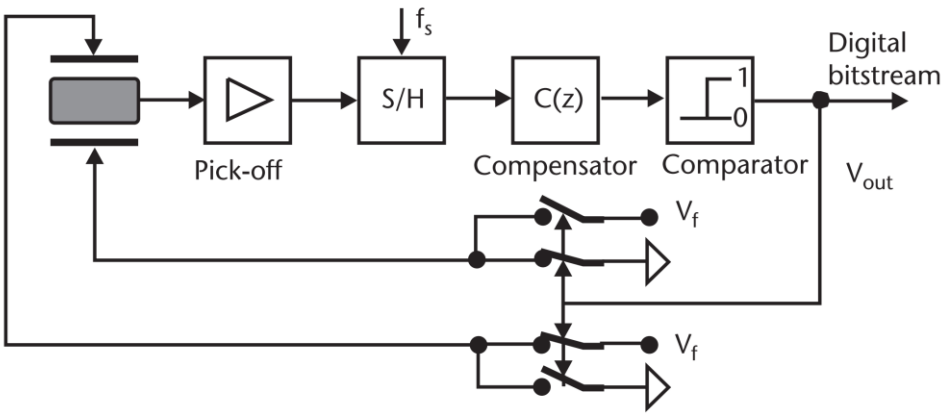

Figure 2-3 An Accelerometer With a Closed Loop and an Analog Force-Feedback [44]

A comparator is used in this method, and the information that it receives concerning the deflection of a proof mass gets supplied into it. It's possible that a compensator will be needed to keep the loop stable, but it will depend on how the proof mass behaves. The comparator is responsible for managing a variety of switches, which subsequently provides the feedback voltage to the electrode that is positioned further away from the proof mass at the same moment. Meanwhile, the other electrode is currently being grounded. The aforementioned process is executed for a pre-established duration, which is fixed in proportion to the sampling frequency of the comparator. The electromechanical sigma-delta modulator, similar to its electronic counterpart, operates as an oversampling device. Consequently, the clock frequency must exceed the sensor's bandwidth by a significant factor. In comparison to analog force-feedback, this method offers a variety of benefits, including the following [2]:

1. Given that the electrostatic feedback force is unidirectional, specifically exerting pressure on the proof mass to maintain its intended position, it is

not feasible for an electrostatic pull-in to occur as a result of electrostatic forces.

2. The comparator produces a digital signal in the form of pulse-density modulation, which serves as the output. This signal is subsequently captured and presented, with the count of high-bits within a specific interval serving as an indicator of the input acceleration. The resulting signal has the potential to directly connect with a digital signal processor, which has the capability to perform the necessary lowpass filtering and any additional signal processing that may be required.

   Despite the absence of applied acceleration to the sensor's input, it will still generate a self-sustained oscillation at the output, similar to other sigma-delta modulators.

3. This may be used as a straightforward method of testing the operation of the sensor, since the presence of a steady signal just at output would indicate that the sensor is defective.

2.4. Capacitive Accelerometers

The capacitive method of measuring the movement of the proof mass has a few intrinsic benefits over the piezoresistive method of picking up the signal. A big output signal, a strong steady-state response, and improved sensitivity as a result of low noise performance are provided by it. The most significant disadvantage of capacitive sensors is their susceptibility to the electromagnetic fields that are present in their environments. As a result, these sensors need to be protected in a thorough manner. The existence of parasitic capacitances in the input of the interface amplifiers will inevitably result in a degradation of the signal quality. This is something that cannot be prevented. In most cases, the variation in capacitance differential is what is noticed. The capacitance decreases as the proof mass moves

further away from an electrode, whereas it increases when it approaches the electrodes. By excluding the influence of peripheral fields, one can derive equations for capacitance change by solving the following equation [45]:

$$\Delta C = \varepsilon A \left(\frac{1}{d_0 - x} - \frac{1}{d_0 + x} \right) \overset{x^2 << d_0^2}{\longrightarrow} 2\varepsilon A \frac{x}{d_0^2} \tag{2.15}$$

Where A is the finger area, x is the distance between the fingers and d_o is the finger displacement. This is proportionate to the deflection induced first by input acceleration if and only if the assumption of tiny deflections is made. This assumption may not be valid for precision accelerometers, and as a result, closed-loop control could be the best option for ensuring that the proof mass deflections are kept to a minimum.

The first varieties of capacitive sensors have been generally manufactured using bulk micromachining as well as the assembly of many wafers through bonding processes. In most instances, the sensitivity axis was found to be aligned perpendicularly to the wafer's plane, with the cap wafers situated at the upper and lower ends of the device. Furthermore, apart from serving as a means of damping, and these cap wafers also functioned as the electrodes utilized for capacitive detection. Over-range stoppers serve the purpose of restricting the motion of the proof mass, thereby preventing any potential contact with the electrodes. Such contact would result in an undesirable electrostatic latch-up. Whether the sensor is run either open loop or closed loop operation determines how well it performs in either configuration [46].

Open loop operation has demonstrated effective adaptation to a wide range of industries, including the general-purpose and automobile sectors. However, it has been previously mentioned that the device is well-suited for inertial navigation and

guidance purposes within closed loop operation, primarily due to its exceptional sub-g resolution. Whenever sensors using capacitive are utilized in an open loop configuration, a notable issue arises when attempting to compare them to piezoresistive devices. This discrepancy arises from the requirement for the proof mass to exhibit parallel movement with the electrodes, resembling a piston-like motion, as opposed to a rotational motion around an axis, as observed in a cantilever-type suspension system. The latter may introduce nonlinearity concerns, particularly for larger deflections. The issue at hand arises due to the fact that the proof mass ought to undergo linear motion along the electrodes, similar to a piston, as opposed to rotational motion around an axis [47]. Despite the presentation of several additional prototypes of cantilever capacitive accelerometers, the construction of more intricate suspension systems became necessary. These systems required the proof mass to be attached to the substrate by a number of fingers and/or folding beams. To mitigate its cross-axis sensitivities of the design, it is imperative to ensure a high degree of symmetry in the design, to the extent that is practically achievable by humans. This implies that any acceleration experienced in a direction other than the axis of interest should not lead to a modification in the capacitance value. Figure 2-4 depicts a conventional layout for a sensing element that has been surface-micromachined [48].

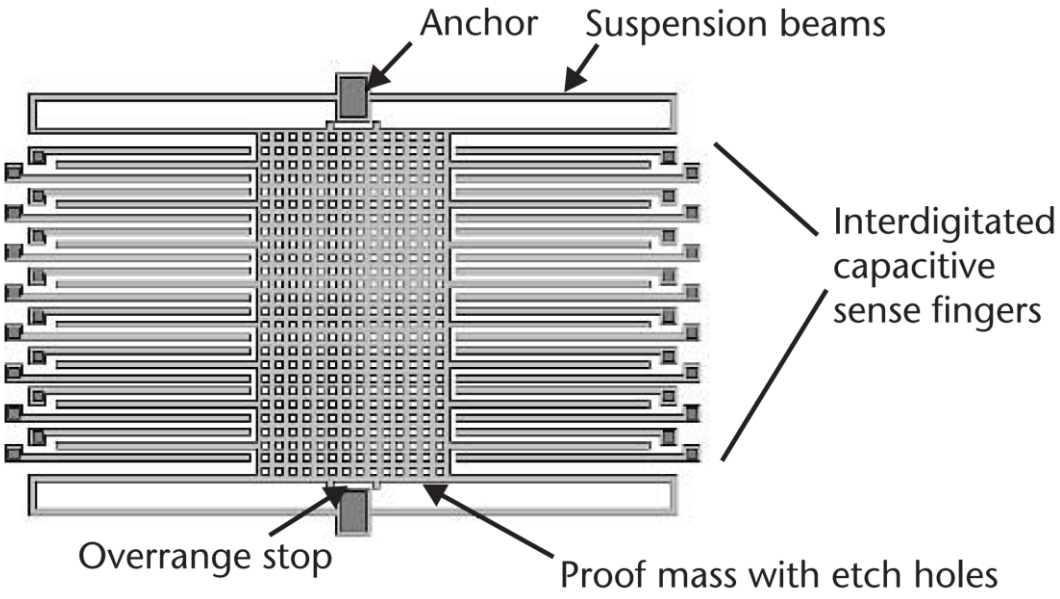

Figure 2-4 The Typical Architecture of a Capacitive Surface-Micromachined Accelerometer That Operates in-Plane [39]

The proof mass is connected to multiple fingers, each of which establishes a capacitor when connected to the anchored electrodes on both sides. In order to achieve an overall capacitance of approximately 100 femtofarad, it is necessary to connect a significant quantity of capacitors in parallel, given that the individual capacitance of this particular capacitor is only a few femtofarads [49].

If it is assumed that a sensor of this type has typical values for the mass of the sensing element with value $m = 0.1 \times 10^{-9}$ kg, a resonance frequency of $f_R = 10$ kHz, and a marginal capacitance value of 100 femtofarad, then the probably results static displacement for 1 mG is only 0.025Å, and the observed differential capacitance has been estimated to be approximately 10 attofarads. Accurate measurement of minute deflecting as well as capacitances necessitates the utilization of on-chip electronics, owing to their exceptional performance capabilities [33].

The efficacy of bulk-micromachined devices is considerably constrained by the presence of Brownian noise originating from the seismic mass, which tends to be approximately ten times greater than the noise exhibited by said devices. The reduction of the Brownian noise floor can be achieved to a significant extent by decreasing the pressure at which the sensor component is packed; however, this comes at the price of more complicated manufacturing and packing methods. Open-loop or closed-loop operation with force feedback are the two control system options, just as they are for bulk-micromachined sensors [50].

Micromachined accelerometers have seen a number of advancements in recent years, one of which is the development of sensors that are able to measure acceleration along up to three axes simultaneously. This is of relevance for a wide variety of applications, including medical applications, virtual reality applications, and inertial sensing applications. While it is possible to arrange the three single-axis equipment in a vertical manner, an integrated version offers advantages in terms of cost, dimensions, and alignment with the sensing axes. The reason for this is that the sensing components are fabricated using highly precise photolithographic techniques. There are two conceivable approaches that can be employed: the utilization of a single proof mass with sufficient flexibility to enable movement through either two or three axes, or the integration of multiple proof masses within a single chip to accommodate the different sense axes. When it comes to multi-axis accelerometers, one of the most significant challenges is cross-axis sensitivity [51].

2.5. Self-test and calibration methods

This section primarily focuses on the self-test with calibration procedures associated with a micro-electro-mechanical inertial measuring unit (MIMU), which

are extensively discussed. The aforementioned procedures are depicted in figure 2-5.

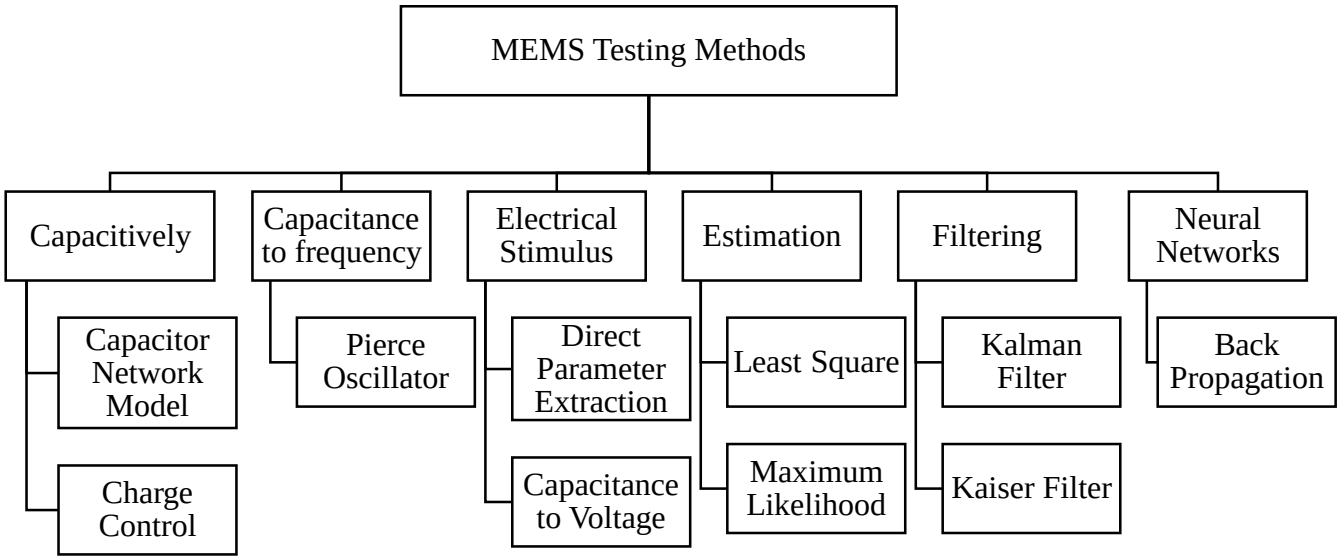

Figure 2-5 The Categories of The Many Different MEMS Testing Techniques [52]

2.6. Capacitive test

The concept behind this test originates from the concept of detecting a change in the capacitance. As a part of this testing out procedure, during the time that an electrostatic force is in effect, a capacitive accelerometer will have its electrostatic power activated by the force. The mechanism achieves this by employing the electrostatic force to ensure a safe separation from the proof mass [4].

2.6.1. Capacitor Network Model

A combdrive can be conceptualized as an electrical mechanism consisting of a series of interconnected capacitors arranged in a linear configuration. Figure 2-6(a)

depicts the magnitude of strain exerted on the accelerometer sensor. The employment of the fully differential spotting technique, in which the experience signal from the combdrive capacitor serves as the origin of the experience signal, is an essential component in the operation of the experience procedure. This approach taps into the experience. The sensor incorporates four unclear experience combdrives that are symmetrically decided. Figure 2-6 presents a schematic diagram that depicts the circuit configuration resulting from the inclusion of capacitors within the four combdrives employed in the experiment. Figure 2-6(a) depicts the unique attributes of the letters *l*, r, b, and t, symbolizing the concepts of cleaned away right, foot, as well as best (b), correspondingly. Figure 2-6(b) illustrates characters 1 and 2 demonstrating the two capacitors of a differential integrator contained within a combdrive [53]. In order to attain an elevation in delivery along the positive Y-axis, it is necessary to decrease the magnitude of capacitors denoted with a subscript 1, while concurrently augmenting the magnitude of capacitors denoted by the subscript 2.

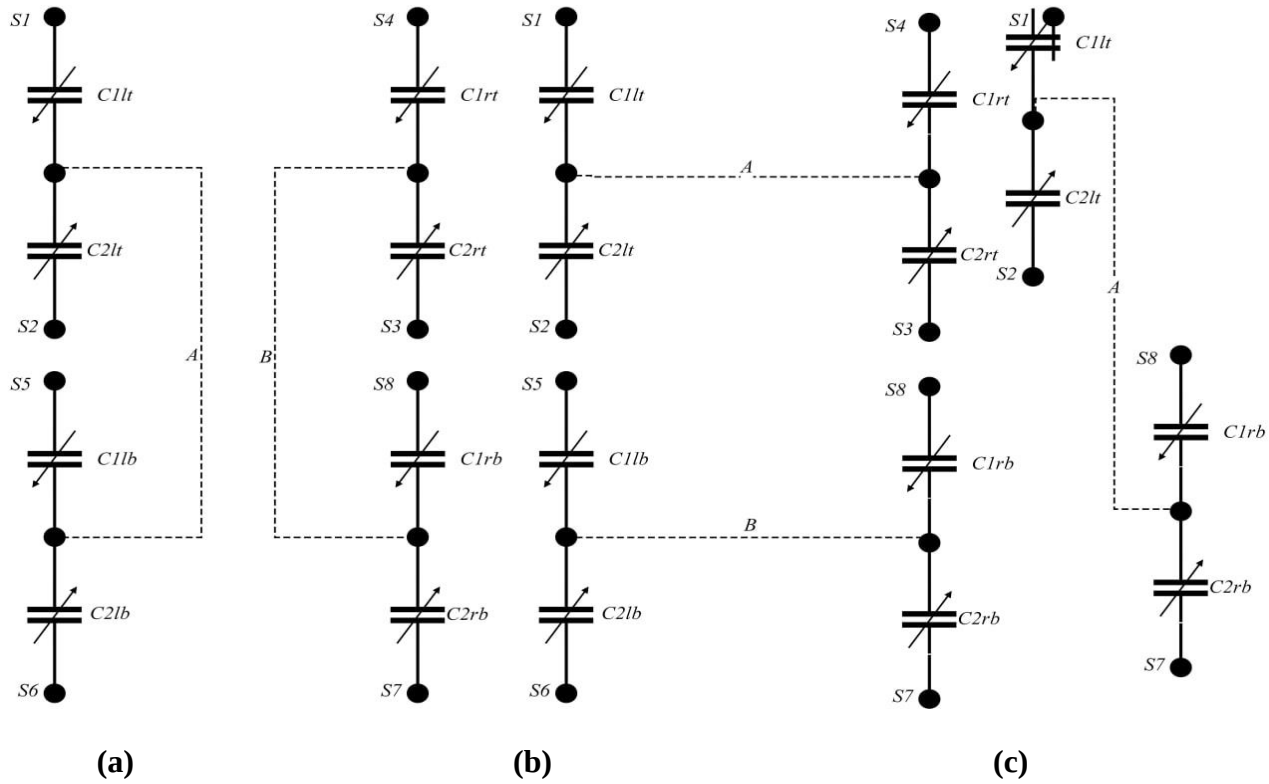

Figure 2-6 Topology of The Accelerometers Sensor for: (a) Differential Figuring out Approach With Vertical Set of Experience Combdrive Capacitors; (b) Set of Experience Combdrive Capacitors Diagonal; and (c) In The Modulation Node Group, S_1 and S_8 Have Sensing and Modulatory Functions, Respectively [52]

2.6.2. Charge Control

The technique that was given for examining a capacitive MEMS device may now be finished off with a contemporary DC evaluation. To ascertain the response of the MEMS shape to an elevated voltage, the rigidity of the MEMS shape is enhanced across its entire operational sensitivity spectrum. Figure 2-7 illustrates a duplicated rendition of the unravelling rectangular chart of the BIST setup [54]. For the purpose of making an evaluation of the response, an analogy with a Time-To-Digital Converter (TDC) are utilized.

Capacitive MEMS devices are able to have their fee management checked by using the fee pump. The estimate circuitry is subjected to checks on a tier-by-tier basis in order to cover nonlinearity issues.

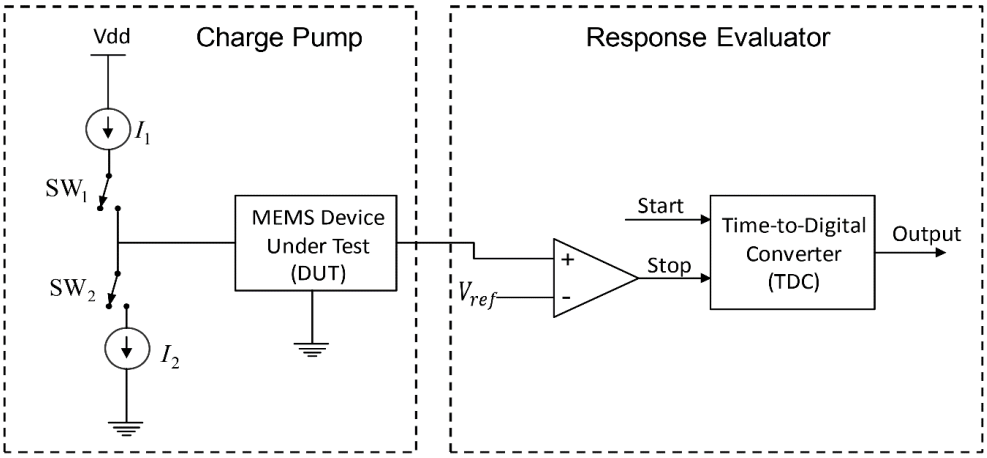

Figure 2-7 A Condensed Version of The Block Diagram That Represents The BIST Architecture [52]

The response evaluator is comprised of many components, including the comparator and the time-to-digital converter. Charge-control capacitive MEMS may be tested by the system thanks to the charge pump. In order to address the non-linear nature of the measurement circuitry, two distinct iterations of the test are conducted. The initial step involves the charging of the Device Under Test (DUT) capacitor through the utilization of a current source I_1 up to a point when it ceases producing signal, when its voltage reaches to a reference value. After this point, the current source I_2 stops charging the capacitor. When working using a Time-to-Digital Converter (TDC), it is necessary to monitor the amount of time that elapses between the initiation signal and the termination signal in order to calculate the value of the capacitor [53]. Only during the second phase does I_2 begin to discharge the capacitor, and the TDC similarly keeps track of the required amount of time. This method is

analogous to the dual-slope measuring strategy, which is often used in the production of items that are in compliance with industry standards.

In a perfect world, the time periods for charge and discharge for $I_1 = I_2$ would be the same; nevertheless, in practice, there is a disparity between them owing both noise and nonlinearities in the system. It is impossible to achieve this degree of precision using a measuring method that only involves one step. Because of the use of the dual-slope measuring approach, any and all impacts of nonlinearities are, to some extent, nullified, which results in an increase in the accuracy of the measurements. As will be shown in the next section, it is also possible to reduce the negative effects such noise and nonlinearities to a greater extent by including a reference capacitor into the BIST circuitry that has been recommended. The inclusion of a reference capacitor in the design effectively mitigates the adverse effects caused by parasitic capacitance [52].

Figure 2-8 depicts the block diagram of the Built-In Self-Test BIST electronics. The circuit incorporates a reference capacitor that possesses an equivalence to the MEMS capacitor in its free-standing condition. This capacitor is a part of the circuit. The following will explain how the BIST system works. To begin, the parasitic capacitance C_p has to be charged for time t_0, which may be determined by switching on SW_1 while leaving SW_3 and SW_4 in their original open positions. After that, the switch labeled SW_4 will become active, which will connect C_{ref} to the circuit. After that, the amount of time required for t_1 for charged $C_{ref} + C_p$ will be determined. After that, the $C_{MEMS} + C_p$ charge up time plus the C_P charge up time is computed. The use of this method allows accurate measurements to be taken on changes in MEMS capacitance.

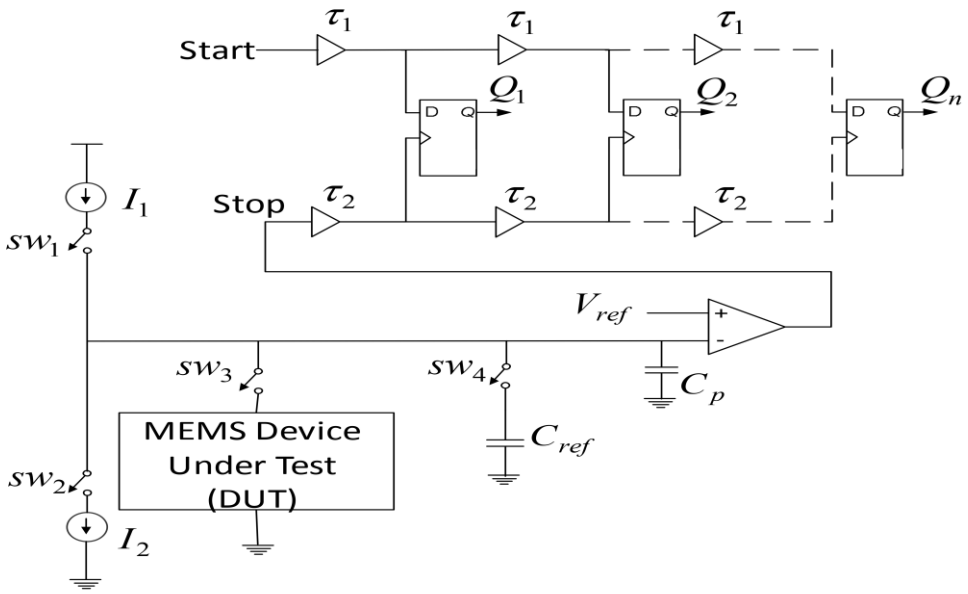

Figure 2-8 BIST Electronics for Charge Control [54]

A simple TDC may be manufactured by using a singular delay line that is comprised of identical delay cells. The time-based interval between the ascending edges of the initiation pulse and the termination pulse can be ascertained through the utilization of this measurement methodology. In order to provide the flip flops with a multi-phase clock, it is imperative to transmit the start pulse to the delay line [53]. The duration of this input period is determined by the quantity of flip-flops capable of transitioning from a low to high state. The resolution of measurement in this system is constrained to the temporal delay equivalent to the duration of one cell. In order to enhance the precision of measurements, a viable approach involves the utilization of a Vernier Delay Line (VDL) which integrates two distinct delay lines, as depicted in figure 2-9 [54].

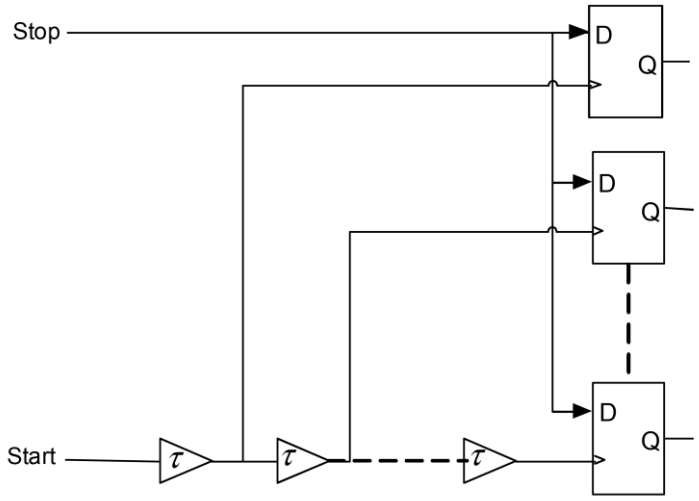

Figure 2-9 The Time-to-Digital Converter (TDC) That is Extremely Straightforward [52]

The inherent design of flip-flops enables them to function as arbitrators, facilitating the analysis of signal phases and the quantization of input time intervals. To facilitate the generation of multi-phase input signals, the delay components comprising the Vernier Delay Line (VDL) are organized into delay lines. The resolution of the VDL design is contingent upon the disparity in propagation delays exhibited by two distinct delay elements. When compared to the propagation delay for a single delayed element, the difference in propagation delays that occur between numerous delay elements may be a substantially smaller discrepancy.

The ideal TDC would have a characteristic curve that had the same quantization number of steps in the whole measurement range. This would provide for a perfect TDC. This curve is used to show an ideal TDC. This curve represents the perfect TDC for our purposes. In practice, the quantization step will shift across the input dynamic range owing to variables such as noise, mismatch, and random variations in the delay between the delay cells. This is because these factors all affect the delay between the delay cells. As a direct result of this, the characteristic curve that serves as a stand-in for a genuine TDC in reality possesses a non-uniform quantization step

in its progression. The values for this step change according on the quantization level that is being applied at this time. Quantization step variation in a TDC characteristic curve has an effect on all of these errors with Differential Nonlinearity (DNL) with Integral Nonlinearity (INL). The terms "DNL" and "INL" are used to refer to these types of mistakes, respectively. Both Differential Nonlinearity (DNL) as well as Integral Nonlinearity (INL) are acronyms for the same idea. Differential Nonlinearity (DNL) is the more common term [47]. The effects of these nonlinearities may be effectively mitigated with the use of an appropriate calibration.

Sensitivity on the sub-femtofarad scale is required for fault detection in capacitive MEMS. It is not feasible to acquire a measurement with this degree of high resolution without first considerably lowering the quantity for noise, nonlinear properties, and other causes of measurement error. Obtaining such a measurement would be impossible. With the use of self-calibration in the BIST system that has been developed, these unintended consequences have been mitigated to a significant degree. If switches SW_3, SW_4, and SW_1 are all open, the parasitic capacitor C_p begins to charge, and the equation describing this process may be stated as follows [53]:

$$I_1 * t_0 = C_p * V_{ref} \tag{2.16}$$

Where V_{ref} is the voltage used as a reference, C_p is the parasitic capacitance and I_1 is the value used for the current source. The switch for SW_4 has been turned off, however the switch for SW3 is still in operation, and it will be [53]:

$$I_1 * t_1 = \left(C_{ref} + C_p\right) * V_{ref} \tag{2.17}$$

Where, C_{ref} is the reference capacitance. In addition to this, when SW_3 is locked and SW4 is turned off.

$$I_1 * t_2 = \left(C_{MEMS} + C_p\right) * V_{ref} \tag{2.18}$$

C_{MEMS} is the MEMS device capacitance. Using the correlations in items (2.16), (217), and (2.18), it may deduce the following correlations [53]:

$$\frac{t_1}{t_0} = K_1 = \frac{C_{ref}}{C_p} + 1 \tag{2.19}$$

$$\frac{t_2}{t_0} = K_2 = \frac{C_{MEMS}}{C_p} + 1 \tag{2.20}$$

The formula for parasitic capacitance can be obtained by solving these equations for C_P, then the following result is obtained [53]:

$$\frac{C_{MEMS}}{K_2 - 1} = \frac{C_{ref}}{K_1 - 1} \tag{2.21}$$

When triggered, capacitive MEMS devices revert to their previous behavior, which is to deviate more from the C_{ref} (reference value) in the situation of the free-standing.

The following results can be obtained from assuming that the change is C, or $C_{MEMS} = C_{ref} + \Delta C$ [53]:

$$\Delta C = \frac{K_2 - K_1}{K_1 - 1} C_{ref} \tag{2.22}$$

Since it is abundantly evident that ΔC is not a function of I_{ref}, V_{ref}, or C_p, the degree of measurement uncertainty that is brought on by changes in these three variables is considerably decreased.

As a consequence of this, there is less unfavorable effects that variations in temperature, supply voltage, and process have on the conclusions of the measurement. It is possible to use the data that were acquired via discharging

capacitors by the bottom current source I_2 in order to further limit the nonlinearity affects that the BIST technique has on the measurement findings. Utilizing the findings is one method for accomplishing this goal.

2.7. Capacitance to frequency

2.7.1. Pierce oscillator

This BIST method is used for capacitive MEMS, focuses on the frequency domain rather than the time domain while carrying out its calculations. It is believed that the auxiliary abandons that cause very small capacitance variations are much easier to find out within the recurrence region than within the time region, especially for thunderous structures that are tested near to their thundering frequency. RLC tanks, which stand for resistor inductor capacitor, are used to guarantee that operations are carried out at the preferred recurrence and to give an exceptional level of strength with the disturbances of the open air [55].

It can be seen from figure 2-10 that the capacitor by the name of C_1 is makes the connection between the MEMS device and the oscillator. This capacitor is used as a reference, and the amount of wear and tear it has sustained makes it almost indistinguishable from the apparent capacitance of the MEMS tool. It's possible that the diagram in figure 2-11 represents the shape of a certain kind of instrument [55].

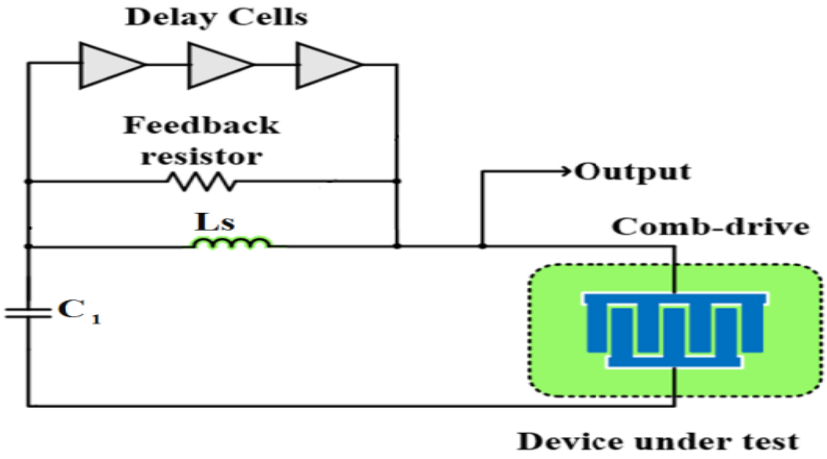

Figure 2-10 Check Setup Chart [52]

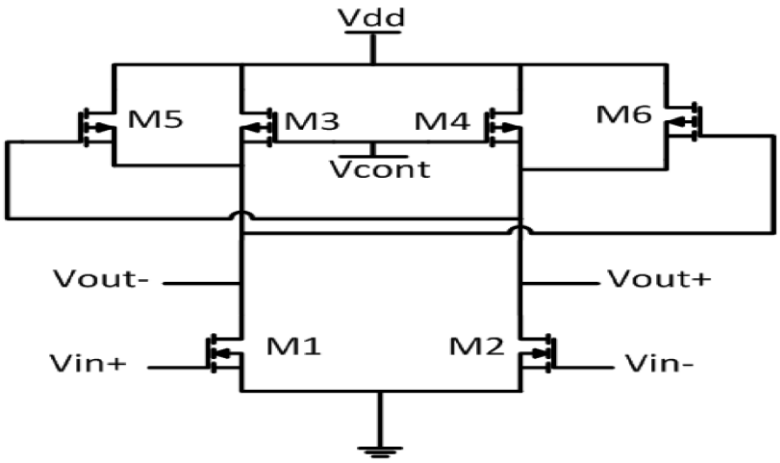

Figure 2-11 Delay Control Using PMOS Transistors M_3 and M_4 [55]

The greatest current that may flow inside a differential pair is limited by the current that flows in the tail. As a consequence of this, the parasitic capacitors are charged with a limited current during the process of changing from a low level to a high level, which extends the amount of time that is required to carry out the transformation. As a consequence of this, there is an increased possibility that such noise will have an effect on the switching level as well as contribute disruption to the oscillator. PMOS transistors M_3 and M_4 are shown functioning in figure 2-11 with variable resistor loads that are responsible for regulating the delay throughout a

certain range. The inclusion of M_5 and M_6 makes transitions from the low level to the high level even more briskly accomplished [55].

Even though it is impractical to produce a pure linear oscillator in reality, the feedback network helps to stabilize the frequency and keeps the oscillator in the linear zone of operation. This is accomplished despite the fact that creating a pure linear oscillator is not possible. A feedback resistor was also included so that the input impedance of the oscillator could be adjusted, and excellent matching could be ensured, so that the resonator would be able to regulate the delay cells. This circuit's resonance frequency may be calculated using equation 2.23, which can be found here f_{res} [52].

$$f_{res} = \frac{1}{2\pi\sqrt{L_S C}} \; where \; C = (C_1 C_{MEMS})/(C_1 + C_{MEMS}) \tag{2.23}$$

where, C_1 and C_{MEMS} are the oscillator and MEMS device capacitors respectively. The following is an expression that may be used to describe the variations in the resonance frequency of the test circuit that are produced with changes in MEMS capacitance [53]:

$$\frac{\partial f_{res}}{\partial C} = \frac{-1}{4\pi C\sqrt{L_S C}} = \frac{-f_{res}}{2C} \tag{2.24}$$

The very little fluctuation in capacitance may be stated as follows [53]:

$$\Delta f_{res} \approx \frac{-1}{4\pi C\sqrt{L_s C}}\Delta C \approx \frac{-f_{res}}{2C}\Delta C \tag{2.25}$$

As can be seen, the capacitance variation, denoted by ΔC, is multiplied by $-f_{res}/2C$, which results in a sizeable amount. According to the research that was shown

earlier [55], locating defects in MEMS devices in the frequency domain seems to be a lot less difficult than doing so in the time domain.

2.8. Electrical Stimulus

The employed testing methodology utilizes an electrical signal to generate a physical signal within the microelectromechanical system (MEMS), alongside the application of an electrostatic force. The aforementioned process is executed by subjecting the microelectromechanical systems (MEMS) to a specific input signal. The aforementioned physiological indication is employed to activate stimuli on the MEMS critical practical substructures in order to elicit a response. If the reaction can be converted back into an electrical signal, an effective Built-In Self-Test (BIST) technique could utilize this physical signal to replicate the physical forces experienced by the Device Under Test (DUT) during normal operation, or to gather information regarding the condition of the DUT. If the reaction can be converted back into an electrical signal, a Built-In Self-Test (BIST) method could utilize this physical signal [56].

2.8.1. Direct parameter extraction

The electrical parameters obtained from the analysis of MEMS yield response are utilized for the computation of mechanical properties, damping coefficients, including mass along with spring constants. The mechanical parameters exhibit a strong correlation with the electrical parameters. An extremely high-frequency pulse was used in order to bring up an oscillating motion at the capacitor plates. In order to assess the capacitance, the researchers employed an oscillating motion, altered the frequency signal, and utilized a capacitance detection circuit that relied exclusively on operational amplifiers. This facilitated the computation of the variation in capacitance. Figure 2-12 illustrates multivariate adaptive regression splines, that are

employed to predict the mechanical characteristics of a hobby with an error of much less than 5% based on the capacitance data. This prediction may be viewed here [56].

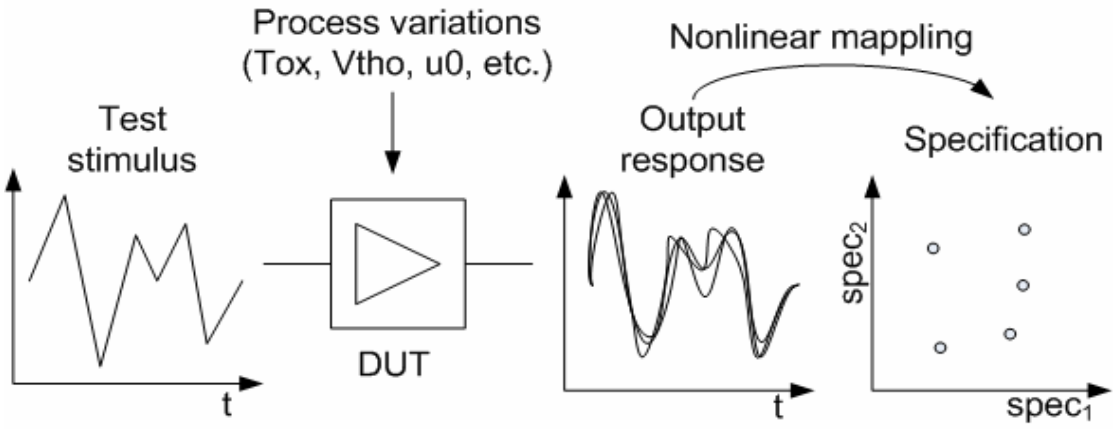

Figure 2-12 Mapping Response Using Translated Lower Back to an Electrical Sign [52]

Conventional testing techniques for RF, analogue, and mixed-signal circuits depend on testing procedures that are driven by the specifications of the circuits. During these kinds of tests, the specifications of the DUT are measured and compared to the specification boundaries that were established in the past in order to determine whether or not the DUT passes or fails each specification. This needs a distinct test setup for each standard, which increases the amount of time required for testing as well as the associated expense. Figure 2-14 illustrates how a single test setup may be used to predict all of the important features by using a single input stimulus. This helps to reduce the amount of time and money spent on testing.

The choice of a test input stimulus is ultimately what will determine the lack of successful coverage of the alternative testing technique. The training and testing stimulus has been meticulously adjusted in order to get an output response which is closely associated with the values that are declared to be of interest. This procedure is conducted with the purpose of achieving the intended outcome. The optimization of the test stimulus may exhibit substantial variation depending on the specific

Device Under Test (DUT) being evaluated and the effectiveness metrics being analyzed. Various test creation methods can be employed to optimize the input test stimuli for the Device Under Test (DUT).

The primary aim of the stimuli generating the module was to produce the input stimulus capable of adequately activate the Device Under Test (DUT) in such a manner that the resulting test response demonstrates a statistically significant association with the mechanical parameters that are pertinent to the test. The test-generating algorithm utilized in this context is built upon the optimization technique called gradient search. The optimization of input stimuli in this study involves the utilization of the error in prediction of the developed model as the cost function. The computation of this error entails ascertaining the disparity between the observed value and the estimated value of a parameter. The optimization process is performed on two different categories of inputs: (a) the single-tone input and (b) the three-tone input, where each tone is optimized for a specific parameter within the system.

It is postulated that the input is represented by the expression ($V_{dc} + V_{ac} \sin(wt)$) in the case of a single tone. Upon initial investigation of the system, it was determined that the frequency range of 15 to 50 Hz exhibited the highest level of effectiveness. The phenomenon of the beginning overshoot for the beam surpassing two-thirds of the original separation between the two plates has been noted at frequencies below 15 Hz [56]. This was discovered by measurements.

In this particular instance, the input waveforms that are being considered are multi-sine waveforms, and the formula that is being applied to them is $V_{dc} + V_{ac}$ (sinw1t + sinw2t + sinw3t). During the process of optimization, each tone is modified for a specific value of a particular parameter. The search method uses the relative inaccuracy of the particular parameter that is being optimized to serve as the cost

function. The overall performance of the tone is being enhanced as a consequence. The circuit illustrated in Figure 2-13 represents a fundamental operational amplifier (op-amp) capacitance sensing configuration employed to detect the actual capacitance within a microelectromechanical systems (MEMS) acceleration sensor beam. The present circuit is employed for the purpose of capacitance detection in the MEMS accelerometer beam [56].

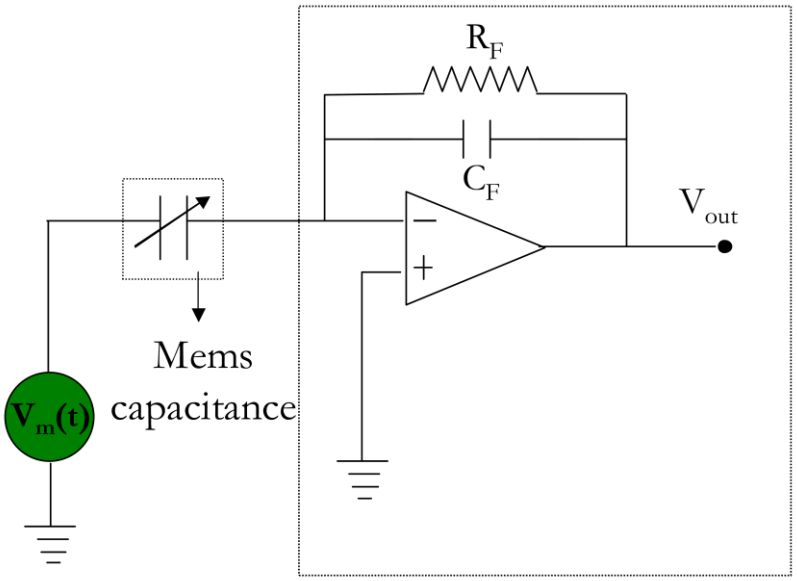

Figure 2-13 Circuit for Measuring Capacitance [52]

The frequency of the measured input signal, characterized by a sinusoidal waveform, is notably greater than the frequency of the input signal associated with the employed MEMS capacitor. In the simulation setup, the measurement frequency is specified as one megahertz (MHz), with an amplitude of one volt (V). By employing the gain measurements acquired through the capacitance detecting circuit, it becomes possible to make predictions concerning the attributes within the system.

The utilization of data for measurements is restricted to situations wherein the system has attained a state of equilibrium. The essential parameters that must be accurately determined based on the test results are the mass of the accelerometer, its damping coefficient, and its spring constant. The model is constructed using seventy instances, while the remaining thirty instances are reserved for evaluation purposes. The RMS error, comprised of both the absolute errors and the root mean square error, serves as the principal evaluation metric for the model that has been developed.

The commencement of the system activation is initiated through the utilization of a singular mood input in the optimal frequency about 45 Hz. Afterwards, the parameter values are reused for the gain evaluations obtained from the assessment set consisting of 30 instances of devices. The error levels obtained are presented in table 2-2, which is displayed below, and it compares the projected values with the actual values [1].

Table 2-2 Discussion Pertains of The Optimization Error with Inputting a Single Tone [1]

Parameters	Nominal value	% Variation	ε_{rms}	ε_{rel}
Mass	10 mg	5 %	5.5390e-5	2.75%
Damping	0.1	10 %	0.0013	2.62%
Spring Constant	50	10 %	1.3747	6.72%

It is clear that there was an increase in the amount of inaccuracy associated with the prediction of the spring constant when contrasted with the case in which

optimization was not performed. The frequencies that were closer to the upper limit were given more weight in the calculation than the frequencies that were closer to the lower bound. This was carried out to guarantee that the device vibrates as little as possible while still maintaining an acceptable level of accuracy. It is possible to demonstrate that the overall mean accuracy of the parameters remains lower than 5%.

Once again, a three-tone frequency is used in order to mimic the system, for each frequency being customized in order to minimize the inaccuracy of a particular parameter. The findings of the errors are shown in table 2-3.

Table 2-3 Discussion Pertains of The Optimization Error with Inputting a Three Tone [1]

Parameters	Nominal value	% Variation	ε_{rms}	ε_{rel}
Mass	10 mg	5 %	3.374e-5	1.72%
Damping	0.1	10 %	0.0012	4.19%
Spring Constant	50	10 %	0.2079	1.119%

As compared to the scenario with the three-tone input, it is clear that there is a significant increase in the amount of error that exists in estimating the damping coefficient. This may be explained in part by the fact that the tones are separately adjusted to correspond to each feature. The effects of the damping coefficient tone were obscured since they were blended with the effects of the other two tones [57].

2.9. Capacitance to voltage

This approach involves the utilization of an electric stimulus to initiate the activation of microelectromechanical systems (MEMS), subsequently leading to the acquisition of the analogue output voltage of the device. The mechanical testing parameter has the capability to be transmitted to the output voltage of the device. The proposed solution incorporates existing readout circuitry while simultaneously reducing overall complexity to a significant extent. Figure 2-14 shows a circuit consisting of a Digital to Analogue Converter (DAC) used to amplify the electrical signal of a MEMS device, the Capacitive to Voltage (C2V) converting device, as well as the sigma-delta Analogue to Digital Converter (ADC) used for converting the output signal into a digital representation [42].

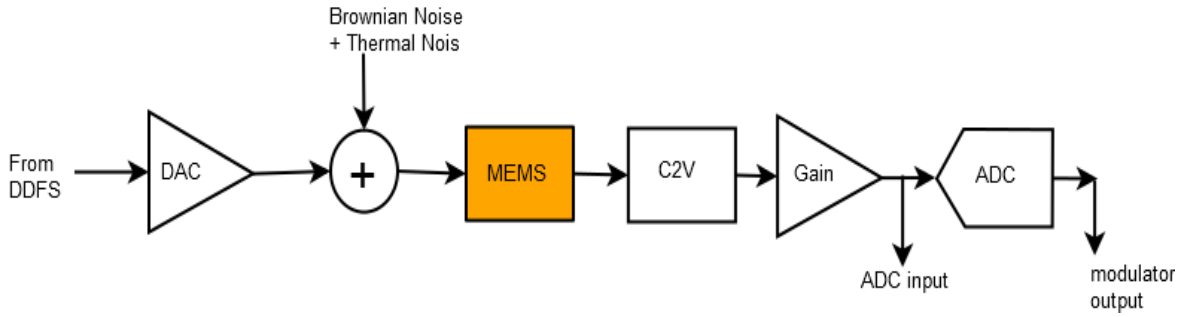

Figure 2-14 The Proposed DAC Method Utilized for Excitation Production Signal [42]

This digital-to-analog converter (DAC) is employed to generate a stimulus for the microelectromechanical systems (MEMS) tool, outcome is a signal that exhibits distinct, step-like levels. The microelectromechanical systems (MEMS) plates are linked to the C2V convention device, and the resulting signal is encoded using an analog-to-digital (A/D) converter before being stored in a field programmable gate array (FPGA). The excitation frequency of the MEMS tool is systematically varied from one to six thousand hertz, with each step incrementing by five hundred hertz.

The outcome of each frequency step is recorded and stored in the field-programmable gate array (FPGA) [42].

This data employed in obtaining the electrical characteristics, which are then utilized in the calculation of the calibration coefficient for the MEMS device. This program takes use of an accelerometer in the form of a comb, which has three axes. The accelerometer will be used by a variety of different electrical devices. The same form of sensory excitation is used for acceleration in the physical world. A Sigma-Delta Converter, a Capacitance-to-Voltage converter, and a Signal Generator make up the built-in self-test architecture of the MEMS device. In order to trigger the MEMS accelerometer, electrical stimuli are applied, and these electrical stimuli should be of a sort that is either identical to or analogous to that of a sine wave. An architecture is needed in order to fully characterize the phase and magnitude response of the MEMS device that is being energized by such a signal generator whose signal frequency gets swept across a range. This is necessary in order to fully characterize the phase and magnitude response of the MEMS device. A DUT is given electrical stimulation, and then the resulting output is characterized and digitalized with the assistance of a Sigma-Delta A/D converter.

2.10. Estimation

The calibration parameters are selected using the new release approach, which guarantees their accuracy and environmental friendliness. Due to this circumstance, a substantial amount of research was dedicated to the advancement of various estimation methods, such as the least squares, maximum likelihood, and minimum variance estimation techniques. Since the projected MEMS parameters have been calculated with varying levels of precision, there is a significant difference between

them. This is the root cause of the distinction. The subsections will serve to illustrate this point further [58].

2.10.1. Least squares

The calibration process comprises various components, encompassing a calibration system and the calibration range of standards. The misalignment of the package deal is one example of these errors. The calibration process for an inertial device involves establishing the coefficients for input and output that align with the reference data in a consistent manner [18]. The achievement of this objective is accomplished through the execution of a comparative analysis between the established input and the resulting output produced through the inertia device. The method of calibration encompasses various discrete elements, among which are the calibration algorithm and the calibration scheme. The present section commences with an exposition of the error model, encompassing various factors such as the scale factor, bias, sensor-to-sensor non-orthogonality error, and package misalignment error, which are duly accounted for. The utilization of a turntable is imperative for the calibration of error factors at various locations, as the rotational speed of the Earth is significantly slower compared to the bias output of low-precision Inertial Measurement Units (IMUs). Subsequently, a rudimentary calibration technique involving three locations that alternate between forward and backward was devised.

The accuracy of the least square method was assessed and adjusted to enable its application in calculating the least squares method, which is a widely employed approach for estimating error parameters. This method was used to calibrate the error system of the tri-axial microelectromechanical systems (MEMS) gyroscope, which includes the non-orthogonality error caused by the axes' misalignment. Additionally, it accounts for the misalignment error that occurs between the physical package

containing the sensing axes and the frame's axes. Furthermore, the error model also considers the bias, which represents any systematic deviation from the true value. Moreover, the model incorporates the consideration of bias. Furthermore, it is worth noting the presence of a phenomenon known as random error, which exhibits a correlation with temperature [59].

According to the principles of rigidity in rotation theory, it is feasible to interpret a coordinate system as a rigid body if the carrier and navigation coordinate systems maintain their rectangular shape and ensure that the axes remain consistently perpendicular to each other. In the given context, the coordinate system can be conceptualized as a rigid entity [59].

During the analysis of the angular positioning relationship between the two coordinate mechanisms, it is observed that the origin of one coordinate system aligns with the origin of another coordinate system through a translation procedure. The occurrence of coincidences can be observed in the context of any pair of coordinate systems. This spatially angular orientation relationship between each coordinate system can be comprehended by examining the fixed-point revolving of the rigid body, resulting in a straightforward consequence. The phenomenon known as package misalignment error refers to the occurrence of three rotation angles being successively rotated within the sequence Z → X → Y, with the intention of forming the rotation matrix as described in equations 2.26-2.28[18].

$$C_1 = \begin{bmatrix} cos\,\theta_z & -sin\,\theta_z & 0 \\ sin\,\theta_z & cos\,\theta_z & 0 \\ 0 & 0 & 1 \end{bmatrix} \tag{2.26}$$

$$C_2 = \begin{bmatrix} 1 & 0 & 0 \\ 0 & cos\,\theta_x & sin\,\theta_x \\ 0 & -sin\,\theta_x & cos\,\theta_x \end{bmatrix} \tag{2.27}$$

$$C_3 = \begin{bmatrix} cos\,\theta_y & 0 & -sin\,\theta_y \\ 0 & 1 & 0 \\ sin\,\theta_y & 0 & cos\,\theta_y \end{bmatrix} \quad (2.28)$$

where, θ_x, θ_y, and θ_z are the inertial device angles correspond to the x, y and z directions respectively.

When θ_x, θ_y, and θ_z are tiny angles, the following subsequent representation provides an estimation of the matrix for packaging misalignment errors. High-order values between small angles may be dismissed as being irrelevant since they occur between small angles [59].

$$C_b^n = C_3 C_2 C_1 \approx \begin{bmatrix} 1 & -\theta_z & \theta_y \\ \theta_z & 1 & -\theta_x \\ -\theta_y & \theta_x & 1 \end{bmatrix} \quad (2.29)$$

2.10.2. Maximum Likelihood

In order to determine the calibration parameters, the Newton iteration approach, which is both more time and labor efficient and precise, is used. The parameters that are calibrated using the maximum likelihood estimation method demonstrate superior accuracy and stability when compared to those calibrated using a least squares technique. The latter approach involves the estimation of parameters for a suboptimal estimation function, under the assumption that the random noise has a mean of zero. The parameters are estimated utilizing the least squares method [60].

The value represents the error that arises due to the non-zero sensor produced by the MEMS triaxial accelerometer, even though the expected yields are zero. This technique determines the values of the calibrating parameters according to a model that is constructed via the use of equation 2.30 [60].

$$y_k^m = C_S C_{Sn} C_n^b y_k^n + b_a + \varepsilon \quad (2.30)$$

Where y_k^n is a reflection of the gravity acceleration in the immediate region, C_n^b C_S is the scale-factor error, C_n is the upper triangular matrix, b_a is the zero-bias error, and talks to the Gaussian white uproar with a fluctuation of weight of zero. It is possible to determine the probability density function of y_k^n by using the of equation 2.31 [60].

$$f(y_k^m) = \frac{1}{\sigma\sqrt{2\pi}} exp\left[\frac{\left\|y_k^m - T_a y_k^b - b_a\right\|^2}{2\sigma^2}\right] \tag{2.31}$$

In line with the hypothesis of the maximum probability estimation technique, one can utilize the following formula to derive the likelihood function *L(θ)* of a randomly occurring variable of a general nature [60].

$$L(\theta) = \prod_{k=1}^{N} f(y_k^m) \tag{2.32}$$

The purpose of an ML evaluation is to determine which esteem is the best and which maximizes the possibility of success in the following areas [60]:

$$max\, L(\theta) = \prod_{k=1}^{N} f(y_k^m) = \frac{1}{\sigma\sqrt{2\pi}} exp\left[\frac{\left\|y_k^m - T_a y_k^b - b_a\right\|^2}{2\sigma^2}\right] \tag{2.33}$$

Where $T_a = C_S C_n$ and $y_k^b = C_n^b\, y_k^n$.

Determining the highest likelihood function value is synonymous with identifying the lowest value of $\sum_{k=1}^{N}\left(\left(\left\|\mathbf{y}_k^m - \mathbf{T}_a\mathbf{y}_k^b - \mathbf{b}_a\right\|^2\right)/2\sigma^2\right)$ to make the discussion more facilitating, the term ($2\sigma^2$) was disregarded, resulting in the expression of the Maximum Likelihood (ML) problem as in equation 2.35. The derivation of equation 2.30 involves the expansion of the constraint conditions stated in equation 2.35 utilizing the model described in equation 2.37 [18].

In order to achieve data normalization when using MEMS triaxial accelerometer adjusted data, it is necessary to ensure that the modular squared of the data equals one. The presence of noise has a direct impact on the magnitude of the adjusted MEMS triaxial accelerometer readings when squared.

$$\begin{aligned} &\min_{\theta} \sum_{k=1}^{N} \|e_k\|^2 = \min_{\theta} \sum_{k=1}^{N} \|y_k^m - T_a y_k^b - b_a\|^2, \\ &s.t.\ \|y_k^b\|^2 = 1, k = 1, \dots, \\ &1 = \|y_k^b\|^2 = \|R_a(y_k^m - b_a - \varepsilon)\|^2, \\ &= \|R_a(y_k^m - b_a)\|^2 - 2(y_k^m - b_a)^T R_a^T R_a \varepsilon + \varepsilon^T R_a^T R_a \varepsilon, \\ &\Delta \|R_a(y_k^m - b_a)\|^2 + \gamma, \end{aligned} \tag{2.34}$$

$$\begin{aligned} 1 = \|y_k^b\|^2 &= \|R_a(y_k^m - b_a - \varepsilon)\|^2, \\ &= \|R_a(y_k^m - b_a)\|^2 - 2(y_k^m - b_a)^T R_a^T R_a \varepsilon + \varepsilon^T R_a^T R_a \varepsilon, \\ &\triangleq \|R_a(y_k^m - b_a)\|^2 + \gamma, \end{aligned} \tag{2.35}$$

$$\begin{aligned} \mu_\gamma \triangleq E(\gamma) &= E[tr(R^T R \varepsilon \varepsilon^T)] = tr\{E[R^T R \varepsilon \varepsilon^T]\}, \\ &= tr\{E[R^T R] E[\varepsilon \varepsilon^T]\} = tr(R^T R)\sigma^2 > 0. \end{aligned} \tag{2.36}$$

Based on equation (2.37), it can be inferred that the value of μγ is not equivalent to zero, indicating that γ is a noise signal that exhibits bias. If the noise γ is considered to be unbiased, similar to the conventional Least Squares (LS) method, the estimated outcomes are suboptimal. To develop an all-encompassing error estimation model for achieving the most accurate estimate, it is necessary to incorporate a Lagrange constraint term to mitigate the impact of biased noises γ. The objective function for minimization is represented as equation 2.38, in which λ_k represents the Lagrange multiplier employed to enforce the constraints on the calibration value $\mathbf{y}_k^c$ for the two paradigms. The current estimated value is denoted as θ:

$$\theta = \left[vec^T(T_a)b_a^T y_1^{bT} \cdots y_N^{bT} \lambda_1 \cdots \lambda_N\right]^T \quad (2.37)$$

where the function vec(·) represents the process of transforming a matrix into a column vector by arranging its columns in order. It is important to note that the resulting column vector does not contain all three a smaller triangular elements of the original matrix [60].

$$f(\theta) = \sum_{k=1}^{N} \left\|\boldsymbol{y}_k^m - \boldsymbol{T}_a \boldsymbol{y}_k^b - \boldsymbol{b}_a\right\|^2 + \lambda_k \left(\left\|\boldsymbol{y}_k^b\right\|^2 - 1\right) \quad (2.38)$$

The mathematical expression representing the iteration formula used in the Newtonian iterating technique is as follows [60]:

$$\theta^{(i+1)} = \theta^{(i)} - \left[\nabla^2 f\left(\theta^{(i)}\right)\right]^{-1} \nabla f\left(\theta^{(i)}\right) \quad (2.39)$$

In the given context, $\theta^{(i+1)}$ denotes the parameter θ at the $(i + 1)$-th iteration, while $\theta^{(i)}$ represents the parameter θ at the i-th iteration. The symbols ∇f($\theta^{(i)}$) and ∇2f($\theta^{(i)}$) represent the Jacobian matrix and Hessian matrix, respectively, of the objective function at the i-th iteration.

2.11. Filtering

In contrast to the traditional method of calibration, this one does not require the assistance of an external high-precision equipment in order to be carried out. It is possible to accomplish this by relying on the rotation of the customer's hand. A one-of-a-kind clear out has been developed for the purpose of carrying out the calibrating procedure and estimating these unfairness mistakes, scale element blunders, and non-orthogonal blunders in this method.

2.11.1. Kalman filter

The covariance of the states communicated through implies of a mistake state ($\Delta\hat{x}_k$) is known as the value desire of the state as in 2.40 [16].

$$P_k = \varepsilon([\vec{x}_k - \hat{x}_k][\vec{x}_k - \hat{x}_k]^T) \quad (2.40)$$

Where: $\hat{x}_k$ is the state propagation, $\vec{x}_k$ is the system dynamics.

With the help of minimizing P_k, one is able to obtain the maximum quality comments advantage K_k, also known as the feedback gain. That is what is known as the Kalman filter, and it is used for linear structures. The remark advantage K_k will be computed, and the situation covariance will be changed (decreased) suitably when the measure is made accessible.

In this scenario, it was considered that the presence of a rigid framework defined by the physical object's coordinates (OX'YZ') and a comparative framework established by the Earth's coordinate system (OXYZ). The introduction illustrates the points along the directions of OY and OZ, as well as OX', OY', and OZ', individually. The initial position of the reference structure device is mapped to the initial position of the outline facilitation device, while the guidelines for the directions OY and OZ remain unaltered.

2.11.2. Kaiser filter

Based on the prescribed guideline, notable errors that can occur with the accelerometer with tri-axial system encompass static inclinations, errors in scale perspective, and misalignment errors. Equation 2.41 is commonly employed in a broad context to elucidate the flawed model of the tri-axial MEMS accelerometer [57].

$$\begin{bmatrix} A_x \\ A_y \\ A_z \end{bmatrix} = \begin{bmatrix} b_{xo} \\ b_{yo} \\ b_{zo} \end{bmatrix} + \begin{pmatrix} K_{xx} & S_{xy} & S_{xz} \\ S_{yx} & K_{yy} & S_{yz} \\ S_{zx} & S_{zy} & K_{zz} \end{pmatrix} \begin{bmatrix} a_x \\ a_y \\ a_z \end{bmatrix} + \begin{bmatrix} \varepsilon_x \\ \varepsilon_y \\ \varepsilon_z \end{bmatrix} \quad (2.41)$$

Where A_x, A_y and A_z constitute the unique outputs of tri-axial accelerometer. b_{xo} b_{yo} b_{zo} are the consistent biases of accelerometer. ax, ay, and az are the real accelerations that it is needed. K_{xx}, K_{yy}, K_{zz} are the size factors. S_{xy}, S_{xz}, S_{yx}, S_{yz}, S_{zx} and S_{zy} constitute the effect of misalignment mistakes coefficients. ε_x, ε_y and ε_z constitute the random noises which may be removed with the aid of using averaging.

The representation in numerical form of the Kaiser channel may be characterized by means of the implication of equation 2.42 [57]:

$$w(n) = \frac{I_o\left(\pi\alpha\sqrt{1-(\frac{2n}{N-1}-1)^2}\right)}{I_o\pi\alpha}, 0 \leq n \geq \tag{2.42}$$

Where *N* is the duration of the sequence, I_0 is the zero - order changed Bessel feature of the primary kind. The botches form condition of MEMS accelerometer in equation 2.43 may be communicated in another expression as takes after [57].

$$A^m = KA^e + A_o \tag{2.43}$$

Where A^m could be a 3×1 vector that speaks to the interesting yields of the accelerometer. *K* could be a 3×3 lattice which speaks to the size component and errors of misalignment. A^0 could be a 3×1 vector that speaks to inclination. A^e may be a 3×1 vector that speaks to the right increasing speed what it is required.

2.12. Neural networks

The purpose of this calibration technique method is to show the non-linear relationship between MEMS sensor's null-voltage and temperature using Back Propagation (BP) neural arrange. A given work f ranging between $[0, 1]^n$ and R_m, f belongs to L2 if each of f's organize capacities is square-integrable into the unit 3d form matrix [AA]. In a n-dimensional Euclidean space, [0, 1] n is the closed unit 3d

shape and R_m is the m-dimensional Euclidean space. The coming about arrangement BP neural arrange structure is appeared in figure 2-15, where Wi $(i = 1, 2, \dots, 9)$ are the weight values interfacing the input layer and the primary covered up layer, $W'ij$ $(i, j = 1, 2, \dots, 9)$ are the weight values interfacing the primary and the moment covered up layers, Vi $(i = 1, 2, \dots, 9)$ are the weight values interfacing the moment covered up layer and the yield layer, bi, j $(i = 1, 2;\ j = 1, 2, \dots, 9)$ is the limit esteem, ƒ is the transfer function tan-sigmoid and $\mathcal{F}$ is the exchange work direct sigmoid [61].

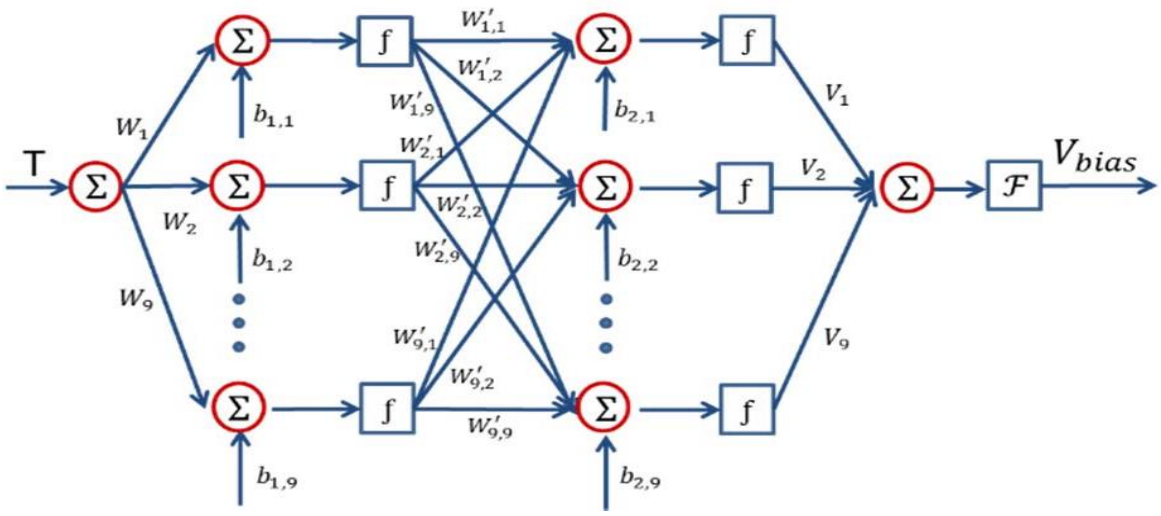

Figure 2-15 The Structure of The BP Neural Network [61]

CHAPTER THREE

The Proposed Self-Test and Calibration Algorithms

Chapter Three: The Proposed Self-Test and Calibration Algorithms

3.1. Introduction

This chapter presents the definition, mathematical design, simulation and implementation of proposed three self-test and calibration algorithms that can be used in MEMS. In addition, the Arduino board is presented for the purpose of reading the data from the MPU6050 three-axis sensor as which to be used as accelerometer. All the simulations and implementations have been carried out using a PC of Core i7 CPU with 2.4 GHz, and RAM 16 GB, with MATLAB 2020b and COMSOL 5.6. Table 3-1, summarizes these proposed test ways using Genetic Algorithm (GA), Akima interpolation and Transformed Unscented Kalman Filter (TUKF) with Delaunay Triangulation Algorithm.

Table 3-1 Proposed Calibration Algorithms

1st proposed algorithm	Genetic Algorithm-Based Self-Test and Calibration with Interpolation
2nd proposed algorithm	Self-Test and Calibration Built Into the Sigma-Delta Modulator
3rd proposed algorithm	Transformed Unscented Kalman Filter (TUKF)

The proposed system in which the Akima interpolation to be used is shown in figure 3-1. The output from the sensing element is treated as input to the lookup table, which the desired outputs in the cases of the fault are stored. These desired outputs are to be used as input points to the Akima algorithm to force the faulty sensing element output to be to the nearest correct output was calculated from the Genetic Algorithm.

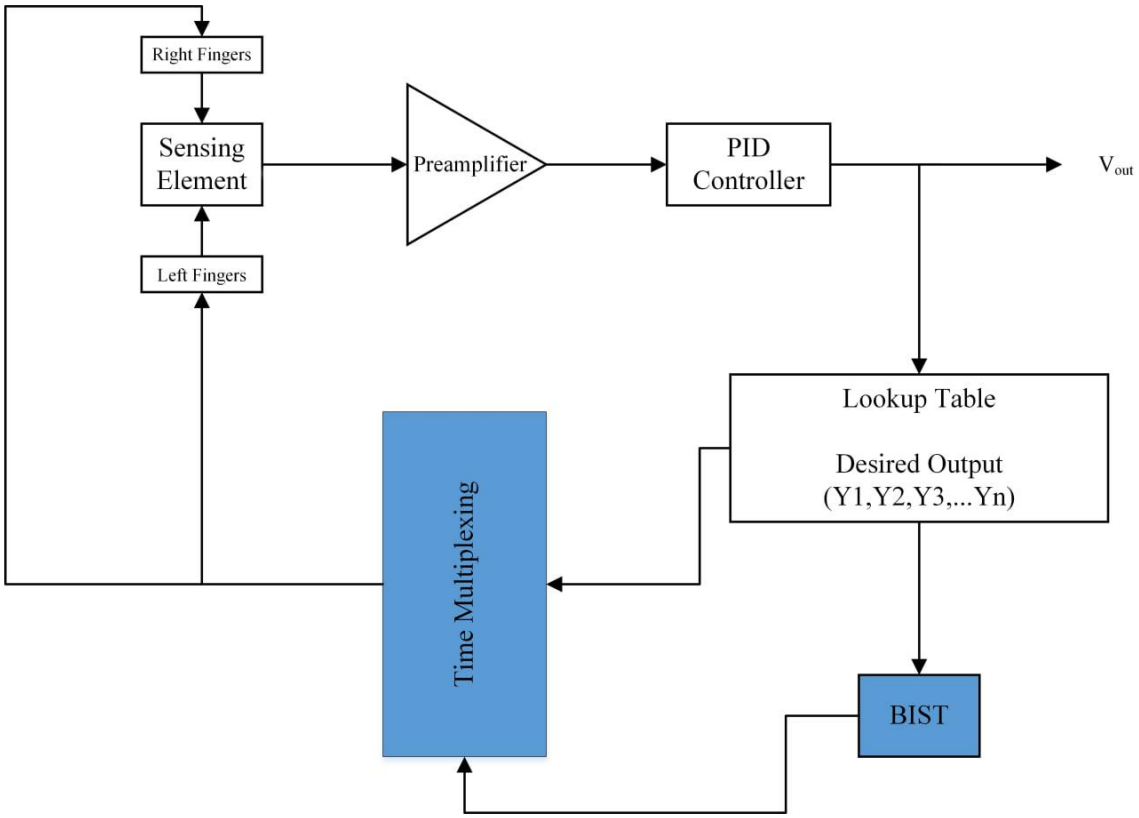

Figure 3-1 The Proposed Self-Test and Calibration System

Force feedback and capacitance sensing might both be accomplished using the time multiplexing technique while using the same sensing electrode.

The design of the sensing element will be made simpler by the collocated sensing mechanism, and higher-order resonance phenomenon will be diminished. Thus, the time-multiplexing technique used here to realize the separation of sensing and the feedback to prevent the interactions between sensing and force feedback mode which results to be more stability in the system. The implementation of the proposed technology for detecting is expected to mitigate higher-level resonance phenomena, thereby streamlining the design of sensing elements.

The sensing element is configured as a balanced capacitive bridge. In the feed-forward path, there is a charge preamplifier function to realize the capacitance

detection and reduce the low frequency noise. The PID controller is used to reduce the ripple of the sensing element because of the residue movement of the proof mass as a result of the spring movement.

The flow-process in figure 3-2 depicts the proposed methodology for the GA for the compensation calculation of the calibration. As an objective, the user must provide one or more objectives again for GA to optimize. The typical objective for the closed loop MEMS sensor is to maintain the proof mass in its initial position and to minimize the residual motion. The ratio of open loop to closed loop proof mass displacement is a measure of how well the electrical feedback force controls the sensing element and provides insight into the increase in dynamic range over the open loop situation. In addition, a GA requires a set of parameters that can be changed under user-defined limits.

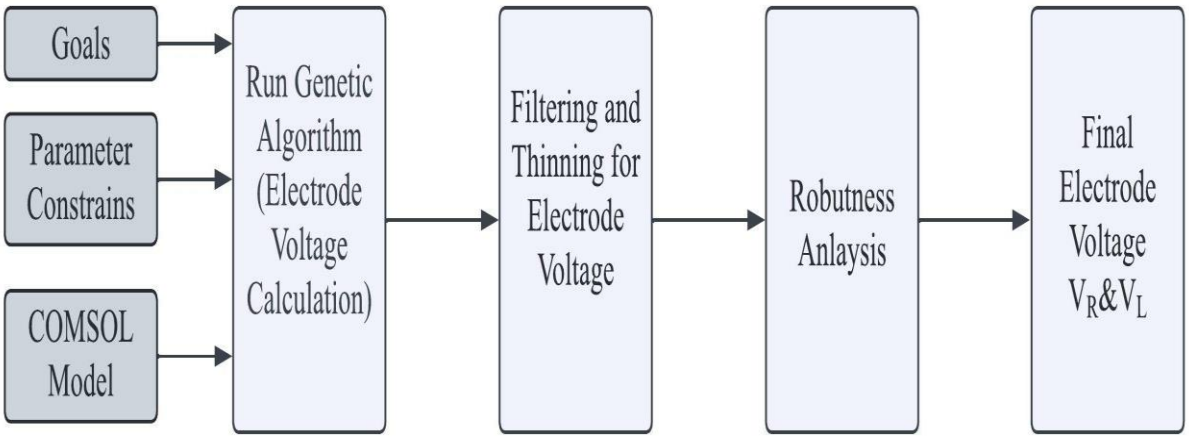

Figure 3-2 The Process Algorithm Design Steps for the GA-based Methodology

The GA is therefore initialized with a user-specified number of randomly picked parameter sets within the limits; this is referred to as a population. Each set of parameters is referred to as an individual. Generation 1 is represented by this

population. After first generation has indeed been simulated, the results are saved as a table, with each row including the parameter settings for one individual and their performance. This GA analyzes the results and then conducts a variety of tasks, including as choosing the best individuals, generating a specific amount of new random (mutation), and cross-fertilizing good individuals to generate new offspring. The final phase entails mixing various parameters from various good individuals to develop a new individual (child). Generation 2 is made up of these three phases.

3.2. Definition of the MEMS Sensor Model

The released seismic mass that supports the surface-micromachined accelerometer at either end is held up by connected springs. Additionally, the device's sides are lined with detecting and a self-test finger. As a result, when an acceleration is applied to the device, restoring force from the springs causes the proof mass to move in a direction that is proportionate to the acceleration.

The displacement that takes place between the fixed and movable fingers causes a change in capacitance. Several alternative circuits that are regarded as standard may be used to measure this change in capacitance. The capacitive interaction that exists between the moving sense electrodes and the stationary sense electrodes enables the displacement to be measured. During normal operation of the physical apparatus, the seismic mass, in conjunction with the attached moving fingers, is permitted to remain at a half of the supply voltage approximately. Simultaneously, the stationary sense fingers positioned adjacent to the mobile electrodes experience a high-frequency square waveform that alternates between zero and the complete power supply voltage, albeit with an inverted phase. Because of the capacitive connection between the stationary and moving electrodes, an alternating voltage is

created whenever the proof mass moves as a direct consequence of the acceleration. The magnitude of this voltage is directly proportional to the displacement.

This configuration cancels out the typical electrostatic force that exists between the moving sense electrodes and the stationary sense electrodes, making it possible for the associated electronics to process signals with greater ease. This is the same as adding a +/-2.5 millivolt difference between the left and right sides of the fixed sensing electrodes inside the model when the real device has a supply voltage of 5 volts. The graph in figure 3-3 illustrates the linear relation that exists between the sense voltage and the acceleration. This signal is then sent on to an amplifier, which, in the working version of the device, was constructed on the same substrate as the mechanical construction.

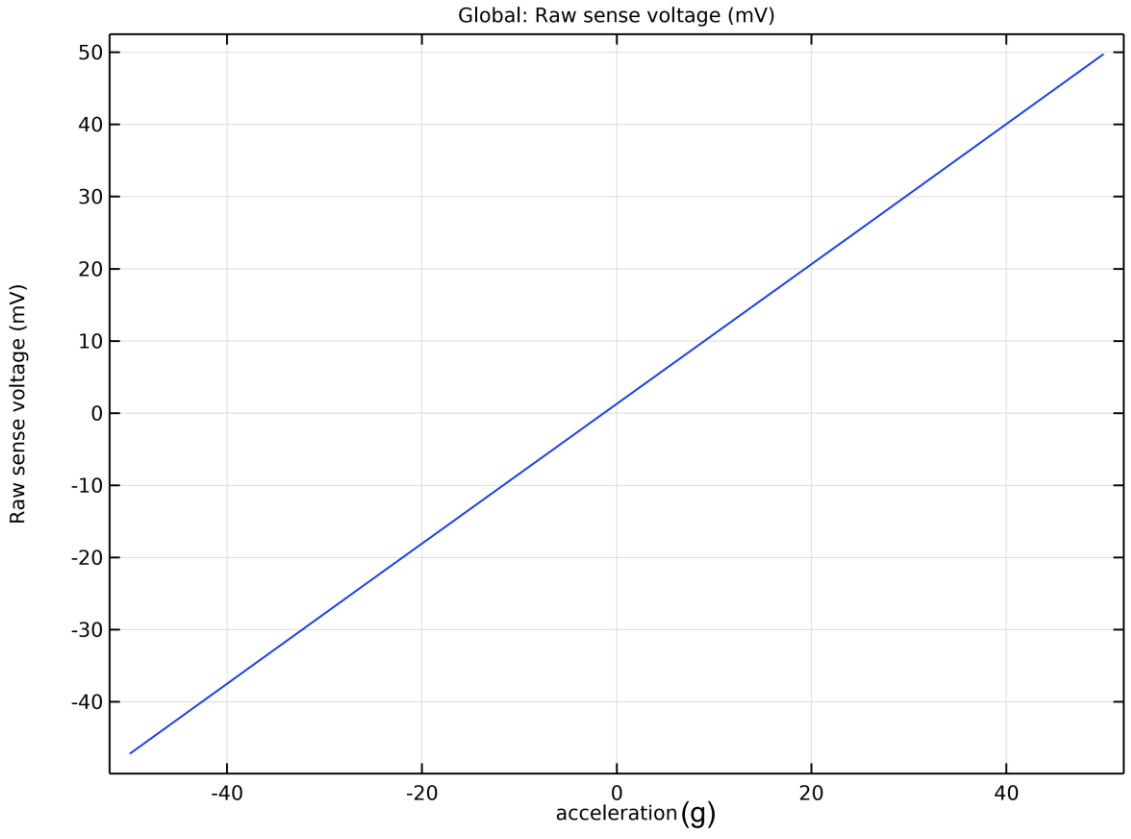

Figure 3-3 Voltage That is Being Sensed Versus Acceleration Applied

The accelerometer that was included into the model was planned to be equipped with self-test electrodes that would allow the sensing element to be calibrated at the manufacturing facility. The proof mass is made to move by applying a biasing voltage of 2 volts to the stationary self-test fingers, The movable electrodes that are affixed to the seismic mass are situated on its sides. This causes the static charges to be found between both the fixed and moving fingers to exert an electrostatic force, which in turn will cause the proof mass to move.

Figure 3-4 depicts the displacement of the polysilicon seismic mass when the fixed self-test electrodes is provided with 0 V to on the left-hand side of the movable electrodes coupled to the seismic mass, when a 2 V biasing voltage is applied to the fingers located on the right-handed side of the moving electrodes. The displacement of the seismic mass is approximately 0.02 μm, a magnitude deemed adequate for the self-test's intended objectives. In the next section a method of interpolation which is called Akima interpolation utilized to approximate the error resultant from the fault to designed output before the fault. This is carried out by initiating a variety of faults related to fingers and spring of the proof mass to be as inputs of the interpolation.

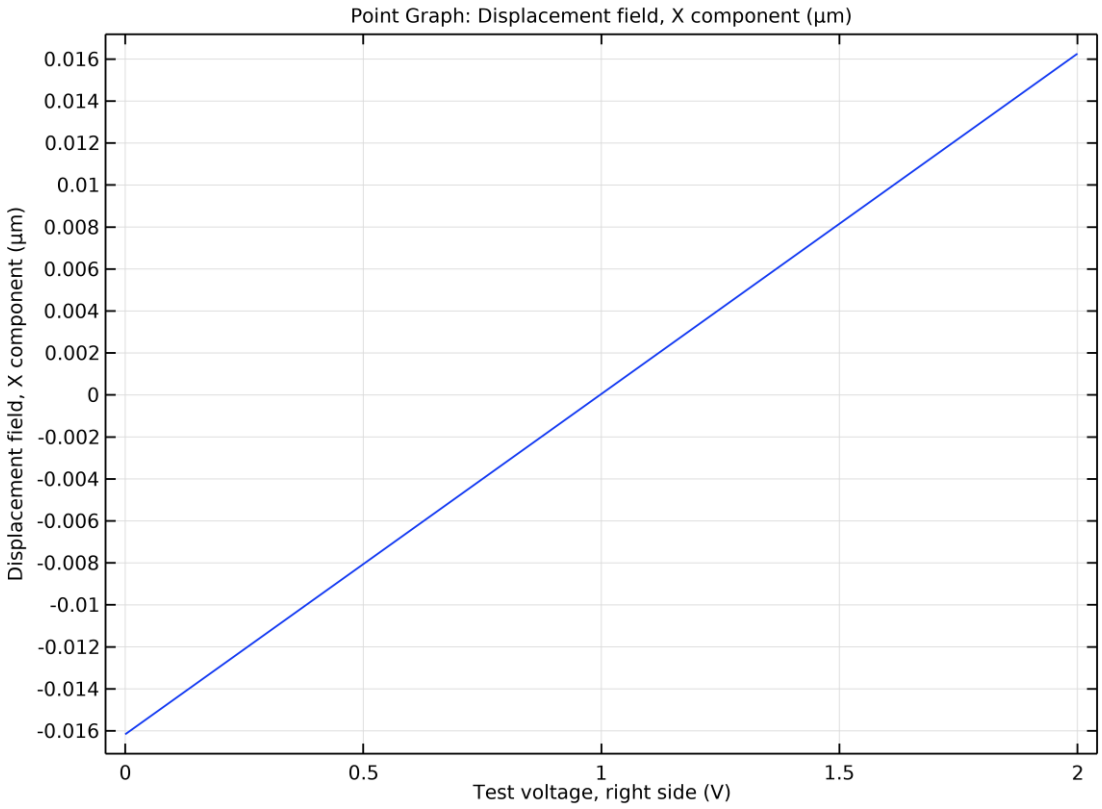

Figure 3-4 Self-Test Voltage Versus Displacement

3.3. Scaling of The NANO Sensing Element

The microscale sensing element can be converted to a nano scale by scaling its dimensions which are in microscale by modifying the dimensions to be in nanoscale. The only problem faced was the spaces between the fingers, where they are must be increased to a specific value to obtain the correct performance. The new design for this sensing element in nano scale is shown in figure 3-5.

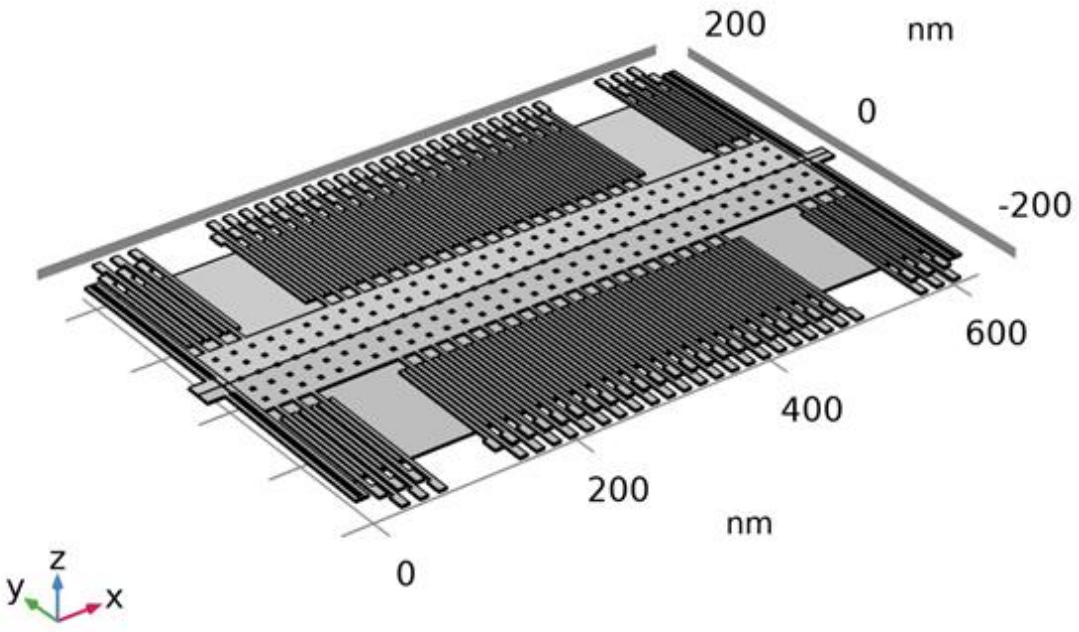

Figure 3-5 The Dual Axis (X,Y) Sensing NEMS Element

3.4. Failure Mechanism

Understanding the several ways in which a system might malfunction is essential for gaining a comprehension of the system's level of dependability. In the field of MEMS, there are numerous different failure mechanisms that have been identified as the principal causes of failure inside devices.

Mechanical fracture is when a single piece of material breaks into two different pieces. In MEMS, it generally causes the device to fail in a catastrophic way, though some designs may only have a small drop in performance. The most important kinds of failures are shown in table 3-2.

Table 3-2 Common MEMS Faults

Fault	Description
Ductile Fractures	Characterized by almost continuous plastic deformation of the material.
Brittle fractures	Occurs mostly on the flat surfaces of crystals and grows fast with little distortion.
Stiction	Because of their minute size, MEMS structures tend to adhere to one another via the action of surface forces.
Wear	Caused by the motion of one surface over another
Intercrystalline Fractures	happens when a polycrystalline material breaks along its grain boundaries, usually at a location where impurities or precipitates have accumulated.

All these faults' kinds can be found in all sensing element parts specially the fingers and spring attached to the proof mass. These changes in the fingers and spring will be compensated in the next section.

3.5. Compensation Voltage Calculation By GA

Fitness function will be calculated for our problem according to the inputs for the Genetic Algorithm (GA) which will be the compensation of the BIST voltage (stimulus) as follow:

$$r = mphplot(out,' pg4') \tag{3.1}$$

where (*r*) is the COMSOL structure of the MEMS, and (mphplot) is the MATLAB function to read the MEMS from COMSOL structure.

This (*r*) will be multiplied by the desired response for the MEMS as in equation 3.2:

$$F = r.d \tag{3.2}$$

The desired response is *d* is as in equation 3.10 below:

$$d = MA + c \tag{3.3}$$

where *A* the points that will be taken from the original response, *M* is the original (desired) response slope, *c* is the offset that given to the original response. Finally, by using the mean square, the error output will be as in equation 3.4:

$$Error = \frac{1}{N}\sum_{k=1}^{N}|d_k - F_k|^2 \tag{3.4}$$

The calculated fitness function can be used in (GA) to find the sufficient value of the BIST (DC test voltage) for the seismic mass displacement of as if the applied acceleration was (±50 g), i.e., the left and right test voltages (V_L, V_R). Then, the calculated left test voltage (V_L) is applied to the testing fingers (fixed fingers) to let seismic mass displaced for producing equal outputs if the acceleration is (+50 g) and the output will be compared with the desired responses (outputs) after the compensation that have been named as "Y_1", "Y_2", "Y_3", and so forth, were

determined through the application of a compensation algorithm (GA) and stored in the search table (lookup table) to be used by the interpolation of Akima. Similarly, the determined voltage (VR) for the right test is applied to a stationary test electrode in order to generate an output equivalent to an acceleration of (-50 g). If the comparison result is OK, then no decision will be taken. Otherwise, lookup table will calculate the voltage that to be fed back for the purpose of compensating (calibration) for the defect that occurred. The modified Akima interpolation method is a spline technique that is specifically designed to handle curves with quickly varying second derivatives in the field of applied mathematics. It is known for its ability to provide accurate and reliable curve fits in such cases. The Akima interpolation will run through all given points when given specific of "knot" end-points (x_i, y_i).

The structure of the sensing element in X and Y axis is shown in figure 3-6, while the Z axis sensing element is as shown in figure 3-7.

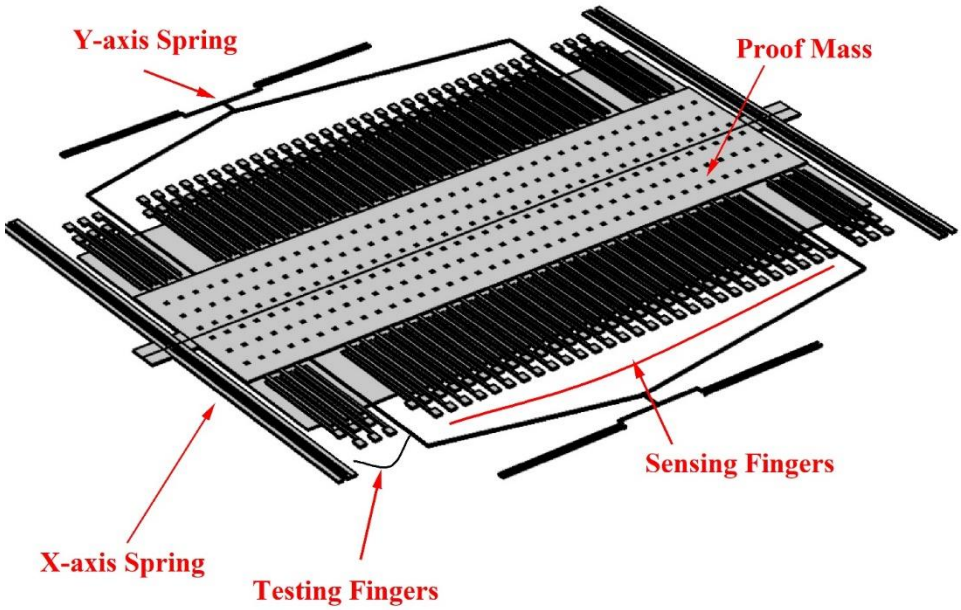

Figure 3-6 The Dual Axis (X,Y) Sensing MEMS Element

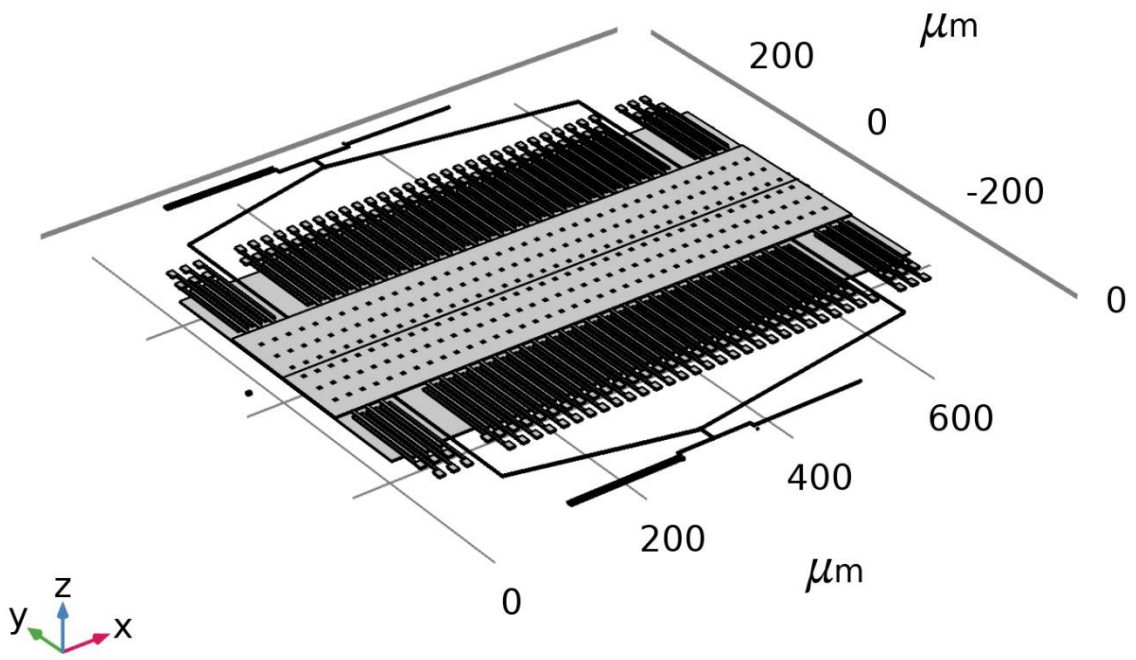

Figure 3-7 The Z Axis Sensing MEMS Element

The feedback system main part is suggested constitutes the electrostatic feedback effect, while the Built-In Self-Test (BIST) stimulus is converted into a physical actuation force. Consequently, the aforementioned system attributes, namely sensibility, the principle of dynamic range in addition to the linearity experience substantial impact. When a potential difference (V) across the detector's plates is applied, a field of attraction is generated between them, as described by the following equation 3.5 [33]:

$$F_{electrostatic} = \frac{C_o d_o {Y_n}^2}{2(do + x)^2} \tag{3.5}$$

In the given context, the symbol (d_0) represents the original separation between the two plates, (C_0) denotes the constant capacitance while (x) signifies the movement of the seismic mass beginning at that particular instant. As a result, the electrostatic force is related to voltage is a second-order and is modulated by displacement (x).

3.6. Method (1): Akima Interpolation Based

The underlying assumption suggests the fact that the local definition of the curve's gradient at a specific position and this method is dependent upon the utilization of the coordinates of five distinct points. The focal point serves as the central point, with a pair of points positioned on either side of it. The situation depicted in figure 3-8 illustrates five data points, specifically labelled as 1, 2, 3, 4, and 5.

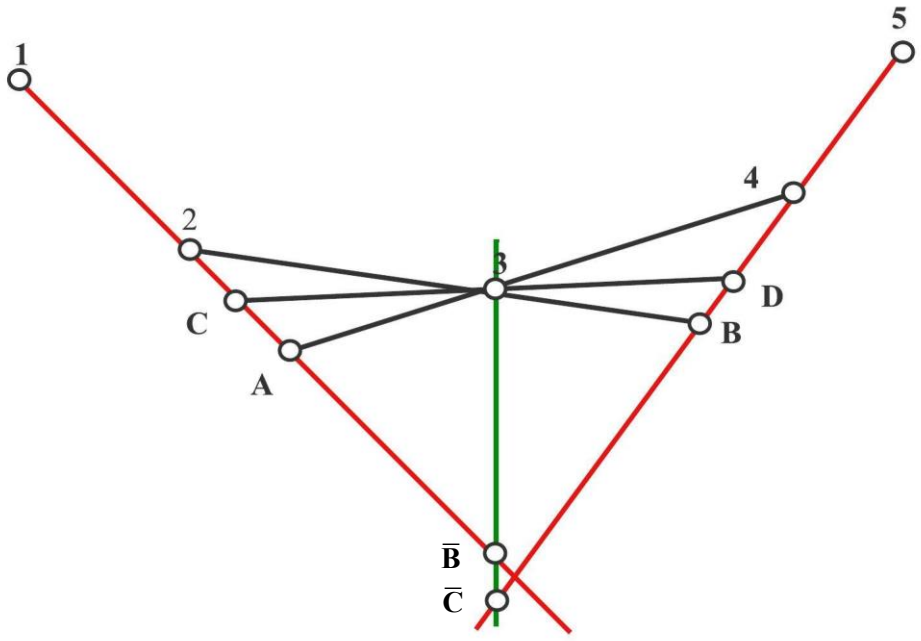

Figure 3-8 A Requirement That Must Be Satisfied in Order to Determine The Angle of a Parallel with The Graph

The line segment slope $\overline{CD}$, which is perpendicular to the curve at point 3, is defined by:

$$\left|\frac{\overline{2C}}{\overline{CA}}\right| = \left|\frac{\overline{4D}}{\overline{DB}}\right| \tag{3.6}$$

in which the intersection of the point of the two lines that have been drawn straight from the line segments $\overline{12}$ with $\overline{34}$ is has the letter A indication, same place that lines segments belong to $\overline{23}$ with $\overline{45}$ has the letter B indication, while the intersection coordinates of the two straight lines tangent being derived from and extended from line segments $\overline{12}$ in addition to $\overline{45}$ which are indicated by the letters C and D.

A plus or minus sign is used to symbolically represent the lengths of segments of two-line that are along on a straight path, based on whether they have the same meaning. Next, $\overline{\mathrm{CD}}$'s slope will be calculated under the equation 3.6. It will be convenient to refer to the vertices coordinates 1, 2, 3, 4, 5, A, B, C, in addition to D in figure 3-8 using the notation (x, y), which has the subscripts labelling of the following: 1, 2, 3, 4, 5, a, b, along with c, respectively, as well as the subscripts themselves. Some parameters have been specified as follows for clarity:

$$a_i = x_{i+1} - x_i \qquad (i = 1,2,3,4) \tag{3.7}$$

$$b_i = y_{i+1} - y_i \qquad (i = 1,2,3,4) \tag{3.8}$$

For convenience, it will be referred to such slopes of $\overline{12}$, $\overline{23}$, $\overline{34}$, $\overline{45}$, and $\overline{\mathrm{CD}}$ as Y_1, Y_2, Y_3, Y_4, and t, accordingly. This means:

$$Y_i = \frac{(y_{i+1} - y_i)}{(x_{i+1} - x_i)} = b_i/a_i (i = 1,2,3,4) \tag{3.9}$$

$$t = \frac{(y_d - y_c)}{(x_d - x_c)} \tag{3.10}$$

Then, it is abundantly apparent in figure 3-8 that the subsequent equations ought to hold:

$$\frac{(y_a - y_2)}{(x_a - x_2)} = \frac{(y_c - y_2)}{(x_c - x_2)} = \frac{b_1}{a_1} \tag{3.11}$$

$$\frac{(y_4 - y_b)}{(x_4 - x_b)} = \frac{(y_4 - y_d)}{(x_4 - x_d)} = \frac{b_4}{a_4} \tag{3.12}$$

$$\frac{(y_3 - y_a)}{(x_3 - x_a)} = \frac{b_3}{a_3} \tag{3.13}$$

$$\frac{(y_b - y_3)}{(x_b - x_3)} = \frac{b_2}{a_2} \tag{3.14}$$

$$\frac{(y_3 - y_c)}{(x_3 - x_c)} = \frac{(y_d - y_3)}{(x_d - x_3)} = t \tag{3.15}$$

Applying equations 3.14 and 3.15, the following equation will be obtained,

$$\frac{[(y_3 - y_a) - b_2]}{[(x_3 - x_a) - a_2]} = \frac{b_1}{a_1} \tag{3.16}$$

By removing $(y_3 - y_a)$ from (3.11), the following result is obtained:

$$\frac{(x_3 - x_a)}{a_3} = \frac{(a_1 b_2 - a_2 b_1)}{(a_1 b_3 - a_3 b_1)} \tag{3.17}$$

This result is obtained by using the exact identical steps that have been obtained when equation 3.17 using equation 3.11 and equation 3.13 [62]:

$$\frac{(x_b - x_3)}{a_2} = \frac{(a_3 b_4 - a_4 b_3)}{(a_2 b_4 - a_4 b_2)} \tag{3.18}$$

$$x_3 - x_c = \frac{(a_1 b_2 - a_2 b_1)}{(a_1 t - b_1)} \tag{3.19}$$

$$x_d - x_3 = \frac{(a_3 b_4 - a_4 b_3)}{(b_4 - a_4 t)} \tag{3.20}$$

Considering that equation 3.6 may be expressed as:

$$\begin{aligned} &| \, [(x_3 - x_c) - a_2]/[(x_3 - x_a) - (x_3 - x_c)] \, | \\ &= |[a_3 - (x_d - x_3)]/[(x_d - x_3) - (x_b - x_3)]| \end{aligned} \tag{3.21}$$

this can be achieved by removing $(x_3 - x_a), (x_b - x_3)$, $(x_3 - x_c)$, and $(x_d - x_3)$ from 3.13 to 3.16, then formula for a quadratic equation will be in the form:

$$|S_{12}S_{24}|(a_3t - b_3)^2 = |S_{13}S_{34}|(a_2t - b_2)^2, S_{ij} = a_ib_j - a_jb_i(i \neq j) \tag{3.22}$$

The fact that points 2 and 4 have to be located on the same side of the tangent that is drawn to the curve at point 3 is a prerequisite. Therefore, it stands to reason that the two points must be next to one another:

$$(a_2t - b_2)(a_3t - b_3) \leq 0 \tag{3.23}$$

Because of this, the following equation will be obtained:

$$|S_{12}S_{24}|^{\frac{1}{2}}(b_3 - a_3t) = |S_{13}S_{34}|^{\frac{1}{2}}(a_2t - b_2) \tag{3.24}$$

Solving this equation, we obtain:

$$t = (w_2b_2 + w_3b_3)/(w_2a_2 + w_3a_3) \tag{3.25}$$

where,

$$w_2 = |S_{13}S_{34}|^{\frac{1}{2}} \tag{3.26}$$

$$w_3 = |S_{12}S_{24}|^{\frac{1}{2}} \tag{3.27}$$

This is a simplified analytical formulation of the slope of $\overline{\mathrm{CD}}$, which was calculated under the equation 3.6. In addition to this, equations 3.25-3.27 may also be stated as:

$$t = \frac{(w_2'm_2 + w_3'm_3)}{(w_2' + w_3')} \tag{3.28}$$

where

$$w_2' = (\,sign\ of\ a_2)|(Y_3 - Y_1)(Y_4 - Y_3)|^{\frac{1}{2}} \tag{3.29}$$

$$w_3' = (sign\ \ of\ a_3)|(Y_2 - Y_1)(Y_4 - Y_2)|^3 \tag{3.30}$$

Note that for the case of a function with a single value, it is always possible to make a_2 and a_3 positive. Equation 3.6 is invariant by linear coordinate system transformations, including scaling and rotation, since it is geometrical. It follows from 3.28-3.30 and the geometrical structure indicated by equation 3.1 that the slope of *t* relies on four slopes of secants only, i.e., on the numbers m_l, m_2, m_3, and m_4, and its interval widths are independent.

From equations 3.28–3.30 it is clear the facts that $Y_1=Y_2$, $Y_3\neq Y_1$, and $Y_4\neq Y_3$ imply that $t = Y_1 = Y_2$, and similarly, the facts that $Y_3= Y_4$, $Y_1\neq Y_2$, and $Y_4\neq Y_2$ imply that $t = Y_3= Y_4$: these are features that are quite desired. When $Y_1=Y_2= Y_3$ or when $Y_2= Y_3=Y_4$, t is undefined by equation 3.22; however, this problem can be readily addressed by taking $t=Y_2=Y_3$ for such situations as a natural and logical extension.

It may be deduced from equations 3.28 and 3.30 that $t =Y_2$ when $Y_2= Y_4$, $Y_3 \neq Y_1$, and $Y_4 \neq Y_3$, and that $t =Y_3$ when $Y_3=Y_l$, Y_2 is $\neq Y_1$, and $Y_4 \neq Y_2$. These characteristics are in no way desirable and should in no way be anticipated. Perhaps changing weighting factors w_2' in addition to w_3' in 3.28 to be read as zero is the easiest method to get rid of these annoying characteristics is to use a single-valued expression in place of equation 3.29 and equation 3.30.

$$w_2' = |Y_4 - Y_3| \tag{3.31}$$

$$w_3' = |Y_2 - Y_1| \tag{3.32}$$

Equation 3.6 retains most of its favorable qualities with this change. Just the coordinate system's invariance under rotation is lost. Interpolation of a single-valued function doesn't need rotation invariance.

Finally, the derivative of Akima computed at x_i may be defined as:

$$t_i = \frac{|Y_{i+1} - Y_i|Y_{i-1} + |Y_{i-1} - Y_{i-2}|Y_i}{|Y_{i+1} - Y_i| + |Y_{i-1} - Y_{i-2}|} \tag{3.33}$$

3.7. Interpolation of Akima with Modifications

The method used by Akima undoubtedly yields appealing outcomes. Akima's formula gives non identified when the lower and higher slopes are identical, $w'_{i-2} = w'_{i-1}$, and also the denominator and numerator are 0. For this extreme scenario, Akima suggested averaging the lower and higher slopes as $t_i = \frac{w'_{i-1} - w'_i}{2}$.

If the data seems to be constant for more than two consecutive nodes, then the Akima interpolation might indeed produce an overshoot. This was a deliberate choice that was made in order to demonstrate yet another property of the Akima interpolation. In a great number of technical applications, this specific kind of overshoot is not something that is desired.

The weights in Akima's derivative formula need to be adjusted so that overshoot can be eliminated, and edge situations in which the numerator and the denominator are both equal to 0 can be avoided by simply adjusting some of the weights m_1 and $m_2$related to the slopes $w'_{i-1}$and w'_i. Then:

$$t_i = \frac{Y_1}{Y_1 + Y_2} w'_{i-1} + \frac{Y_1}{Y_1 + Y_2} w'_i \tag{3.34}$$

$$Y_1 = \frac{|w'_{i+1} - w'_i| + |w'_{i+1} + w'_i|}{2} \tag{3.35}$$

$$Y_2 = \frac{|w'_{i-1} - w'_{i-2}| + |w'_{i-1} + w'_{i-2}|}{2} \tag{3.36}$$

Thus, according to equation 3.34 and equation 3.35 the overshoot is eliminated in the case of constant consecutive input values as it is shown in figure 3-9.

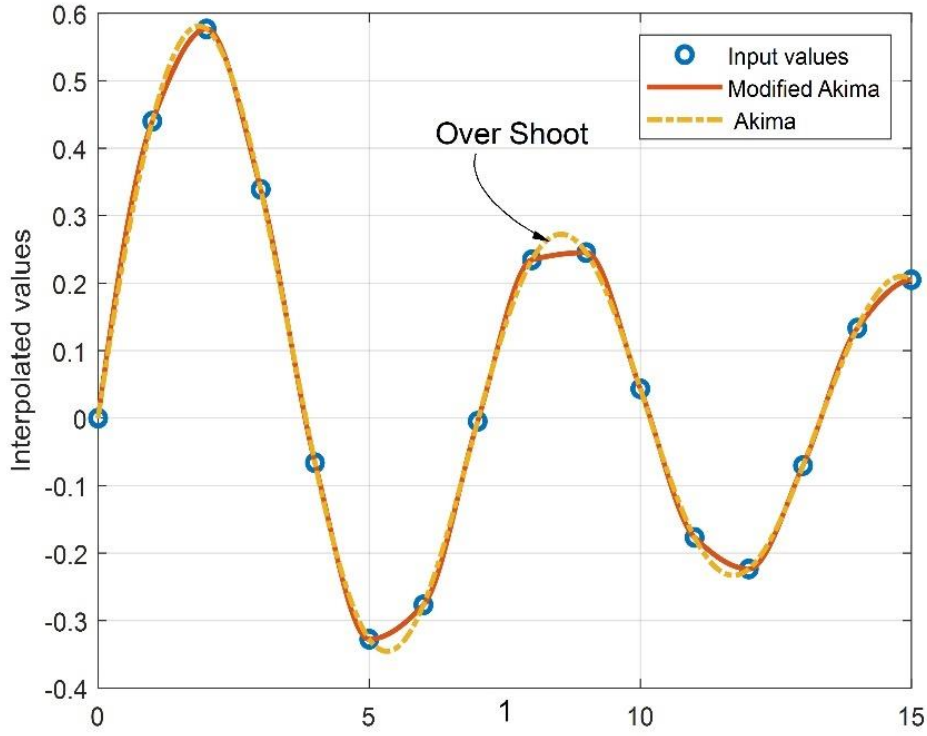

Figure 3-9 Over Shoot of Akima Elimination

3.8. Method (2): A Sigma-Delta Modulation Based

In this calibration method, the same Akima interpolation algorithm used in method (1) in addition to the removing of the noise like Brownian, resulted from random motion of material particles in the proof mass and sensing fingers, amplification, switching, quantization noise sources. The essential idea that underlies

Sigma-Delta (ΣΔ) converters is that these noise sources are removed through oversampling, error of the processing, as well as feedback with the goal of improving the efficiency and accuracy of a quantizer. The Analog-To-Digital Converter (ADC) represents a device utilized for the conversion of analogue signals, characterized by their continuous nature in both time and amplitude, into digital signals, which are discrete in nature. This device is specifically designed for the conversion of low-pass signals. In its most basic form, it is comprised of an antialiasing filtering, a sampling circuitry, and a quantizer.

3.8.1. Method Description

As can be seen in figure 3-10, the most basic form of the ΣΔ architecture, known as a single-bit ΣΔ modulator with 1st-order, developed by employing a discrete-time integrator in the function of a loop type filter in conjunction with a comparator in order to get the desired result.

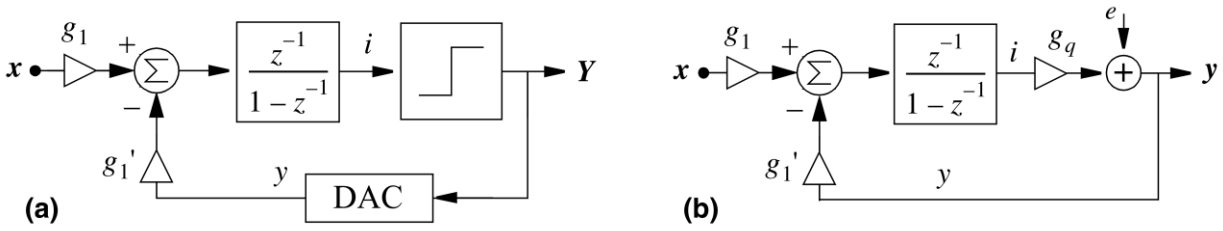

Figure 3-10 Single -Bit First -Order ΣΔ Modulator (a) General Circuit (b) Linear Circuit

The following prerequisite must be met to be able to achieve the quantization error's first-order shaping:

$$g_1' g_q = 1 \Rightarrow Y(z) = \frac{g_1}{g_1'} \cdot z^{-1} X(z) + (1 - z^{-1}) E(z) \qquad (3\ 37)$$

After the Akima interpolation, the $X(z)$ will be ($X(z) \pm Y_n$) and the equation 3.38 will be:

$$g_1' g_q = 1 \Rightarrow Y(z) = \frac{g_1}{g_1'} \cdot z^{-1}(X(z) \mp Y_n) + (1 - z^{-1})E(z)$$
$$= \frac{g_1}{g_1'} \cdot z^{-1}\, X(z) \mp \frac{g_1}{g_1'} \cdot z^{-1}\, \mathrm{Y_n} + (1 - z^{-1})E(z) \tag{3.38}$$

The quantization error for the inside the band signal and the change in dynamic range are determined, respectively:

$$P_Q \approx \frac{\Delta^2}{12} \cdot \frac{\pi^2}{3OSR^3} \tag{3.39}$$

$$DR|_{dB} \approx 10log_{10}\left(\frac{3}{2} \cdot \frac{3OSR^3}{\pi^2}\right) \tag{3.40}$$

where OSR is the Over Sampling Ratio and Δ is the quantization step.

The main disadvantage of this modulator is that in order to achieve medium resolutions, extremely large oversampling frequencies are needed, which is not feasible because the dynamic range increases by only 1.5 bits per octave when employing an OSR. Because of this, it cannot be used in any applications requiring a medium or high frequency. The model of a ΣΔ modulator of linear form may be solved analytically and utilized to understand the system and anticipate its performance.

Equations 3.39 to 3.40 assume that the error in quantization is independent of the input signal and fluctuates at a random rate in order to determine the efficiency of the 1st-order ΣΔ modulator. Nevertheless, if a DC signal is fed into the first-order modulator as the input, the output will oscillate between the two levels (±Δ/2), attempting to maintain its mean value at the same level as the input despite the presence of repeating patterns.

The consequence of this phenomenon is the occurrence of a quantization error with coloration, as opposed to a neutral or white error. Moreover, the magnitude of the error in the signal band may surpass the expected value as projected by the linear model, especially when the recurring frequency is located inside the signal frequency range. The reason for this phenomenon is that an error in quantization exhibits a colored rather than white characteristic. The aforementioned impact is observable in figure 3-11, in which the within the band error in quantization power for a first-order single-bit ΣΔ modulators are depicted. The modulator is designed to accommodate direct current (DC) inputs within the restricted range spanning from the negative half of the amplitude (Δ/2) to the positive half of the amplitude (+Δ/2). The pattern noise of the ΣΔ modulator is a sort of representation that describes situations like this. Both the quantization error along with the modulator inputs exhibit a correlation, as evidenced by the curves and spectral output of the initial ΣΔ modulator. It's important to keep in mind that this association might cause the modulator's output spectrum to significantly vary from. To combat this, a non-periodic signal with a Signal to Noise Ratio (SNR) of ΣΔ modulator is often added to the quantizer's input. The implementation of oversampling can partially mitigate the impact of quantization error on the input signal. However, it is important to note that this approach introduces additional design complexity as a trade-off.

The potential instability in a 1st-order feedback system, similar to other feedback systems, is contingent upon the dynamics of the feedback. If, given bounded inputs and any starting condition of the integrator, the internal state variables of a ΣΔ modulator continue to be bounded throughout the course of time, then it can be said that the ΣΔ modulator is stable.

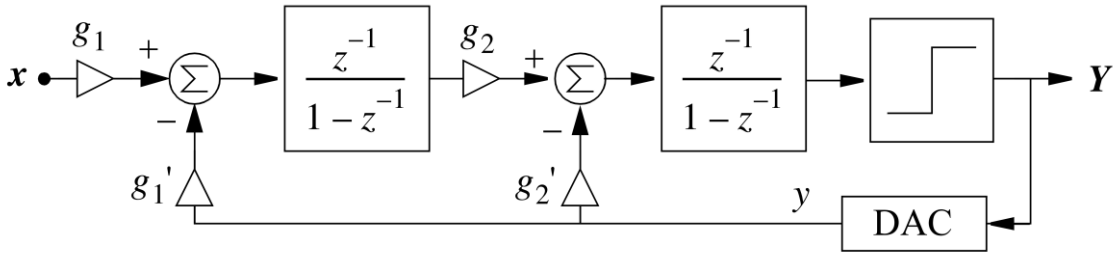

Figure 3-11 Architecture of Second-order ΣΔ modulator

3.8.2. Second-order ΣΔ Modulator

The architectural design of a second-order Sigma-Delta modulator (ΣΔ) is derived from the substitution of the quantizer in a first-order Sigma-Delta modulator (ΣΔ) with a first-order modulator. The design depicted in figure 3-11 illustrates the single-bit example. Additionally, supposing the comparator of a linear model, the following results from the output of the modulator in the z-domain will be obtained:

$$Y(z) = \frac{g_1 g_2 g_q z^{-2} X(z) + (1 - z^{-1})^2 E(z)}{1 + \left(g_2' g_q - 2\right) z^{-1} + \left(1 + g_1' g_2 g_q - g_2' g_q\right) z^{-2}} \tag{3.41}$$

So, in order to have a pure 2nd-order shaping, the following requirements need to be satisfied:

$$\left.\begin{array}{l} g_1{}' g_2 g_q = 1 \\ g_2{}' = 2 g_1{}' g_2 \end{array}\right\} \Rightarrow Y(z) = \frac{g_1}{g_1{}'} \cdot z^{-2} X(z) + (1 - z^{-1})^2 E(z) \tag{3.42}$$

E(z) is the quantization noise z-transform.

Equation 3.43 will represent the Akima interpolation in this particular case.

$$Y_1(z) = \frac{g_1 g_2 g_{q1} z^{-2} (X(z) \pm Y_n) + (1 - z^{-1})^2 E_1(z)}{1 + \left(g_2' g_{q1} - 2\right) z^{-1} + \left(1 + g_1' g_2 g_{q1} - g_2' g_{q1}\right) z^{-2}} \tag{3.43}$$

$$= \frac{g_1 g_2 g_{q1} z^{-2} X(z) \pm g_1 g_2 g_{q1} z^{-2} Y_n + (1 - z^{-1})^2 E_1(z)}{1 + (g'_2 g_{q1} - 2) z^{-1} + (1 + g'_1 g_2 g_{q1} - g'_2 g_{q1}) z^{-2}}$$

It is crucial to consider that, despite the implementation of the requirements specified in equation 3.43, the integrator weights in a second-order ΣΔ modulator still retain their status as free parameters and maintain their functionality. Several design considerations need to be made before making the right choice for these free coefficients.

The utilization of two integrators in this modulator contributes to the improved decoupling of the error in quantization in the input signal, as well as the expansion of the device's dynamic range. Furthermore, the linear model offers a more precise estimation of the error in quantization within the stable input range.

Indeed, it is a factual observation that augmenting the modulator order results in a heightened level for decorrelation within the error in quantization as well as the input signal. The utilization of system noise as a shifting signal in practical implementations is highly beneficial in reducing the potential impact of quantization error-induced coloring.

3.8.3. ΣΔ Modulator with High-Order

The quickest and easiest approach to extending a ΣΔ modulator towards arbitrary-order filtering by including integrators before to the quantizer. If the linear model to be used, the output would be predicted as:

$$Y(z) = \frac{g_1}{g'_1} \cdot z^{-L} (X(z) \mp Y_n) + (1 - z^{-1})^L E(z) \qquad (3.44)$$

3.8.4. Architecture of Cascaded ΣΔ modulator

As previously mentioned, the utilization of single-loop ΣΔ modulators for high-order filtering presents challenges in terms of instability and a notable decline in performance compared to an ideal modulator.

The proper functioning of cascade ΣΔ modulators is dependent on the appropriate digital processing of the outputs of the stages in the cascade. Let's have a look at the third-order cascade shown in figure 3.12 so it can be seen how its influence works. The architecture of the modulator can be classified as a 2-1 cascade Sigma-Delta modulator, as it comprises a primary stage second-order Sigma-Delta modulator in conjunction with a secondary stage first-order Sigma-Delta modulator, both indicated by dashed boxes.

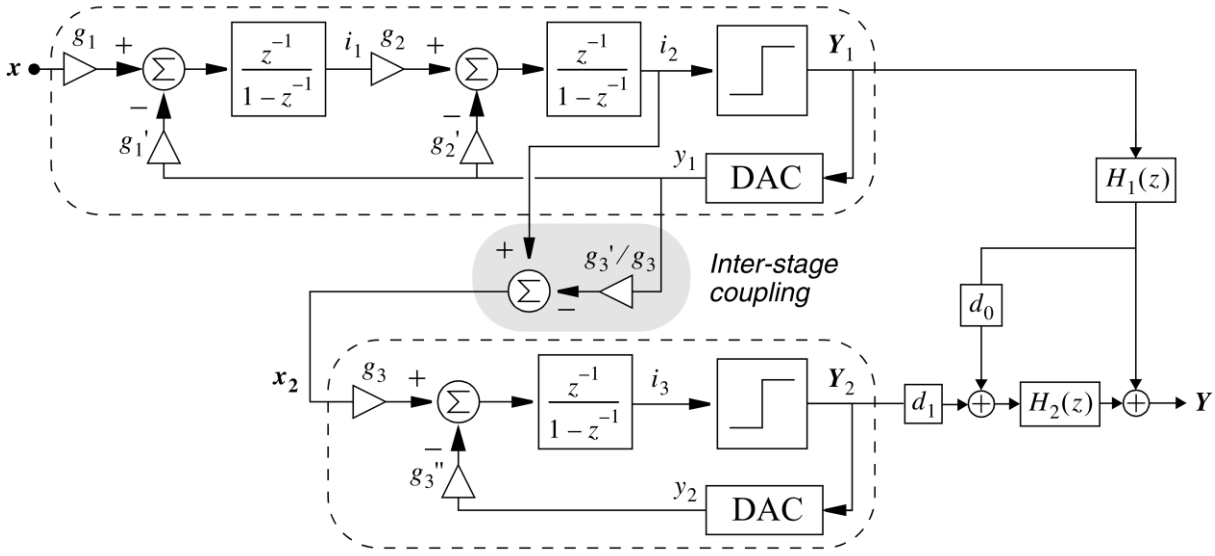

Figure 3-12 ΣΔ Modulator Cascading Utilizing Third-Order Second-Stage

When analyzed using linear methods, the result that the first stage's output produces in the domain is:

$$Y_1(z) = \frac{g_1 g_2 g_{q1} z^{-2}(X(z) \mp Y_n) + (1 - z^{-1})^2 E_1(z)}{1 + \left(g_2' g_{q1} - 2\right)z^{-1} + \left(1 + g_1' g_2 g_{q1} - g_2' g_{q1}\right)z^{-2}} \qquad (3.45)$$

3.8.5. The Decimation Filter

Processing of the oversampled digital output of a one-bit sigma-delta reading circuit is imperative due to the presence of high-frequency signals additive noise and a significantly high data rate. Decimation filters are frequently utilized to effectively eliminate high-frequency noise, eliminate unnecessary output data, while decreasing data rate.

Sinc filters are often used for the purpose of realizing decimation filters due to the low-pass quality of these filters as well as the ease with which they can be implemented. Both subtraction and addition blocks are the building blocks of sinc filters, which are low-pass filters. Figure 3-13 presents a diagram depicting the construction of a Sinc filter. Blocks that do addition add the input to the result of the previous addition, while blocks that perform subtraction remove the input from the input that is coming in.

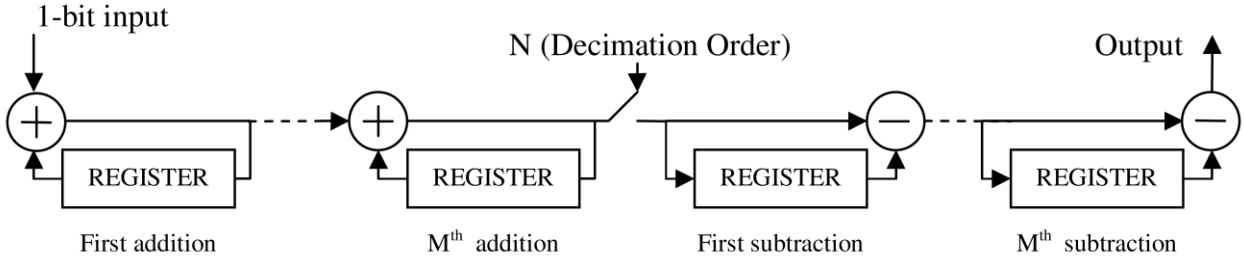

Figure 3-13 Sinc Filter Construction

The decimation filter sequentially processes a 1-bit input through a series of addition blocks, beginning with the first block and continuing until the M_{th} block. One of the outputs generated by the M_{th} addition block is directed towards the initial subtraction block, and then proceeds to propagate through the subsequent blocks in a sequential fashion until it reaches the M_{th} subtraction block. The variable M is used

to represent the degree of the decimation filter, while N is used to denote its decimation order. The establishment of transfer functions for the subtraction and addition blocks illustrated in figures 3-14 and 3-15 is deemed essential. The transfer function representing the addition block in the Z-domain is given by equation 3.46.

$$\begin{aligned} y(n) &= x(n) + y(n-1) \\ Y(z) &= X(z) + Y(z)z^{-1} \\ \frac{Y(z)}{X(z)} &= \frac{1}{1 - z^{-1}} \end{aligned} \tag{3.46}$$

Figure 3-14 Sinc Filter Addition Block

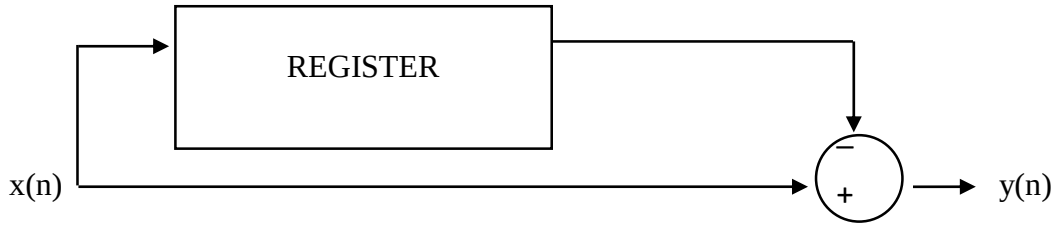

Figure 3-15 Sinc Filter Subtraction Block

Equation 3.47 gives Z-domain subtraction block function.

$$y(n) = x(n) - x(n-1)$$
$$Y(z) = X(z) - X(z)z^{-1}$$
$$\frac{Y(z)}{X(z)} = 1 - z^{-1} \quad (3.47)$$

The parameters M and N of the Sinc filter play a critical role. The degree of the system used in the closed-loop sigma-delta modulator in microelectromechanical systems (MEMS) is determined by the bandwidth, which in turn depends on the values of M and N. system Enhanced filtration of high-frequency noise is achieved by reducing the ripple at high frequencies through an increase in the degree of the Sinc filter.

3.8.6. Capacitive ΣΔ MEMS Accelerometer Noise Sources

A its known, MEMS accelerometer has the mechanical and electrical components that are combined in these systems. The performance of the system as a whole is negatively impacted by the individual sounds that are introduced by each of these components. The determination of the resolution of a capacitive accelerometer system is predominantly influenced by noise sources, that are typically categorized into two categories: mechanical or electrical in origin.

3.8.6.1 MEMS Mechanical Noise Source

The mechanical structure of the capacitive accelerometer is made up of springs, proof mass, and electrodes that are set in place. The mechanical noises referred to as Brownian noise is a result of the thermal motion exhibited by gas molecules within the given mechanical form. The auditory disturbance is generated by the internal mechanical constituents of this particular mechanical configuration. The key factors that contribute to Brownian noise are the temperature, the damping coefficient of the accelerometer, and the seismic masses.

Using equation 3.48, the Brownian noise can be calculated which produced by a capacitive accelerometer. The frequency terms in the derivation of Brownian noise can be disregarded because the sampling frequency of the employed accelerometer system is considerably higher than the accelerometer bandwidth.

$$B_n = \frac{\sqrt{4K_T Tb}}{9.8m} \tag{3.48}$$

where K_T is the Boltzman constant, T is the temparature and b is the damping of the accelerometer.

The mitigation of Brownian noise could be achieved through two approaches: reducing the coefficient of damping or augmenting the seismic mass within the system. The use of vacuum packing is one method for reducing the damping factor; however, the use of vacuum packaging will cause problems with the package's stability.

3.8.6.2 MEMS Electrical Noise Source

The integration of the accelerometer with the interface electronics results in the introduction of electrical noises into the system. Thermal noise and quantization noise are the two types of electrical noise that are produced by interface electronics. Both noises are caused by the process of converting analog to digital. The provision of feedback force induces oscillation in the seismic mass, leading to the generation of residual motion noise in closed loop operations.

3.8.6.3 Amplification Noise

A sigma-delta readout circuit is the source of the amplifier's noise, which includes the thermal and flicker noise that the amplifier produces when it is connected to the readout circuit. In order to eliminate the flicker noise produced by the amplifier, the

Correlation Double Sampling (CDS) approach may be implemented in the readout circuit. During the feedback phase, the CDS technique is employed to sample noise and offset on the CDS capacitors. Following this, in the subsequent sensing phase, measures are taken to eliminate flicker noise and offset. The utilization of the Common-Mode Feedback (CMFB) technique results in thermal noise being the predominant source of noise generated by the amplifier. The equation for this is as follows:

$$V_{out\,-\,thermal} = \sqrt{\frac{16}{3}\frac{C_s + C_p}{C_{int}}\frac{k_b T}{C_{out}}\frac{1}{f_s}} \tag{3.49}$$

where the variable C_s denotes the numerical value of the sensing capacitance associated with the accelerometer, The variable C_p is used to denote the parasitic capacitance, C_{int} represents the capacitance of integration, C_{out} represents the capacitance of the output, f_s represents the frequency of sampling, and V_{out} represents the amplifier noise (volts / hertz). As can be seen from equation 3.49, the amount of noise produced by an amplifier can be reduced by raising the sampling frequency.

3.8.6.4 Switching Thermal Noise kT/C

The phenomenon under discussion is commonly referred to as thermal noise, which is produced by switches that are utilized in the reading circuit. The generation of electrical noise source is a notable phenomenon, and its importance is primarily influenced by the integration capacitance's magnitude in conjunction with the sampling frequency, as demonstrated in equation 3.50.

$$V_{out\,\_\_kT/C} = \sqrt{\frac{4k_b T}{f_s C_{int}}} \tag{3.50}$$

3.8.6.5 Quantization Noise

Under conditions of closed loop operation, quantization noise can be effective. The process of converting analog to digital in the readout circuit results in the production of this noise source. The quantization noise in an oversampled sigma-delta modulator is primarily influenced by the oversampling ratio, as it causes a shift in quantization at higher frequencies. This effect becomes more pronounced as the oversampling ratio increases and can be calculated using equation 3.51.

$$Quantization\_noise = e_{rms}\frac{\Pi^{n}}{M^{n+0,5}\sqrt{2n+1}} \tag{3.51}$$

where, $e_{rms} = \frac{\Delta}{\sqrt{12}}$, M is the ratio of the oversampling and the order of the sigma-delta modulator is n.

Two techniques for reducing quantization noise are increasing the oversampling percent or even the decimation order of the decimation filter.

3.8.6.6 Mass Residual Motion Noise

The electromechanical sigma-delta device can use mass residual motion well when it is working in a closed loop. In the context of closed loop operation, the proof mass exhibits oscillatory motion around the equilibrium point due to the input received from the pulsed train output of the sigma-delta reading circuit.

Even with no input, this oscillation continues to occur. This evidence mass's periodic motion is considered to be a source noise and is referred to as noise of the seismic mass residual motion. For accelerometers that have a modest proof mass and a wide operational range, this noise source predominates. Equation 3.52 can be used to compute mass residual motion.

$$N_{rm} = 4\frac{f_{BW}}{f_s}\left(\frac{K}{M}\right)\frac{a_{fb}}{(2\pi f_s/4)^2} \tag{3.52}$$

where a_{fb} is the feedback in terms of acceleration, f_{BW} represents the input signal bandwidth, f_s represents frequency of sampling, K is the accelerometer's constant of the spring, M is the seismic mass, while N_{rm} represents the residual movement of the seismic mass noise.

3.9. The Proposed Sigma-Delta Modulator (ΣΔ) System Model

The model of the whole accelerometer system is presented in this section. The model was created in such a way that it may be modified to accommodate a variety of designs for the accelerometer, readout, and decimation filter. The model that has been made can be used to estimate how well different types of accelerometer systems work as a whole. This model lets the user change important design parameters, which lets them see how these parameters affect the system's total performance. Figure 3-16 provides a representation of the full model for the accelerometer calibration system.

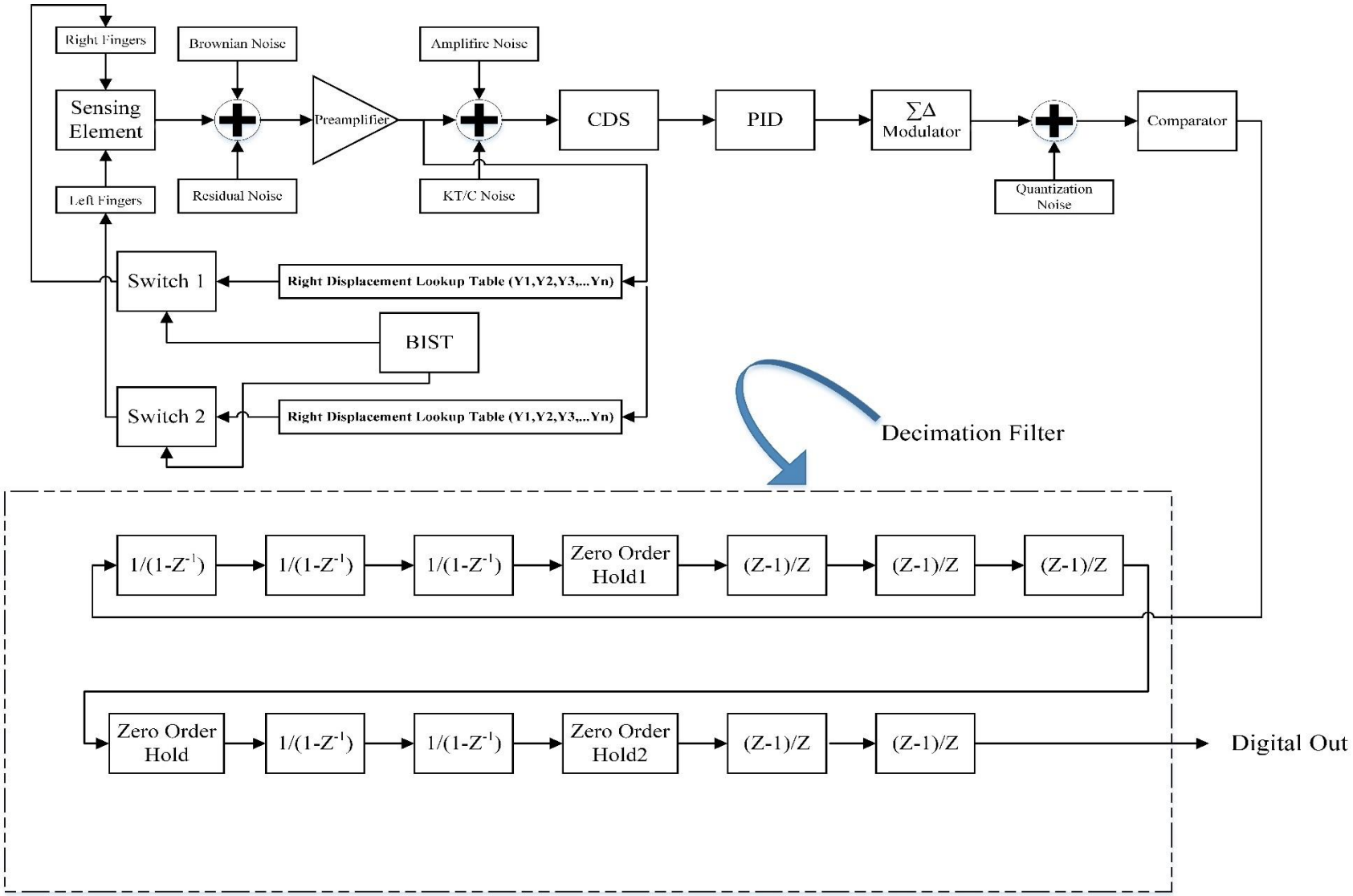

Figure 3-16 Sigma-Delta Modulator of the MEMS Capacitive Accelerometer

3.10. The Method of Calibration

The calibration method utilized here is the Akima interpolation as in the section 3.5 of this chapter. The calculated values of (V_L, V_R) in COMSOL can be used to find the sufficient value of the (BIST) (DC test voltage) for the seismic mass displacement in the case if the acceleration applied was (±50 g), i.e., the left and right test voltages (V_L, V_R). Then, the calculated left test voltage (V_L) is applied to the testing fingers to obtain the seismic mass displacement for getting output equal if the acceleration applied was (+50 g). Then the output will be compared with the desired compensated outputs named compensation that have been named as "Y_1", "Y_2", "Y_3", and so forth, were determined through the application of a compensation algorithm (GA) and stored in the look up table shown in figure 3-17 to be used by interpolation of Akima. Similarly, the calculated right test voltage (V_R) is applied to fixed test electrode to obtain output equal to that if the acceleration is (-50 g). If the comparison result is OK, then no decision will be taken. Otherwise, lookup table will calculate the voltage that to be feedback for the purpose of compensating (calibration) for the defect that occurred.

3.11. Method (3): Three Axis MEMS Calibration Using Kalman Filter and Delaunay Triangulation Algorithm

A Kalman filter is an efficient and effective recursive data processing technique. It analyses all of the data that are available, regardless of how precise they are, to obtain an estimate of the present value of the variables that are of interest by using the following:

- A comprehension of the dynamics of both the system and the measuring device.
- Uncertainty in dynamic models, as a result of noise in the system, inaccurate measurements, and other sources, are statistically described.

- Any data that can be gathered on the starting points of the relevant variables.

To provide a statistically accurate estimate of the target variables, Kalman filter integrates all available measurement data with previous knowledge about the system and measuring equipment. The aim of this method is to use a series of mathematical equations to clean up the raw acceleration data from the Inertial Measurement Unit (IMU) and arrive at an accurate approximation of the process's current condition with as little inaccuracy as possible.

3.11.1. Method description

Gravity-based techniques can be used in the field with ease because they do away with the need for additional equipment in the case of an accelerometer. In contrast, to hand, calibrating a gyroscope with a turntable or other external device restricts the sensor's ability to be reliably calibrated inside the field and increases overall costs. An accelerometer, gyroscope, and the magnetometer are all integrated onto a single chip in the MPU6050 sensor used as an example. Inertial sensor businesses are increasingly attempting to merge numerous sensors onto the single chip in order to further decrease both the size and cost of their products as MEMS technology continues to progress.

In this research, a calibration algorithm is suggested for IMU (MPU6050) that may be used in the field without any additional hardware. The process also requires less computation and can be applied physically.

The modelling of the accelerometer output is carried out in the same manner as the modelling of the gyroscope output. The scale factor, bias, and misalignment errors are also present in the gyro error components, which are comparable to those found in the static error components. In addition to this, the accelerometer has a problem with the error caused by the lever arm. The

following is one way to explain the information provided by the accelerometers when $\mathrm{M}_a \triangleq \mathrm{G}_a - \mathrm{E}'_a, \mathrm{G}_a \triangleq \mathrm{W}_a^{\mathrm{T}}$ are defined, respectively:

$$\tilde{A}^s = (G_a - E'_a)\overline{A^b} - b_a + \eta_a = M_a\overline{A^b} - b_a + \eta_a \tag{3.53}$$

and

$$E'_a = \left(W_a\Lambda_a + U_a\Delta_{v_a} + V_a\Delta_{u_a} - U_a\Delta_{v_a}\Lambda_a - V_a\Delta_{u_a}\Lambda_a\right)^T \tag{3.54}$$

where M_a and G_a, respectively, indicate the actual and nominal configurations of the sensors, $\Lambda_a$scale factor matrix of errors, W_a is the nominal direction matrix, V_a and U_a the orthogonal orientation vectors, b_a is the vector of bias, η_a is the measured noise.

The ideal acceleration vector may be represented as follows if it is assumed that the accelerometer was positioned at the distance from the center of the turntable.

$$\overline{A^b} = A^b + \overline{\omega_{ib}^b} \times \left(\overline{\omega_{ib}^b} \times d\right) + \dot{\omega}_{ib}^b \times d \tag{3.55}$$

where $\mathrm{A}^b = \begin{bmatrix} A_x^b & A_y^b & A_z^b \end{bmatrix}^T$ indicates the acceleration that would be taking place at the table's centre of rotation in relation to the body frame $\begin{bmatrix} \alpha_x^b & \alpha_y^b & \alpha_z^b \end{bmatrix}^T$ is a measure of the angular velocity of the turntable's acceleration, and d is defined as $\mathrm{d} = [d_x \quad d_y \quad d_z]^T$is the vector that is used to represent the lever arm.

Now, equation 3.56 is recast in a more succinct form as seen in the following:

$$\overline{A^b} = A^b - K_1\omega_2 - K_2\alpha^b \tag{3.56}$$

where

$$\boldsymbol{K}_1 \triangleq \begin{bmatrix} 0 & d_x & d_x & -d_y & -d_z & 0 \\ d_y & 0 & d_y & -d_x & 0 & -d_z \\ d_z & d_z & 0 & 0 & -d_x & -d_y \end{bmatrix},$$
$$\boldsymbol{K}_2 \triangleq \begin{bmatrix} 0 & -d_z & d_y \\ d_z & 0 & -d_x \\ -d_y & d_x & 0 \end{bmatrix},$$
$$\boldsymbol{\omega}_2 \triangleq \begin{bmatrix} \omega_x^{b^2} & \omega_y^{b^2} & \omega_z^{b^2} & \omega_x^b\omega_y^b & \omega_x^b\omega_z^b & \omega_y^b\omega_z^b \end{bmatrix}^T \quad (3.57)$$

If equation 3.57 substituted for equation 3.55, then the outputs of the accelerometer will be:

$$\tilde{A}^s = (G_a - E_a')A^b - K_w\omega_2 - K_a\alpha - b_a + \eta_a \quad (3.58)$$

in which:

$$\begin{aligned} &E_a' = \left(W_a\Lambda_a + U_a\Delta_{v_a} + V_a\Delta_{u_a} - U_a\Delta_{v_a}\Lambda_a\right) \\ &-V_a\Delta_{u_a}\Lambda_a^T \\ &K_w \triangleq (G_a - E_a')K_1 \\ &K_a \triangleq (G_a - E_a')K_2 \\ &M_a \triangleq G_a - E_a', G_a \triangleq W_a^T \end{aligned} \quad (3.59)$$

3.11.2. Transformed Unscented Kalman Filter TUKF Calibration Method

The sensor output is nonlinear. As a result, an estimation of the error parameters has to be carried out using a nonlinear filter. In contrast to the Unscented Kalman Filter UKF, the TUKF does not suffer from linearization error since the TUKF approach is founded on the sigma point. This allows the TUKF to perform more accurately. In addition, in contrast to other filters that are based on sigma points, such as the Unscented Kalman Filter, this filter does not need any tweaking UKF.

As a result, the TUKF was used in this investigation in the capacity of an estimator (observer). For TUKF to be able to execute the estimate of unknown parameters, it requires a dynamic model in addition to observations. All readings and process model of the calibrating filters will be provided in the sections that follow.

3.11.3. Model of Measurement and Process for the Accelerometer

For the purpose of representing measurement, which is contingent just on the output of the system of the accelerometer, the following equation is used:

$$z(k) = \tilde{A}^s - G_a A^b = -E'_a A^b - K_w \omega_2 - K_a \alpha - b_a + \eta_a \tag{3.60}$$

The Markovian model of the first order is a reasonable assumption for η_a, given that:

$$\eta_{a_i}(k) = C_{x_{ai}}(k) X_{a_i}(k) + v_{a_i}(k) \tag{3.61}$$

where X_{ai} stands for the first order Gauss-Markov process state variable, C_{xai} stands for the coefficient, and v_{ai} may be thought of as noise with white Gaussian distribution in addition to a mean of zero with a covariance labeled with $E\{v_{a_i} {v_{a_i}}^T\} = R_{a_i}$. If the calibration assumed that finished in a reasonably less period of time, then it will be possible to describe the error parameters as constant processes. This is because it will be assumed that the time it took to complete the calibration was relatively short. Because of this, it would seem that the error parameters are immune to the effects of variations in temperature. The dynamism of the process in the state space may be described as follows:

$$X_{aug_a}(k) = \overline{A_a}(k-1) X_{aug_a}(k-1) + \overline{B_a}(k-1) w_{x_a}(k-1) \tag{3.62}$$

where

$$X_{a_{aug_a}} = [x_a \quad {b_a}^T \quad {\lambda_a}^T \quad {\delta u_a}^T \quad {\delta v_a}^T \quad d^T \quad {A_a}^T B_a^T \, C_a^T]^T \tag{3.63}$$

the calculation for $\overline{\mathrm{A_a}}, \overline{\mathrm{B_a}}$an is as follows:

$$\overline{A_a} = \begin{bmatrix} A_a & 0 \\ * & I \end{bmatrix}, \overline{B_a} = \begin{bmatrix} B_a \\ 0 \end{bmatrix} \tag{3.64}$$

Moreover, there is an angular acceleration α indicated in the form of equation 3.64. In general, there are two different methods that may be used to calculate this signal. The first problem is associated with the twice differentiated output of the encoder. The existence of noise, on the other hand, causes this method to

result in an increase in the magnitude of the inaccuracy. Another potential strategy involves the angular acceleration of the system as an additional unknown variable in the state space. In order to accomplish this goal, a dynamic model for angular acceleration should be explored. For the purpose of this investigation, a Gauss–Markov dynamic of the first order was used to model angular acceleration. An angular acceleration is basically just a straightforward function of an angular velocity as in equation 3.65.

$$\begin{aligned} \alpha_i(k) &= a(k)\omega_i(k) - b(k)\omega_i(k-1) + w_{\alpha_i} \\ a(k) &= a(k-1) \\ b(k) &= b(k-1) \end{aligned} \tag{3.65}$$

where *a*, *b*, and *c* are constant coefficients that are estimated in the same way as any other coefficients. The process noise's covariance matrix is denoted by the equation:

$$E\{w_{\alpha_i} w_{\alpha_i}^T\} = Q_{\alpha_i} \tag{3.66}$$

The complete order of process dynamics is increased to 30, which are employed in the TUKF for the purpose of computing the overall error characteristics of accelerometers. This is carried out by including its angular acceleration equation 3.66, which brings the total up to 30.

3.11.4. Formulation of TUKF

A comprehensive description of TUKF is provided in [63]. Just its mechanism is described in this section, while the algorithm that governs it is given out in Table 3-3. Take into consideration a process model of the nth order, the measurement models for which would be as follows:

$$x_k = f(x_{k-1}, u_{k-1}) + \omega_{k-1} \tag{3.67}$$

$$y_k = h(x_k, u_k) + \sigma_k \tag{3.68}$$

where u represents the input and x_k represents the k_{th} sequence of state variables, the measurement Gaussian white noises process are ω in addition to σ, each f them has the values of covariance matrix Q_k and matrix R_k. The approach utilised to analyse the described process and evaluation dynamics is known as the TUKF approach. It comprises three key components, namely initialization, prediction, and measurement update. Both the sigma values, state variables ($\hat{x}_o^-$), and an covariance matrix error ($\hat{P}_o^-$) are all set to zero at the beginning. In order to make inferences about the future, the process model is used to compute estimates for state variables ($\hat{x}_k^-$), as well as the square root of the covariance matrix. The square root of the covariance matrix and the state variables ($\hat{x}_k^+$) are then updated based on the actual its model values and the measurement.

According to the information shown in table 3-3, E[.] designates the operator of the expected value, *qr*(.) stands for the QR factorization in linear algebra, *chol*(.) is regarded here as the decomposition process of the Cholesky factor, I_n is an matrix of the identity of the n-th order. The calibration procedure was carried out on an MPU6050 sensor in order to determine whether or not the approach described in this article is indeed practicable.

Table 3-3 The outline of Transformed Unscented Kalman Filter.

(1) Initializing	
Variables pertaining to the state and the square root (sr) of the error covariance matrix	$\hat{x}_0^+ = E[x_0]$ $P_0^+ = E\left[[x_0 - \hat{x}_0^-][x_0 - \hat{x}_0^-]^T\right]$ $S_0^+ = chol(P_0^+)$

Points for Sigma	$For\ i = 1,2,\dots,2n$ $\gamma_i = (\gamma_{i,1}, \gamma_i, 1, \dots, \gamma_{i,n})^T$ $\gamma_{i,2r-1} = \sqrt{\frac{2}{n}} cos\left(\frac{(2r-1)i\pi}{n}\right)$ $\gamma_{i,2r} = \sqrt{\frac{2}{n}} sin\left(\frac{(2r-1)i\pi}{n}\right)$ $r = 1,2,\dots,\left[\frac{n}{2}\right]$ $\gamma = [\gamma_1, \gamma_2, \dots, \gamma_{2n}], l = 2n$ $\mu_0 = \gamma\sqrt{n}[I_n, -I_n]$
(2) Prediction (Time Update)	
TUKF cubature points after transformation	$\chi_{k-1}^{+} = \boldsymbol{S}_{k-1}^{+}\boldsymbol{\mu}_0 + \hat{\boldsymbol{x}}_{k-1}^{+}$
Sample propagation points	For $i = 1,2,\dots,2n$ $\chi_{i,k}^{-} = \mathbf{f}(\chi_{i,k-1}^{+}, \mathbf{u}_{k-1})$
State prediction	$\hat{\mathbf{x}}_k^{-} = \frac{1}{l}\sum_{i=1}^{l} \chi_{i,k}^{-}$
SR-error covariance matrix prediction	$\chi_k^{-*} = \frac{1}{\sqrt{l}}(\chi_k^{-} - \hat{\mathbf{x}}_k^{-})$ $\mathbf{S}_k^{-} = qr([\chi_k^{-*}\text{chol}(\mathbf{Q}_k)])$
(3) Measurement Update	
TUKF predicted converted cubature points	$\chi_k^{+} = S_k^{-}\mu_0 + \hat{x}_k^{-}$
Sample propagation points	For $i = 1,2,\dots,2n$ $Z_{i,k}^{-} = h(\chi_{i,k}^{+}, u_k)$
Predicting measurement	$\hat{\mathbf{z}}_k^{-} = \frac{1}{l}\sum_{i=1}^{l} \mathbf{Z}_{i,k}^{-}$
Update of Sr-innovation covariance matrix	$Z_k^{-*} = \frac{1}{\sqrt{l}}(Z_k^{-} - \hat{z}_k^{-})$ $S_{z,k}^{-} = qr([Z_k^{-*}chol(R_k)])$

Update of cross-covariance matrix	$\chi_k^{+*} = \frac{1}{\sqrt{l}}(\chi_k^+ - \hat{x}_k^-)$ $P_{xz,k}^- = \chi_k^{+*}(Z_k^{-*})^T$
Updating the Kalman gain	$K_k = \left(P_{xz,k}^- / \left(S_{z,k}^-\right)^T\right) / S_{z,k}^-$
Updating the states	$\hat{x}_k^+ = \hat{x}_k^- + K_k(y_k - \hat{z}_k^-)$
Update Sr-error covariance matrix	$\underline{S}_k^+ = qr([\chi_k^{+*} - K_k Z_k^{-*} K_k chol(R_k)])$

IMU and Arduino both contributed to the data collection process. The inertial measurement unit (IMU) is comprised of three gyroscopes as well as accelerometers that are orthogonal to each other. It is situated within the turntable in a manner that facilitates consideration of the following matrices during configuration:

$$\boldsymbol{W} = \begin{bmatrix} 1 & 0 & 0 \\ 0 & 1 & 0 \\ 0 & 0 & 1 \end{bmatrix}, \boldsymbol{U} = \begin{bmatrix} 0 & 0 & 1 \\ 1 & 0 & 0 \\ 0 & 1 & 0 \end{bmatrix}, \boldsymbol{V} = \begin{bmatrix} 0 & 1 & 0 \\ 0 & 0 & 1 \\ 1 & 0 & 0 \end{bmatrix} \tag{3.69}$$

To assess the effectiveness for the proposed methodology, a comparative analysis was conducted between the outcomes derived from calibration utilising the Least Squares (LS) technique as well as those derived from calibration employing the proposed methodology.

3.11.5. Delaunay Triangulation Algorithm

This section examines how the Transmormed Unscented Kalman filter's output is impacted by the Delaunay triangulation process. With the help of this algorithm, the accuracy of the Kalman filter's output values can be improved as it cab seen in figure 3-17. A triangulation divides a polygon neatly into triangles, making it possible to, for example, quickly calculate the area or even a guarding of a polygon. Utilizing trigonometry (T) for interpolation is another popular application scenario: Consider an extending a function (f) "fairly" and continuously with (P), defined upon those vertices of the polygon (P°).

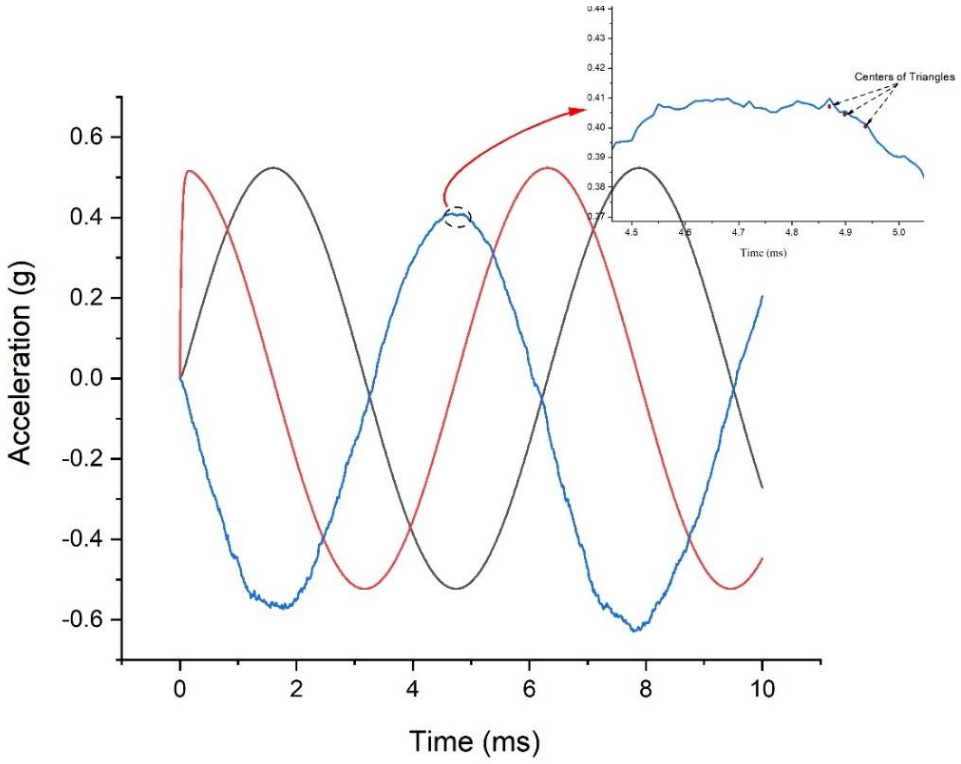

Figure 3-17 The Triangulation Process Result for TUKF Output

Afterward, locate the triangle (t) with a (T) which contains a point p ϵ (P˚). As (p) is a convex expression. With the vertices v_1, v_2, v_3 of t combined ($\sum_i^3 \lambda_i v_i$), the function values using the same coefficients ($f(p) = \sum_i^3 \lambda_i f(v_i)$) can simply interpolated. The procedure is to regard each of the three Kalman filter, output values as a triangle composed of three vertices, with one serving as the triangle's head and the other two as its base, if this is carried out, the center of the triangle- which will serve as such an alternative output value since it is closest to the real value as in figure 3-18.

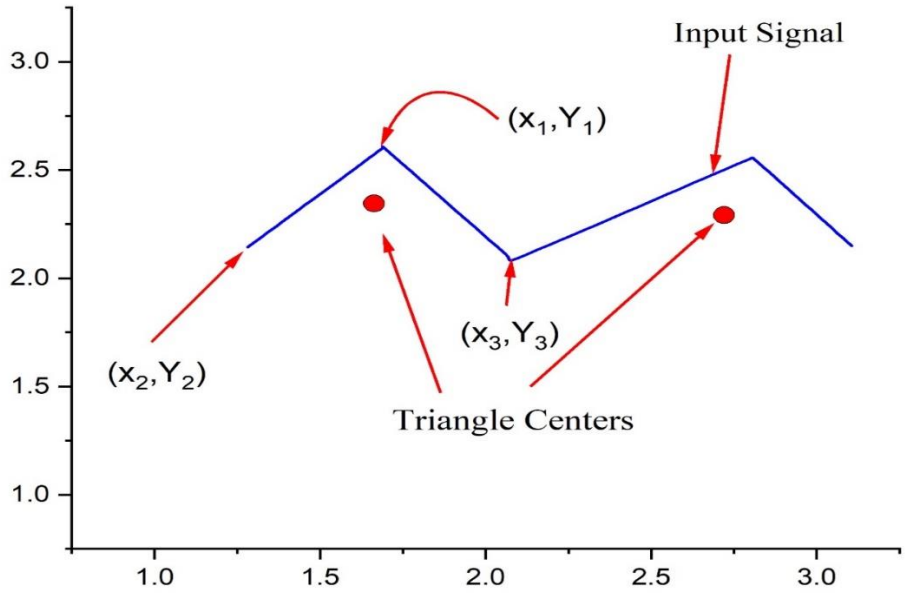

Figure 3-18 The Approximation Process for The TUKF Output Point

All steps are shown in figure 3-19, the flow chart summarize the calculated voltage must be applied after each self -test and stored in the lookup table for the next test and calibration.

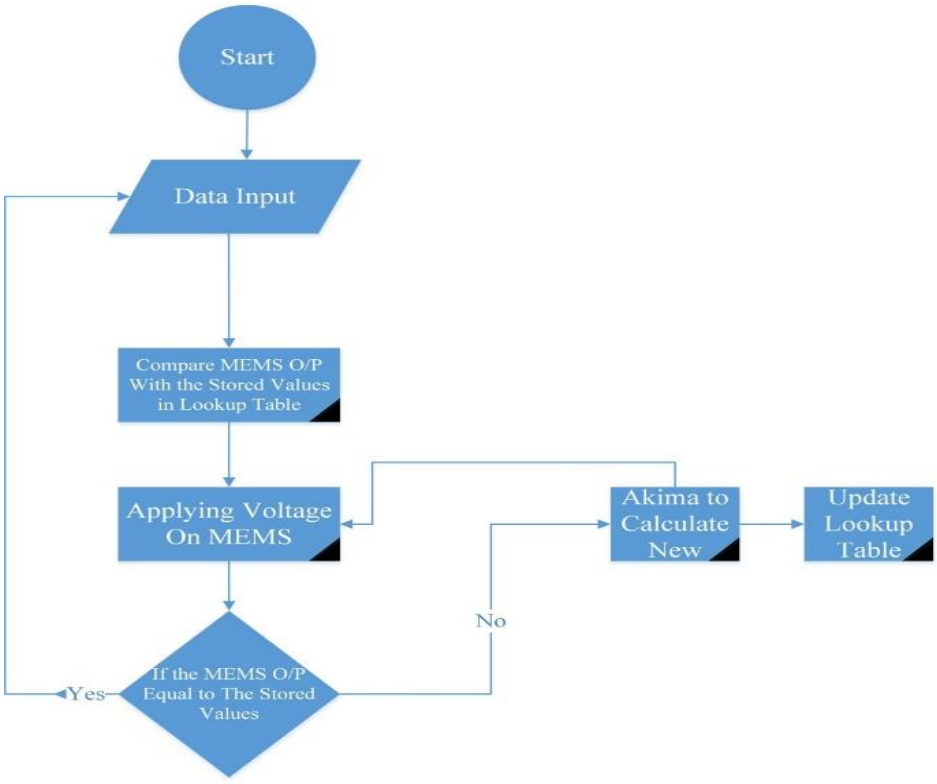

Figure 3-19 Flow Chart of The Akima Interpolation

3.12. Experiment setup

The setup of the experiment for practical reading from the MEMS sensor element MPU6050 is shown in the figure 3-20 and figure 3-21. The reading is taken using the arduino with serial data transmission of (115200 bps) for USB. The sensor is fixed on a working precision rotation plate to be rotated (0^o, 30^o, 50^o, 90^o). Each orientation will record the readings from the tree axis of the accelerometer. All the results for each step will be shown in chapter four.

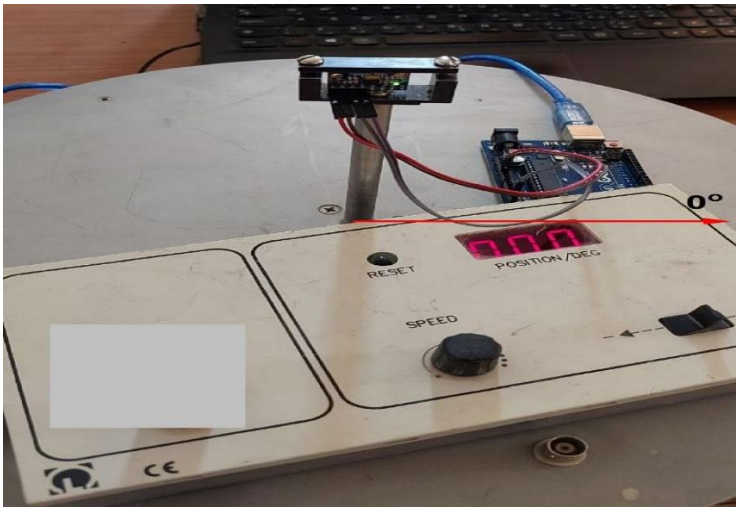

(a)

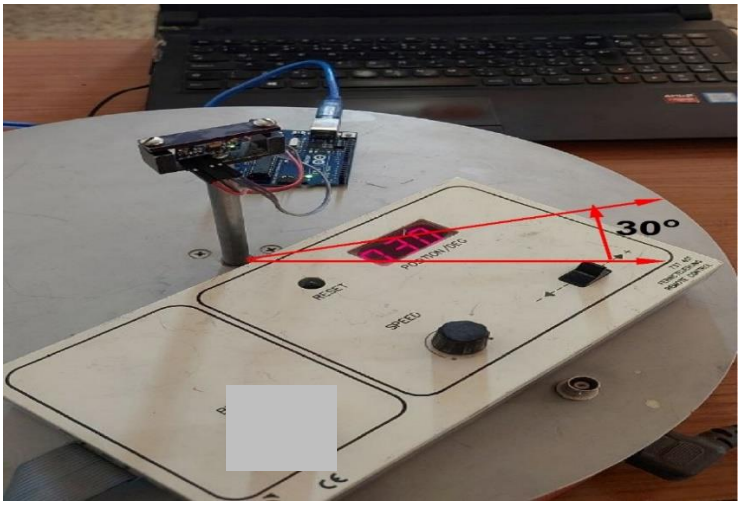

(b)

Figure 3-20 The Orientation of The Accelerometer (a) 0^o (b) 30^o

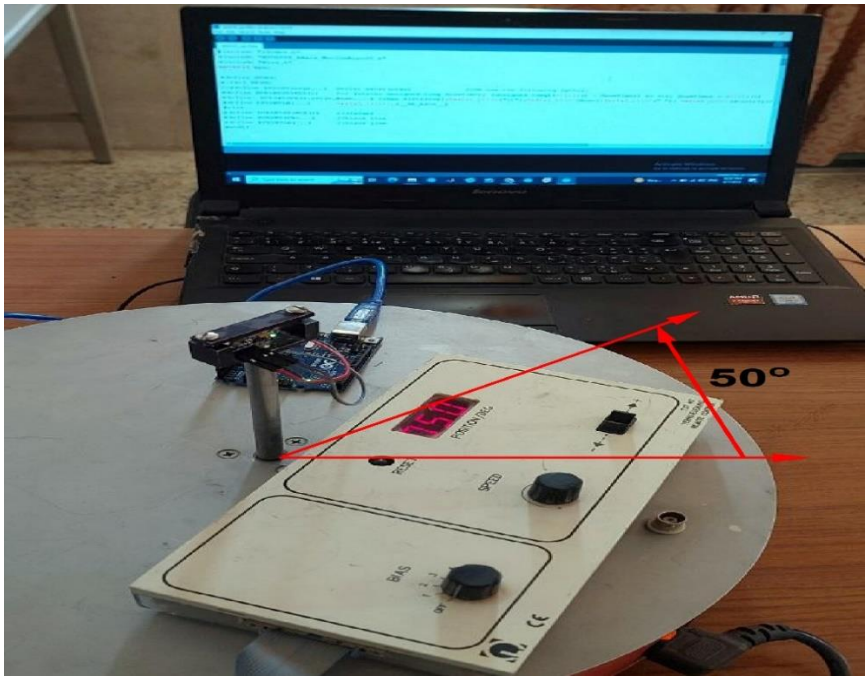

(a)

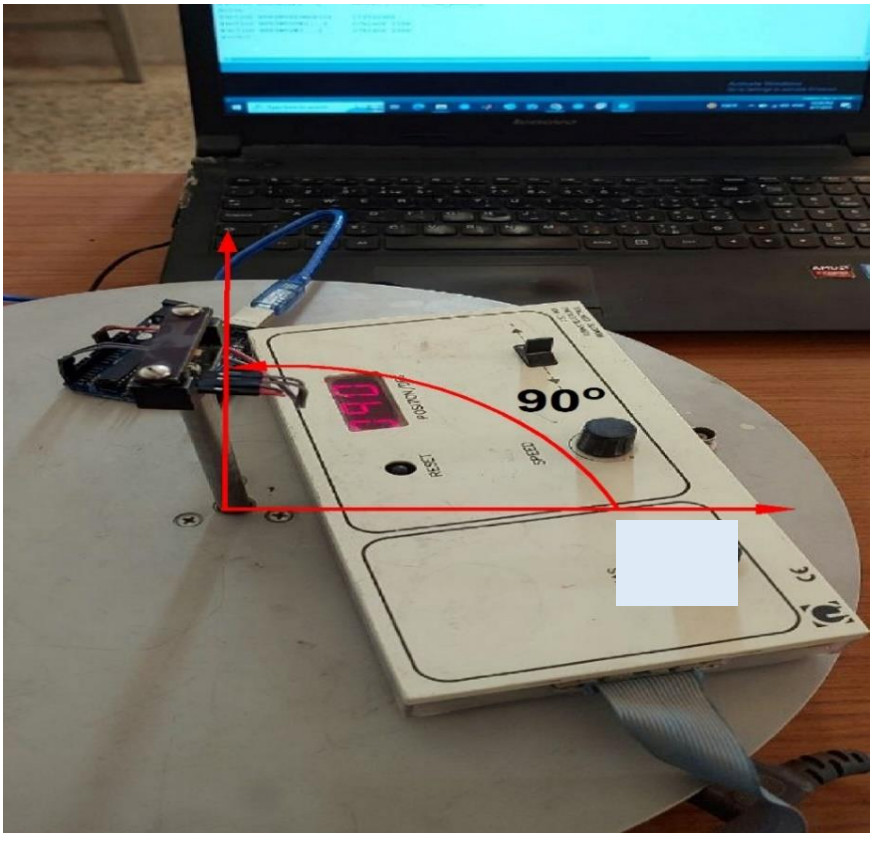

(b)

Figure 3-21 The Orientation of The Accelerometer (a) 50º (b) 90º

3.13. Chapter Summary

This chapter aimed to design three proposed self-test and calibration algorithms for MEMS and NEMS capacitive accelerometer in addition to the design of this accelerometer in micro and nano scale for three axes (X, Y, Z). A description has been given for the Genetic Algorithm (GA) to be used in the calculation of the compensation for the sensing element in the case of the sensing finger and spring fault to be stored in the lookup table. The first algorithm took the advantage of the Akima interpolation for the purpose of making the faulty output of the sensing element to be closed to the desired output calculated by GA and stored in the lookup table. The second method have employed the same Akima interpolation to be integrated with the Sigma-Delta modulator for a purpose of noise removing and resolution enhancement by oversampling. Several faults for the sensing fingers and spring were made to show the effectivity of the second method.

In the third algorithm, a transformed Kalman filter has been employed in addition to the Delaunay triangulation to be as a tracker for the three axes accelerometer. The bias and noise were well removed with good stability. Practical results were read using Arduino microcontroller from the MPU6050 accelerometer to show the effectiveness of this method.

CHAPTER FOUR

Experimental Results, Statistical Analysis and Discussion

Chapter Four: Experimental Results, Statistical Analysis and Discussion

4.1. Introduction

The simulation and implementation results in addition to the time response of the proposed algorithms that were explained in chapter three are presented in this chapter with the same order. Each of the proposed self-test and calibration method is implemented and tested via testing techniques presented in chapter three. GA algorithm is implemented with different cases to deeply evaluate the compensating voltage in the cases of the proposed fingers and spring fault, which is treated as BIST and stored in lookup table, to be applied on the testing fingers of the MEMS sensing element. In addition to GA implementation, Akima algorithm is applied for the calculation of the necessary voltage in the case of fault to be used as a calibration in the first and second method.

In the third method, the TUKF is used to take the advantage of the self-test and calibration of the three-axis MPU6050 accelerometer, then experimental readings are collected for two hours by the Arduino microcontroller for the purpose of calculating the Allan deviation to measure the bias instability and random walk compared to other related references.

4.2. Sensing Element Dimensions Calculation

A MATLAB program was developed using equations 3.4, 3.5, 3.6, and 3.7 that calculate and graph the width of such center plate as well as the length of each portion of the springs. The proof mass length is taken from the figure 4-1 in intersection point between the total sensing element width and the total magnitude of the spring attached to the sensing element. The x coordinate of the intersection is the proof mass length.

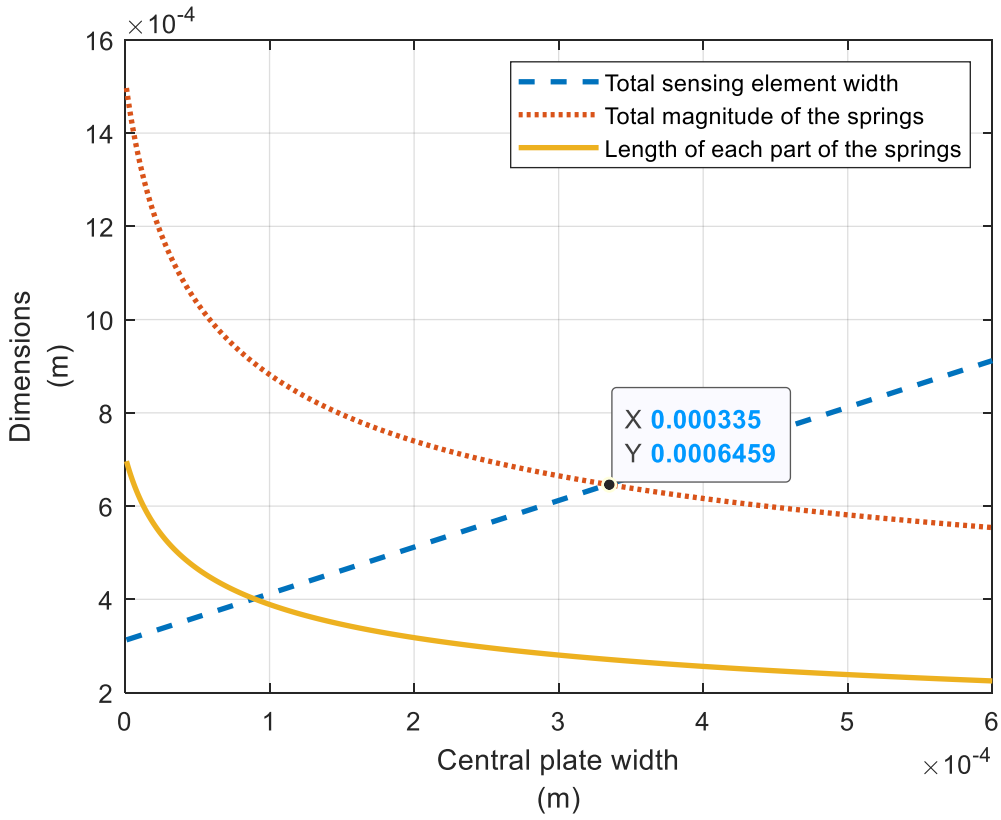

Figure 4-1 Central Plate Width Calculation

4.3. Method (1): Akima Interpolation

Fingers and spring fault simulation in COMSOL software, BIST calculation in GA and frequency response of the MEMS sensing element are presented in this section.

4.3.1. BIST Calculation Using GA

The number of possible faults related to fingers and spring which was introduced in chapter three (table 3-2) and its compensation values of the voltages (BIST) to be applied on the fingers of the proof mass are explained in table 4-1 be to be compared with the case of no fault (figure 4-2).

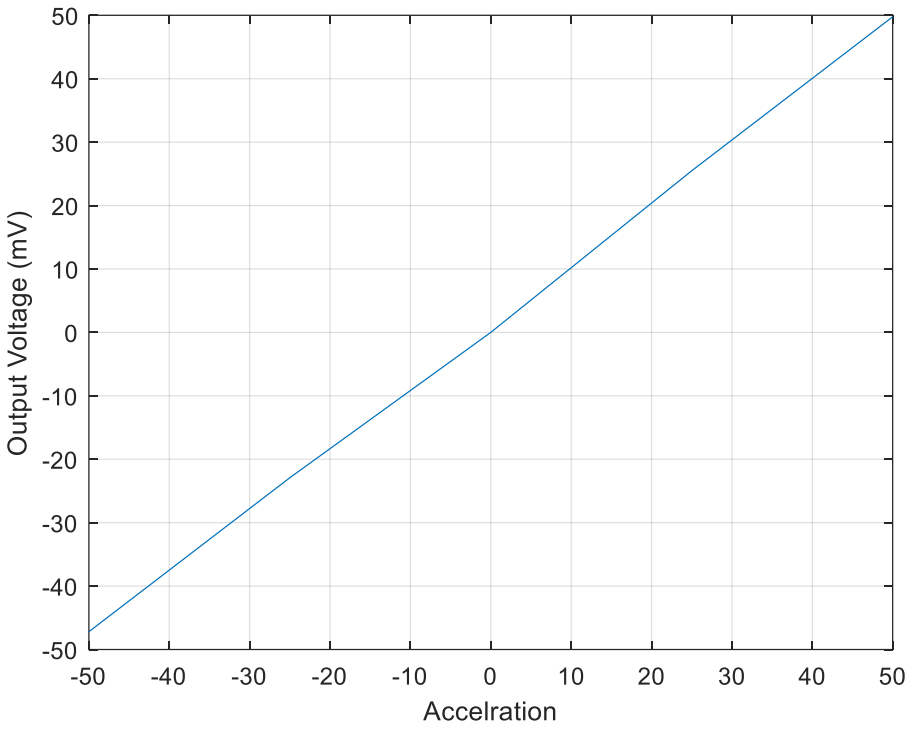

Figure 4-2 Sensing Element at No Fault Case

As can be seen in table 4-1, there are five cases of faults (1 finger to 5 fingers). Each finger fault resulted from the changing in its length and width which makes the sensing element output voltage differs from its designed voltage before the fault case. This drift will give bias at the output voltage and will be compensated by the Genetic Algorithm GA which produces the Built-In Self-Test (BIST) voltage value to be used in the interpolation and stored in the lookup table. The same procedure will be for the spring fault case, where the spring length and width can be changed for five cases as seen in the table. The spring property changes will affect on the proof mass displacement and then the output voltage of the sensing element. All these fault cases will be compensated by BIST voltage, and this voltage is applied on the self-test fingers for the self-test and fault compensation.

Table 4-1 Bias Values for The Fingers and Spring Faults

Finger Faults	1 Finger fault		2 Finger faults		3 Finger faults		4 Finger faults		5 Finger faults	
	Biased Value V		Biased Value V		Biased Value V		Biased Value V		Biased Value V	
	6.919775184		11.35735046		18.4679		20.18747585		24.57663725	
Spring Fault	Length of Spring	Width of Spring	Length of Spring	Width of Spring	Length of Spring	Width of Spring	Length of Spring	Width of Spring	Length of Spring	Width of Spring
	290 µm	3 µm	300 µm	3.5 µm	310 µm	4 µm	320 µm	4.5 µm	330 µm	5 µm
	Biased Value V		Biased Value V		Biased Value V		Biased Value V		Biased Value V	
	2.36414	2.11267	2.36358	2.34234	2.36304	2.34214	2.36262	2.4121	2.36244	1.93663

In figures 4-3 and 4-4, the effect of the finger and spring faults on the displacement of the proof mass is shown, where there is a bias in the zero-acceleration compared with the case of no fault (figure 4-1), all these values are listed in table 4-1. The fingers' fault can be defined as the change in its length and width or height, and this will affect the overall sensing element capacitance and thus the bias existence. Also, the change in length or width of the spring will result in the bias at the output.

As can be seen from figure 4-3, the 1 finger fault (figure 4-3(a)) will result in less bias while this bias will increase for 2,3 and 4 fingers (figure 4-3(b,c,d)) as compared with the case that there should be no output (0 V) and that the output should be zero at the no acceleration point (0 g). In figure 4-4, in the case of the spring fault, the same meaning is shown, where the bias value increased as the fault has increased. The fault of the spring has the more effect in comparison with the fingers fault, because the spring effect is on the proof mass movement.

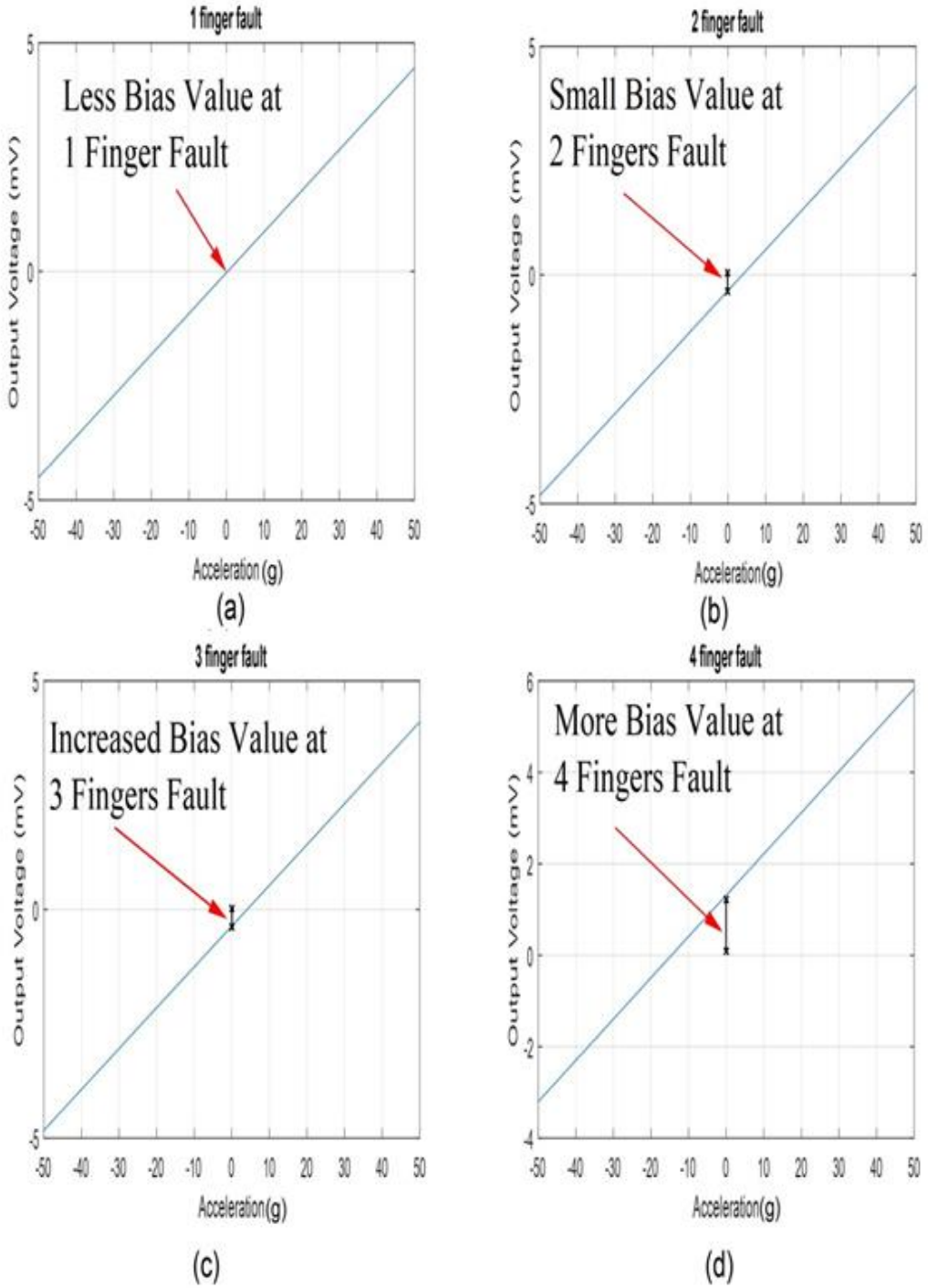

Figure 4-3 The Effect of Sensing Fingers Fault on the Output Voltage at Different Cases

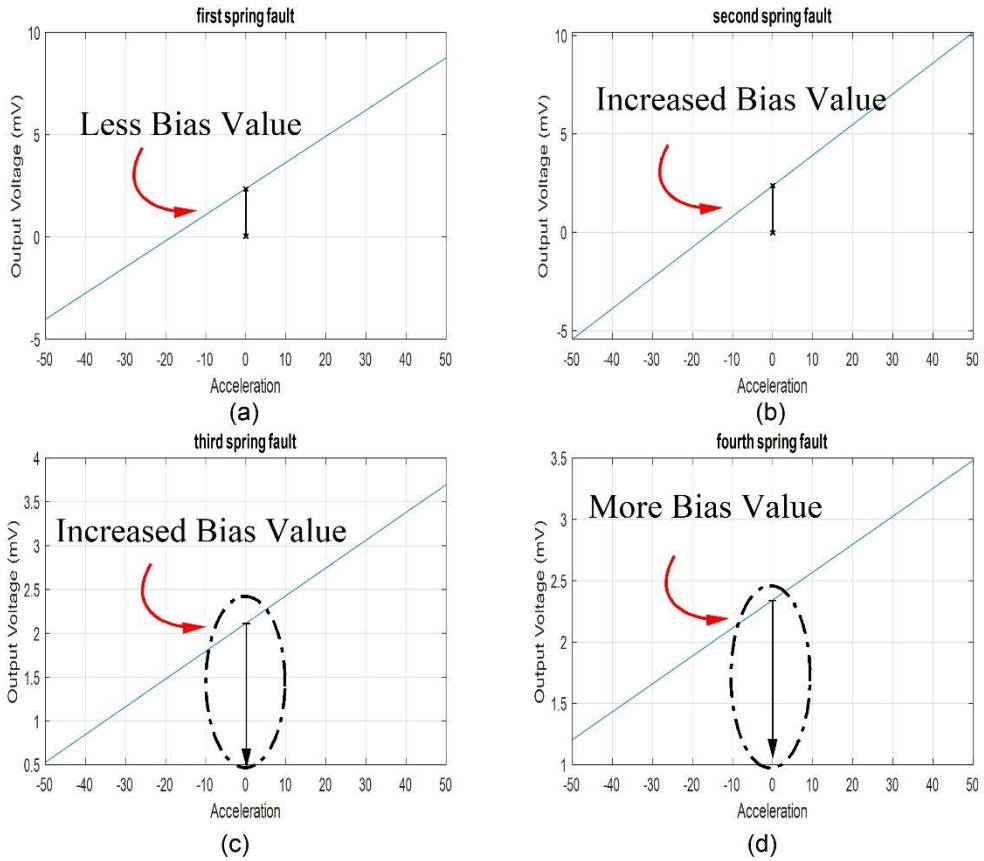

Figure 4-4 The Effect of Spring Fault on the Output Voltage at Different Cases

Therefore, after the implementation of the Akima interpolation process, there will be a reduction in all these bias values compared with the case of no fault as seen in figure 4-1 which means that an acceptable calibration was achieved. The lookup table was fed with the desired referenced outputs (calculated by GA) of the sensing element MEMS, then the sensing element outputs is treated as inputs and will be sued to calculate the expected bias voltage to return the device to its normal position before fault. As a result of compensating the error (spring and fingers fault), the obtained results are in well compatible with the exact solution as shown in figures 4-5 and 4-6.

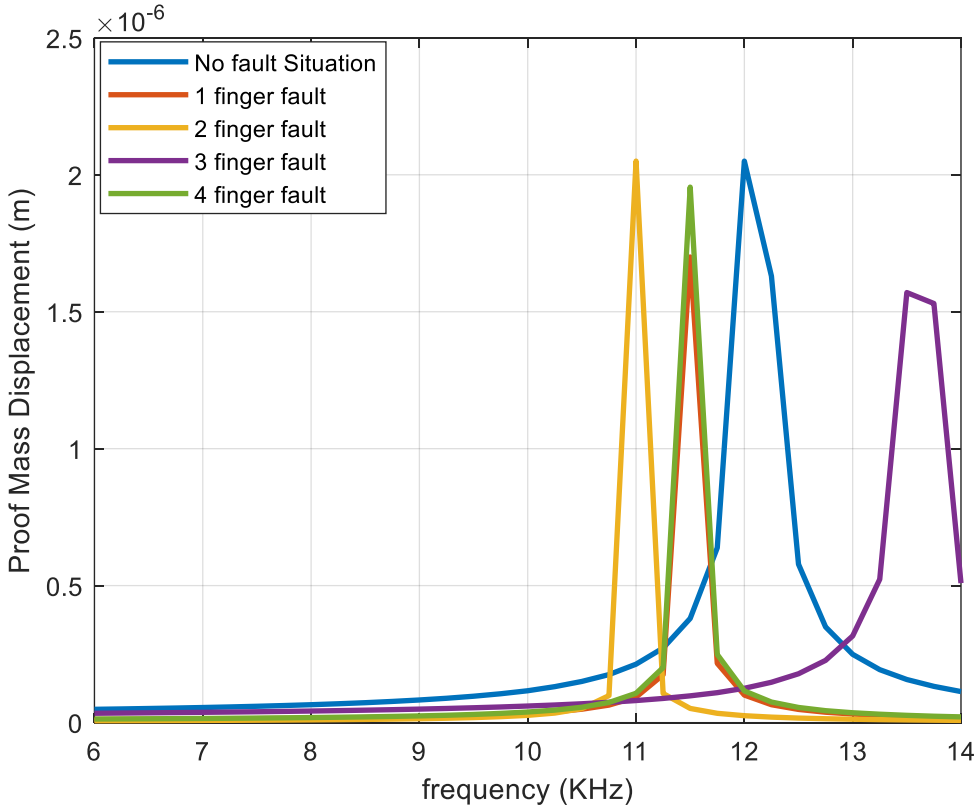

Figure 4-5 Sensing Element Resonance Frequency Response Before Calibration Case

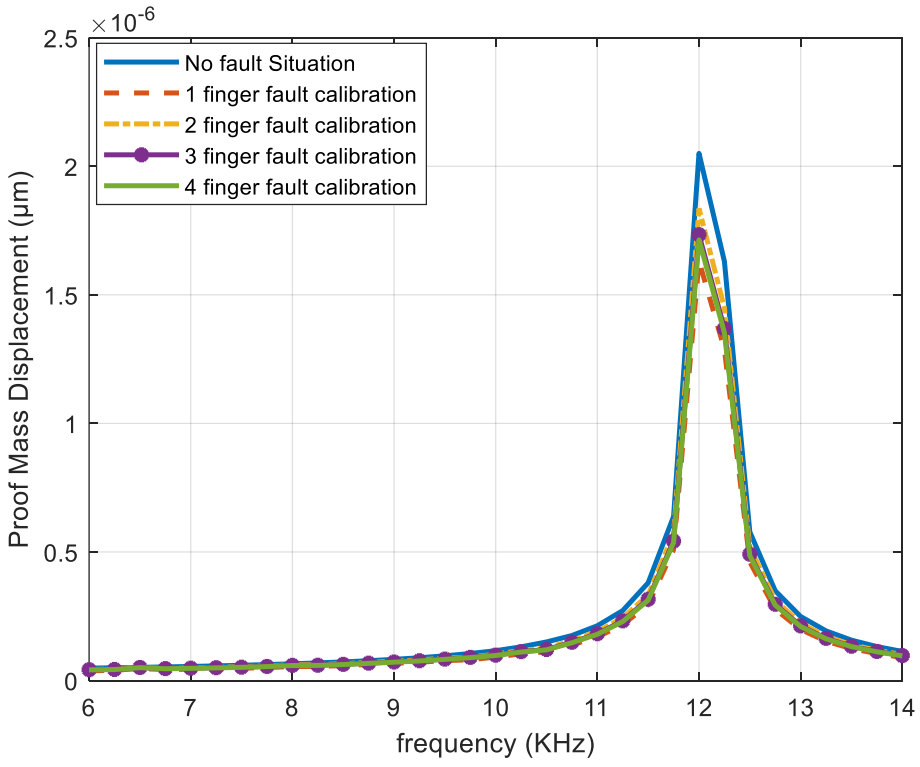

Figure 4-6 Sensing Element Resonance Frequency Response at Calibration Case

The frequency responses of faulty cases 1,2 and 3 in figure 4-5 (yellow, red, purple) show that the sensing element resonance frequency is shifted because of the changes in the overall capacitance of the proof mass as a result of the proof mass structure deformation because of the device aging and temperature effect. This change in the structure of the device will lead the resonance frequency to be different from the designed value. Therefore, the calibration process is needed to reposition of the proof mass to its zero point when there is no acceleration (reducing the bias value). The result given for the calibration case is shown in figure 4-6, where the faulty frequency responses cases (yellow, red, purple) are coincided with the blue on (no faulty case).

Table 4-2 shows the calculated BIST values by Genetic Algorithm (GA) for 1,2,3,4 and 5 fingers in addition to the spring faults that to be applied on the self-test fingers to minimize the bias values. This BIST calculation is carried out by converting the COMSOL sensing element design to MATLAB environment and then applying GA.

Table 4-2 BIST Values Using GA to Minimize the Bias Values

Finger Faults	1 Finger fault	2 Finger faults	3 Finger faults	4 Finger faults	5 Finger faults
	BIST by GA	BIST by GA	BIST by GA	BIST by GA	BIST by GA
	2.4 V	2.45 V	2.56 V	2.7 V	2.87 V
Spring Fault	BIST by GA	BIST by GA	BIST by GA	BIST by GA	BIST by GA
	1.93 V	1.96V	1.99 V	2.1 V	2.2 V

Table 4-3 illustrates the minimization of bias values in the case of 1,2,3,4, and 5 fingers in addition to the spring fault cases after applying the Akima interpolation. It is noticed that the bias value is more reduced than by the algorithm used which means the best calibration case for the proof mass.

Table 4-3 Bias Values Minimization After Akima interpolation

Finger Faults	1 Finger fault		2 Finger faults		3 Finger faults		4 Finger faults		5 Finger faults	
	Biased Value V		Biased Value V		Biased Value V		Biased Value V		Biased Value V	
	0.01		0.026		0.04		0.054		0.087	
Spring Fault	Length of Spring	Width of Spring	Length of Spring	Width of Spring	Length of Spring	Width of Spring	Length of Spring	Width of Spring	Length of Spring	Width of Spring
	290 µm	3 µm	300 µm	3.5 µm	310 µm	4 µm	320 µm	4.5 µm	330 µm	5 µm
	Biased Value V		Biased Value V		Biased Value V		Biased Value V		Biased Value V	
	0.026	0.052	0.034	0.088	0.0303	0.021	0.015	0.068	0.037	0.041

4.4. Method (2): Sigma-Delta Modulation

In this section, the noise shaping by using the Sigma-Delta Modulator technique is utilized to see its effect on noise removing from the sensing element input signal. The calculation of the Power Spectral Density (PSD) before and after calibration using the Akima interpolation, time response of the quantized input and output signal were all calculated in this method.

4.4.1. Noise removing

The noise coming from the sensing element such Brownian noise and the one resultant from the quantization process can be reduced by oversampling or increasing the quantization levels throw increasing the encoding bits as in figures 4-7 to 4-10. When the value of the encoding bits (D) is increased from 8 to 12, it was able to raise the number of quantization levels in the full-scale voltage from 256 to 4096. This was accomplished by increasing the number of bits utilized to quantize the signal. This provided the quantization more accuracy as described in the first portion of this explanation. The upper and lower bounds of the quantization error percentage have been lowered to (-DELTA/2) and (+DELTA/2) respectively (DELTA = V_fullscale/4096). This percentage brought the Signal to Quantization Noise Ratio (SQNR) up greatly while also

lowering the strength of the quantization noise. This may be noticed by looking at the spectrum. A spectrum with minimal noise would have spikes that are lower in percentage over the whole frequency range.

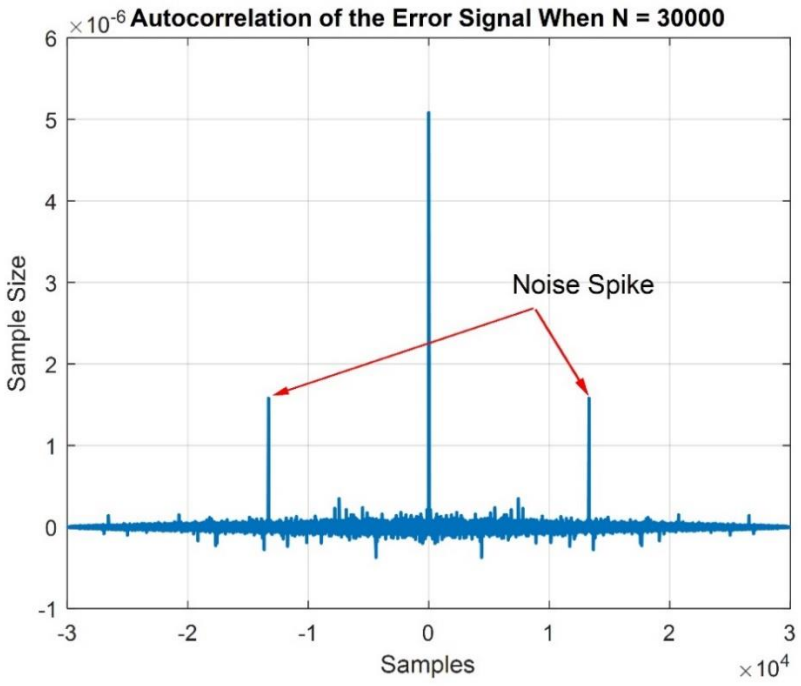

Figure 4-7 Autocorrelation of the Error Signal When D=8

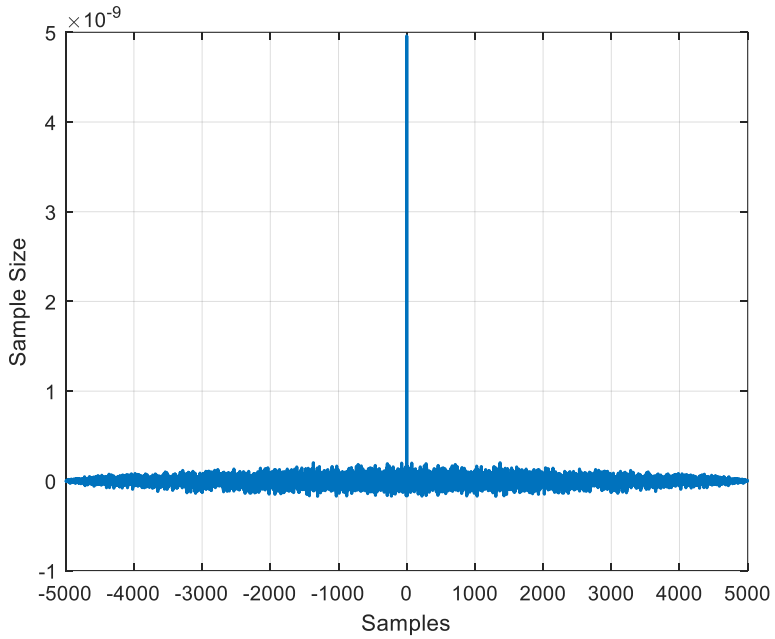

Figure 4-8 Autocorrelation of the Error Signal When D=12

The difference between figure 4-7 and 4-8 is the existence of the noise harmonic. As the number of the encoding bits is increased from 8 to 12 bits, the noise harmonic is greatly lowered which gives a minimal noise level at the output then purer signal.

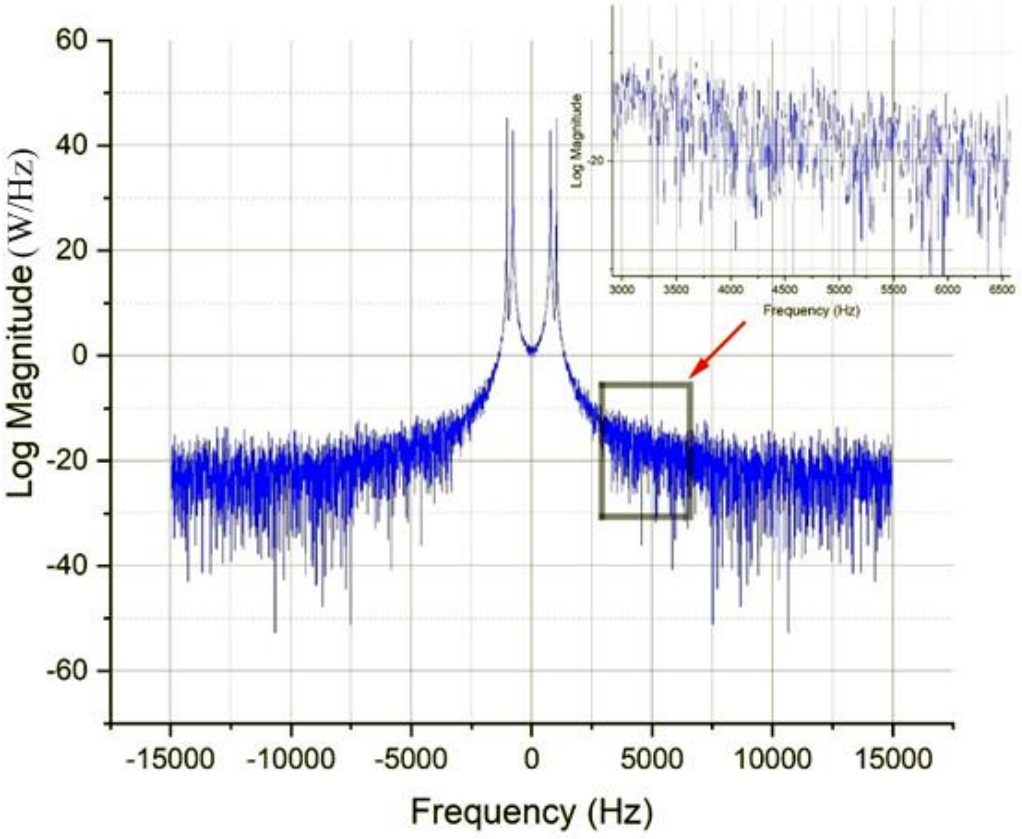

Figure 4-9 Frequency Response of the Quantized Output D = 8

The Power Spectral Density (PSD) of the signal at the encoding (D) of 8 bits is shown in figure 4-9, which shows that the noise has more harmonics than the power spectral density shown in figure 4-10 at (D) of 12 bits which shows low noise level and this makes the distribution looks more uniform.

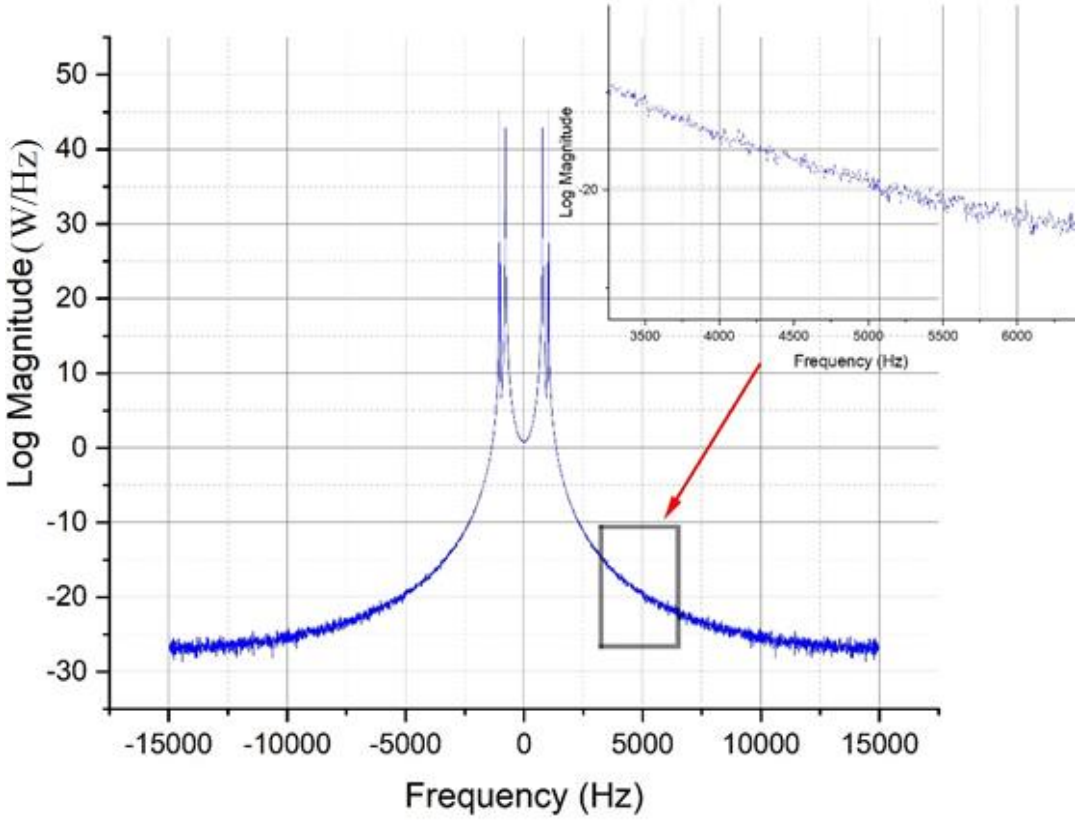

Figure 4-10 Frequency Response of the Quantized Output D = 12,

In case of the system with no noise shaping the noise, the transfer function is given by $1/(1-a_p(z^{-1}))$, where (a_p) is the pole value. When the frequency transform will be ($z = e^{jw}$) which is found that the noise transfer function has higher values at lower frequencies than at higher frequencies. This produces the higher noise at lower frequencies.

Table 4-4 shows the quantization signal to noise ratio versus the number of encoding bits (D) and pole value (a_p) before noise shaping and table 4-5 after noise shaping. The reason why theoretical power is less than the one that was calculated because MATLAB also quantizes the values which it is called infinite precision (64 bit in this case) but it is actually not.

Table 4-4 The Values of Signal to Noise Ratio Versus Number of Bits and Pole Value Before Noise Shaping.

Ideal Signal to Noise ratio	Quantization Signal to Noise ratio	Theoretical Signal to Noise ratio
D = 8, a = 0.6	D = 8, a = 0.6	D = 8, a = 0.6
37.5324	37.5332	38.4026
D = 12, a = 0.6	D = 12, a = 0.6	D = 12, a = 0.6
61.5851	61.5849	62.4850

Table 4-5 The Values of Signal to Noise Ratio Versus Number of Bits and Pole Value After Noise Shaping.

Ideal Signal to Noise ratio	Quantization Signal to Noise ratio	Theoretical Signal to Noise ratio
D = 8, a = 0.6	D = 8, a = 0.6	D = 8, a = 0.6
36.8612	36.8621	38.4026
D = 12, a = 0.6	D = 12, a = 0.6	D = 12, a = 0.6
60.5851	60.5838	61.4840

4.4.2. Fault and Calibration Process

To determine the optimal voltage for the self-test electrode to restore the sensing element to its original position after a fault, the lookup table was initially populated with the desired reference responses of the sensing device, specifically the spring and fingers in a fault-free scenario. The spectrum of the Sigma-Delta (ΣΔ) accelerometer's performance is presented in Figure 4-11, showcasing the impact of calibration on various finger and spring defects. The results indicate successful correction of these issues. Following each computation, Akima records the calculated voltage into the searching table (lookup table) to be one of the saved inputs for the subsequent self-test and calibration process.

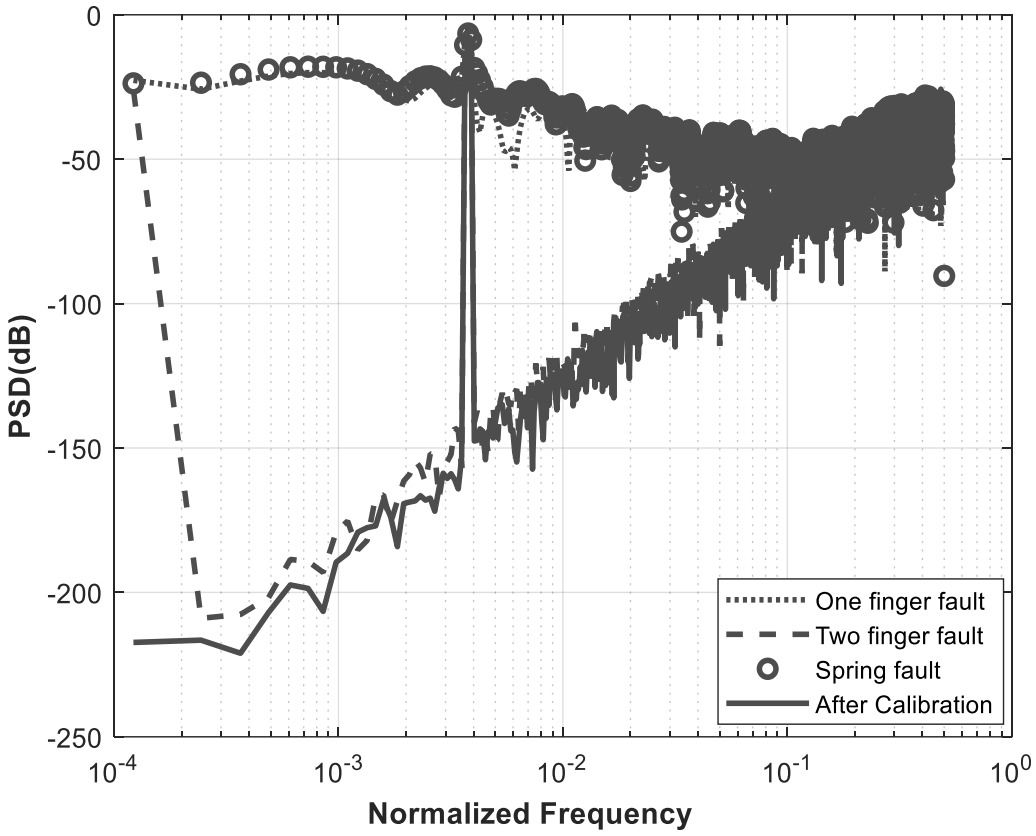

Figure 4-11 The Spectrum Output of The Sigma-Delta (ΣΔ) Accelerometer for various Finger and Spring Faults

4.5. Method (3): Kalman Filter

Figure 4-12 displays the errors of the Transformation Unscented Kalman Filter (TUKF) with Maximum Likelihood (ML) for the calibrated accelerometer signals in a single direction. This data was obtained during the validation process.

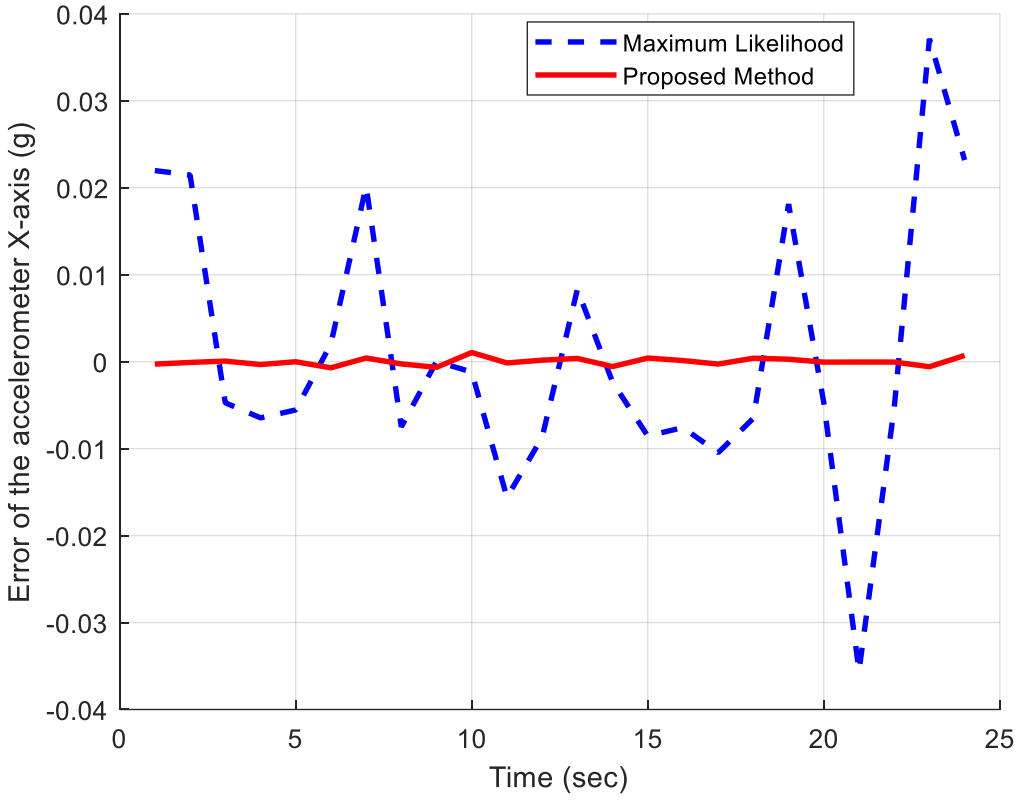

Figure 4-12 The Margin of Error for The Linear Acceleration That Was Experimentally Calibrated in One Direction

The Allan variance approach is used to ascertain the properties that are underlying random processes which are accountable for the generation of the data noise. For describing the methodology and evaluating the Velocity Random Walk (VRW), Bias Stability, and Angle Random Walk (ARW), suppose that there are N successive data points, and each of them has a sampling time of t_o. Each of the n successive data points (with $n<N/2$) that comes together to form a group is considered to be a cluster, as seen in figure 4-13.

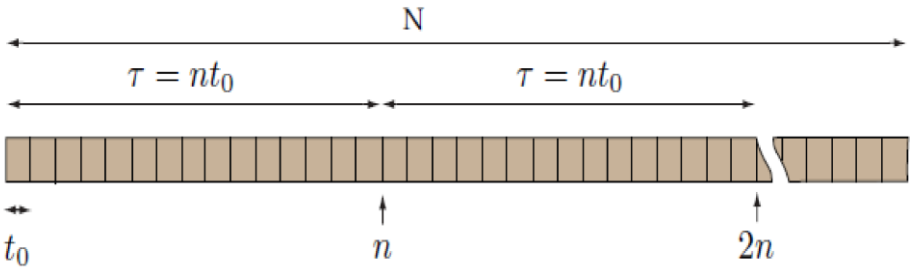

Figure 4-13 Diagram of Data Structure That is Used in The Allan Variance Algorithm

Figure 4-14 shows the Allan deviation before applying TUKF algorithm which gives the value of bias stability of (135.7 µg), and the random walk acceleration of (86.848 µg). Table 4-6 display the 50,000 data points recorded over the 2 hours, each representing a single axis of sensor data for the X, Y, and Z axes.

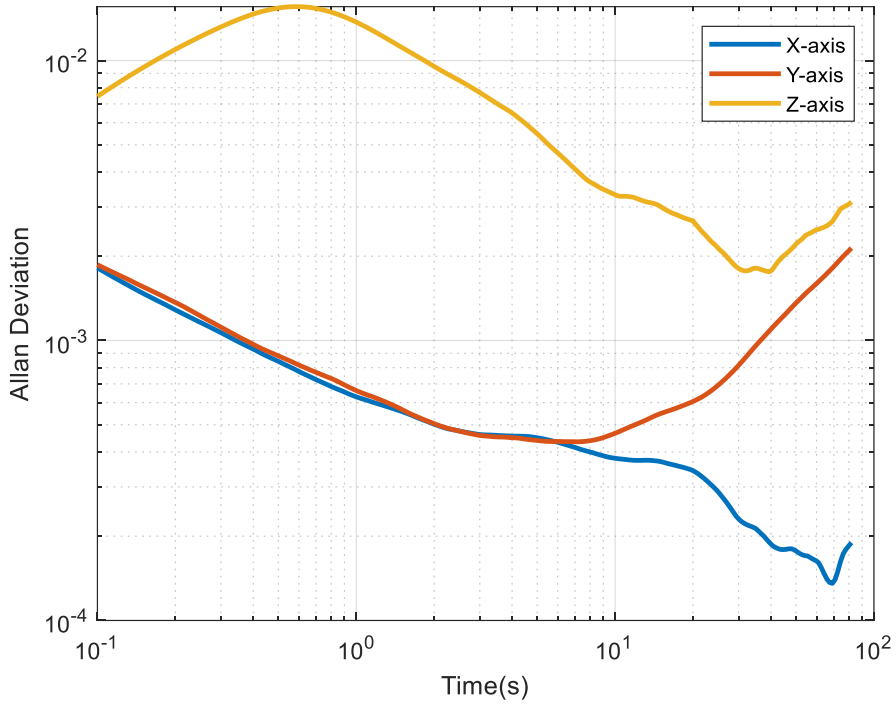

Figure 4-14 Allan deviation before applying TUKF algorithm

Table 4-6 The Collected Data From MPU6050 Sensor Before TUKF Algorithm

Time	X data (m/s^2)	Y data (m/s^2)	Z data (m/s^2)
11:30:50	0.057	-0.134	9.73
11:30:50	0.077	-0.115	9.778
11:30:50	0.077	-0.144	9.768
11:30:50	0.067	-0.134	9.74
11:30:51	0.086	-0.134	9.759
11:30:51	0.057	-0.134	9.778
11:30:51	0.057	-0.144	9.749
11:30:51	0.057	-0.144	9.74
11:30:52	0.057	-0.134	9.778
11:30:52	0.057	-0.134	9.759
11:30:52	0.057	-0.134	9.749

Figure 4-15 shows the setup for the data reading from the MPU6050 that was aged by putting it in the oven chamber at temperatures (-15^o C to 80^o C). 50,000 points of data then recorded after that within 2 hours as shown in table 4-7, where a piece of data collected from the sensor for X, Y and Z axes at a specific time in seconds and temperatures.

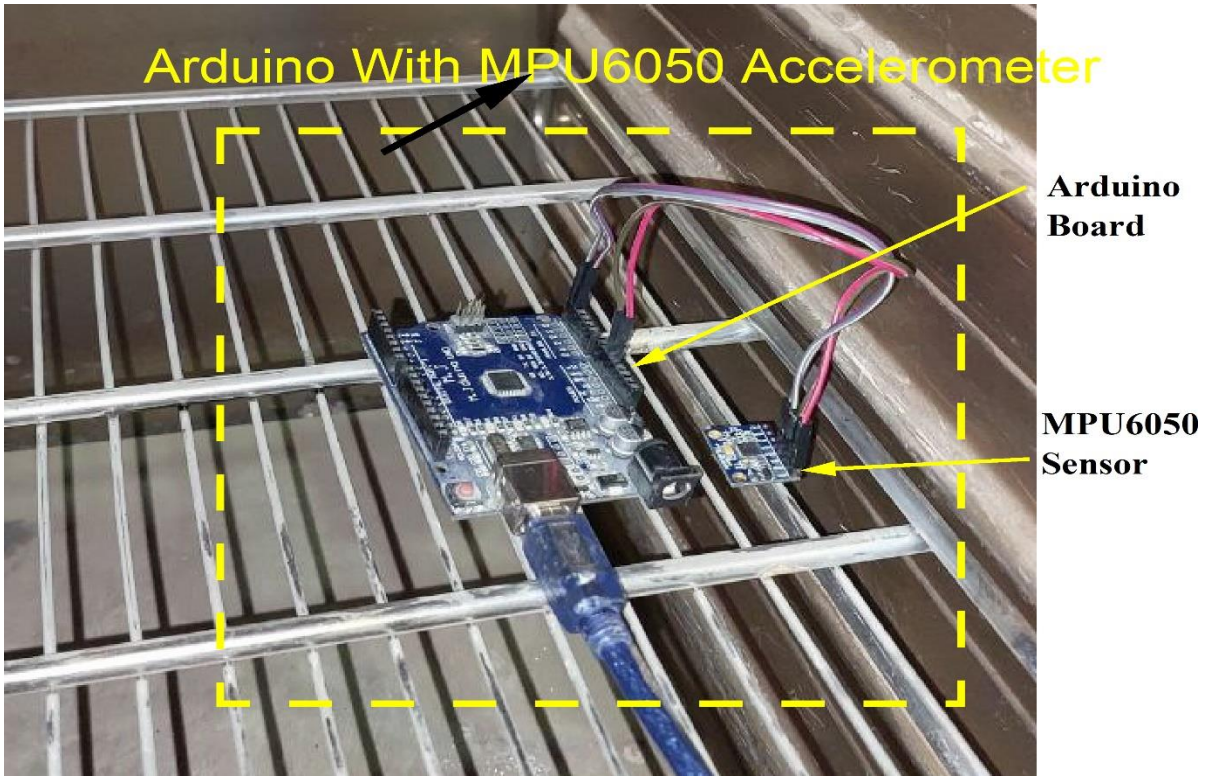

(a)

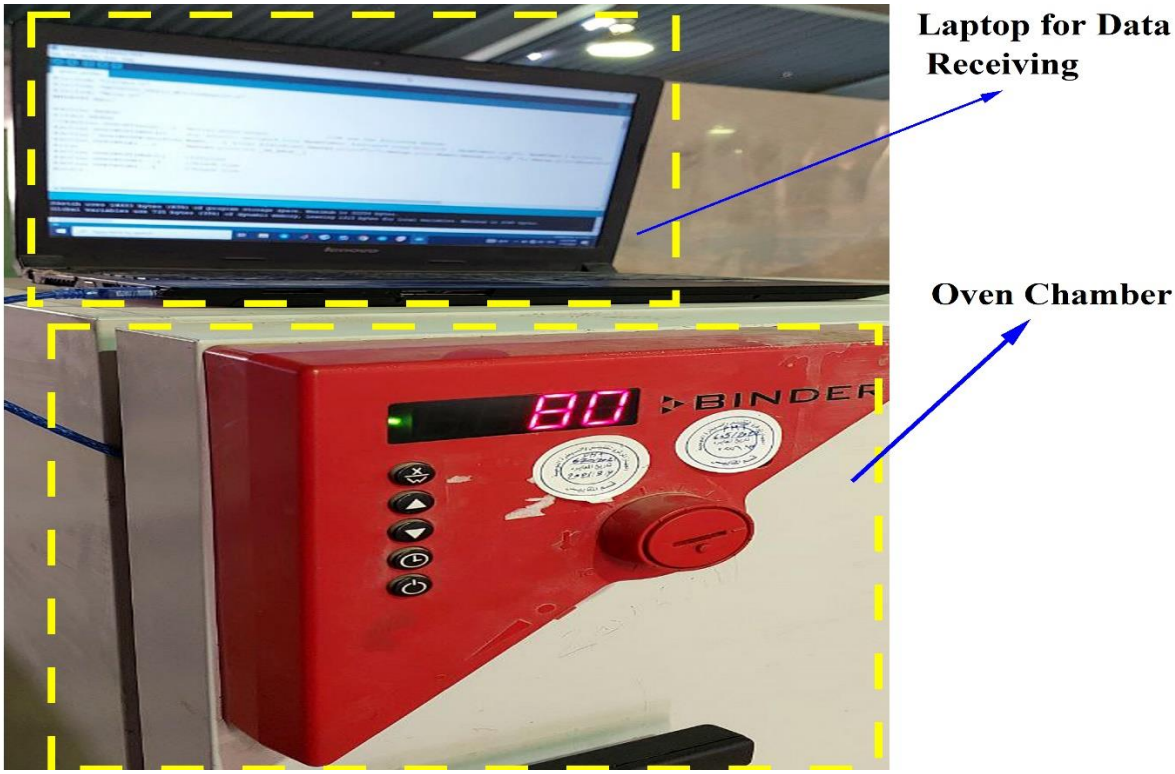

(b)

Figure 4-15 Photographs of the experiment setup (a) Inside The Chamber (b) Data Collecting by The Laptop

Table 4-7 The Collected Data From MPU6050 Sensor After TUKF Algorithm

Time	Temperature C	X data (m/s^2)	Y data (m/s^2)	Z data (m/s^2)
15:10:13	0^o	0	0.0067	9.75959
15:10:13	0^o	0	0.0067	9.75959
15:10:13	0^o	0	0.0067	9.75959
15:10:13	0^o	0	0.0067	9.75959
15:10:14	0^o	0	0.0067	9.75959
15:10:14	0^o	0	0.0067	9.75968
15:10:14	0^o	0	0.0067	9.75959
15:10:14	0^o	0	0.067	9.75959
15:10:14	0^o	0	0.0067	9.75959
15:10:15	0^o	0	0.0067	9.75959
15:10:15	0^o	0	0.0067	9.75959
Time	Temperature C	X data	Y data	Z data
17:10:16	30^o	0	0.0067	9.75959
17:10:16	30^o	0	0.0067	9.75959
17:10:16	30^o	0	0.0067	9.75959
17:10:16	30^o	0	0.0067	9.75959
17:10:16	30^o	0	0.0067	9.75959
17:10:17	30^o	0	0.0067	9.75959

17:10:17	30º	0	0.0067	9.75959
17:10:17	30º	0	0.0067	9.75959
17:10:17	30º	0	0.0067	9.75959
17:10:17	30º	0	0.0067	9.75959
Time	Temperature C	X data	Y data	Z data
18:10:20	60º	0.001	0.00672	9.75958
18:10: 20	60º	0.001	0.00672	9.75958
18:10: 20	60º	0.001	0.00672	9.75957
18:10: 20	60º	0.001	0.00673	9.75957
18:10:21	60º	0.001	0.00672	9.75958
18:10:21	60º	0.001	0.0673	9.75955
18:10:21	60º	0.001	0.00672	9.75956
18:10:21	60º	0.001	0.00671	9.75958
18:10:22	60º	0.001	0.00672	9.75959
18:10:22	60º	0.001	0.00671	9.75959
Time	Temperature C	X data	Y data	Z data
20:10:11	80º	0.003	0.00672	9.75968
20:10:11	80º	0.0012	0.00672	9.75978
20:10:11	80º	0.0013	0.00674	9.75958
20:10:11	80º	0.0014	0.00683	9.75959

20:10:12	80^{o}	0.002	0.00682	9.75957
20:10:12	80^{o}	0.0015	0.0673	9.75957
20:10:12	80^{o}	0.0016	0.00675	9.75976
20:10:12	80^{o}	0.0023	0.00661	9.75956
20:10:13	80^{o}	0.0011	0.00682	9.75956
20:10:13	80^{o}	0.0015	0.00678	9.75975

4.5.1. Comparison With Previous Works

In this section, a comparison with other related works has been presented. In [27], theoretical basis is the chi-square square distribution of the Mahalanobis distance, and the purpose of this approach is to enhance the effectiveness and resilience of a filter by employing a dual state model.

The authors of [22] have presented a nonlinear model and employ a calibration technique based on the Transformation Unscented Kalman Filter (TUKF) to estimate the parameters of a sensor model for a three-axis gyroscope along with an accelerometer.

The authors of [20] have presented an innovative adaptive and robust Kalman filter known as the Modified Sage Husa Adaptive Robust Kalman Filter (MSHARKF). Following each iteration of the MSHARKF algorithm, the state of the Adaptive Robust Kalman Filter (ARKF) method undergoes an update, accompanied by the introduction of a novel adaptive scale factor to the ARKF algorithm.

To consider the effectiveness of our proposed methods and as illustrated in table 4-8, the bias instability has been improved compared with the previous

works [64], [65], [66], [67], [27], [22] and [20], [32] for three axes, which shows a very competitive outcome for the performances of bias stability and Acceleration Random Walk in the temperature range (-15^{o} C to 80^{o} C) which is obtained in this work. Three measurements from the IMU, while the sensor was kept still in a fixed orientation. The calculated Allan deviation for the accelerometer's three axes is displayed in figure 4-16. As it can be seen, the readings from each of the three axes are stable over time compared to the readings in table 4-7.

Table 4-8 Comparison Between The Present Work and The Previous Works

References	Acceleration Random Walk μg/√Hz	Bias Stability μg
[27]	80	40
[22]	-	250
[20]	1000	290
[64]	0.7	0.123
[65]	70	100
[66]	6.1	2.8
[67]	79.15	36
[32]	-	2
Present Work	0.71	0.116

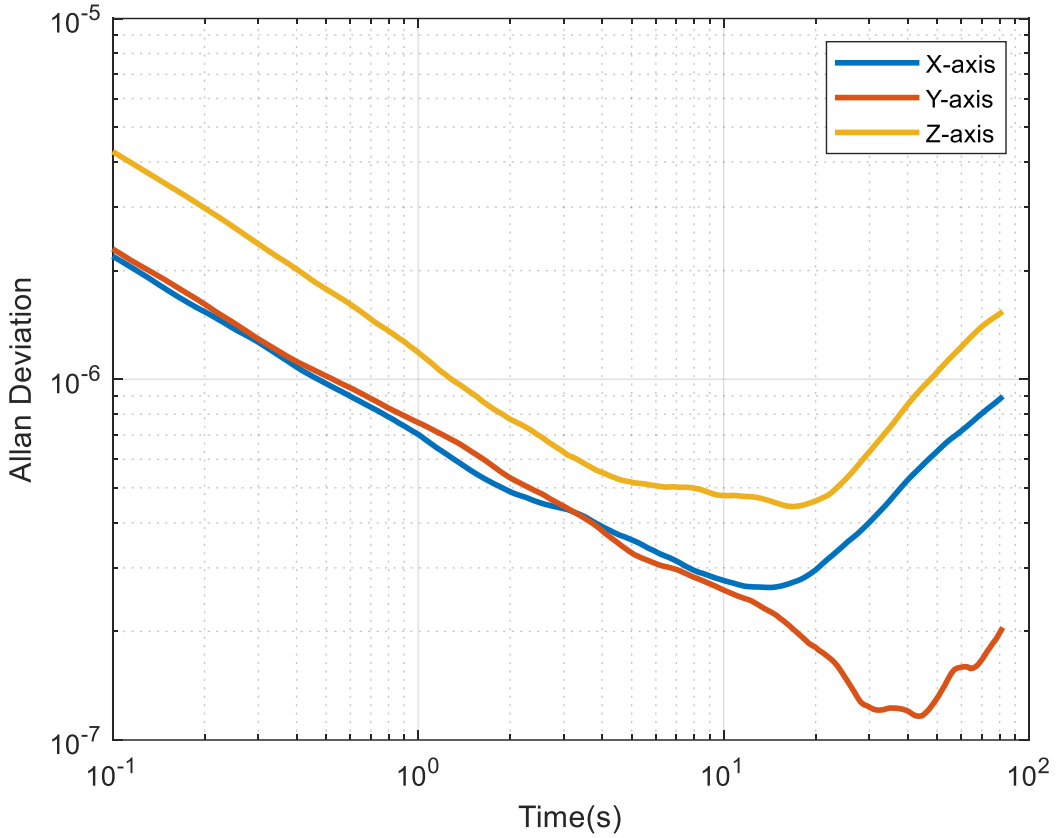

Figure 4-16 Allan deviation after the (TUKF) and the Delaunay Triangulation of the 3-axis (X,Y,Z)

This TUKF with triangulation method, utilized in this work, investigated the calibration of such as the Microelectromechanical IMU (MPU6050) accelerometer, also it was aiming to develop a TUKF using triangular calibration algorithm that can be used in the field, outside of a lab, without the need for additional equipment. The testing results, which have been achieved using just a standard IMU, a custom-built IMU, as well as an aviation graded table, supported the practicality of the proposed method. Figures 4-17 to 4-22 show the orientations conditions (0^o-90^o) in the Y axis direction of the IMU sensor obtained by the Arduino plotter. As can be seen from the figures, when the movement direction in the Y direction the other axis will be in less movement and more stable. And in the state of no movement (0 g acceleration) as in figure 4-16, the three accelerometers are in more stability state as the straight lines of the axes data.

4.6. Comparison Of The Three Algorithms

The three supposed algorithm used in this dissertation are compared with respect to the scale factor calibration, bias errors and bias stability as shown in the table 4-9 shown below.

Table 4-9 Comparison Between The Three Proposed Algorithms

Proposed Algorithm	Scale Factor			Bias Errors			Bias Stability (μg)		
	X	Y	Z	X	Y	Z	X	Y	Z
Akima Interpolation	0.41%	0.42%	0.43%	0.024	0.026	0.025	2.216	2.22	2.23
ΣΔ Modulation	0.32%	0.33%	0.31%	0.011	0.014	0.012	1.34	1.23	1.12
TUKF	0.22%	0.24%	0.26%	0.017	0.015	0.014	0.116	0.12	0.18

As it can be seen from the table 4-9, the best algorithm for the sensor to be more stable is the third one (TUKF). In the third algorithm, the bias stability is the less in comparison with the other two proposed algorithms.

4.7. Chapter Summary

In this chapter, the design results of MEMS and NEMS three axes accelerometer with the results of the three algorithms of self-test and calibration were presented.

The first algorithm based on the Akima algorithm was used in conjunction with the genetic algorithm GA to calculate the voltages required to be applied on the test finger in the case of the fault of the fingers and spring. The required voltage is to be as Built In Self-Test (BIST) and stored in the lookup table.

The second algorithm used the Akima and genetic algorithms within the Sigma-Delta Modulator for the purpose of the noise removing based on the principle of the over sampling. All Brownian, electrical and quantization noise sources were well removed.

The third algorithm based on the Kalman Filter (KF) with modification to obtain the Transformed Unscented Kalman Filter (TUKF) for the three axes accelerometer MPU6050 with the triangulation on the output to achieve the best stability output for the X, Y, Z axes. The MPU6050 device was tested in the temperature range (-15^{o} C to 80^{o} C) to see the robustness of the algorithm used.

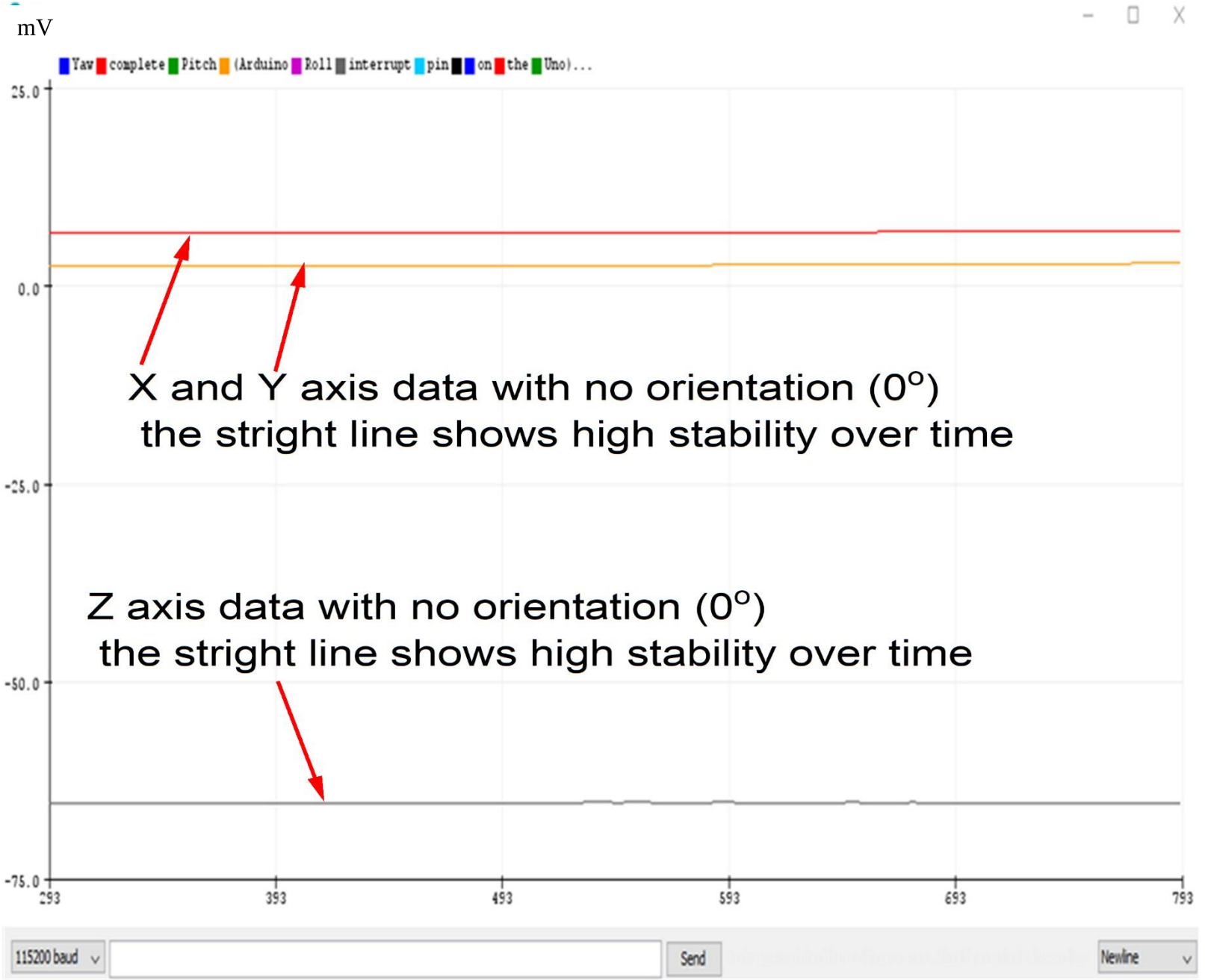

Figure 4-17 IMU 0º Orientation

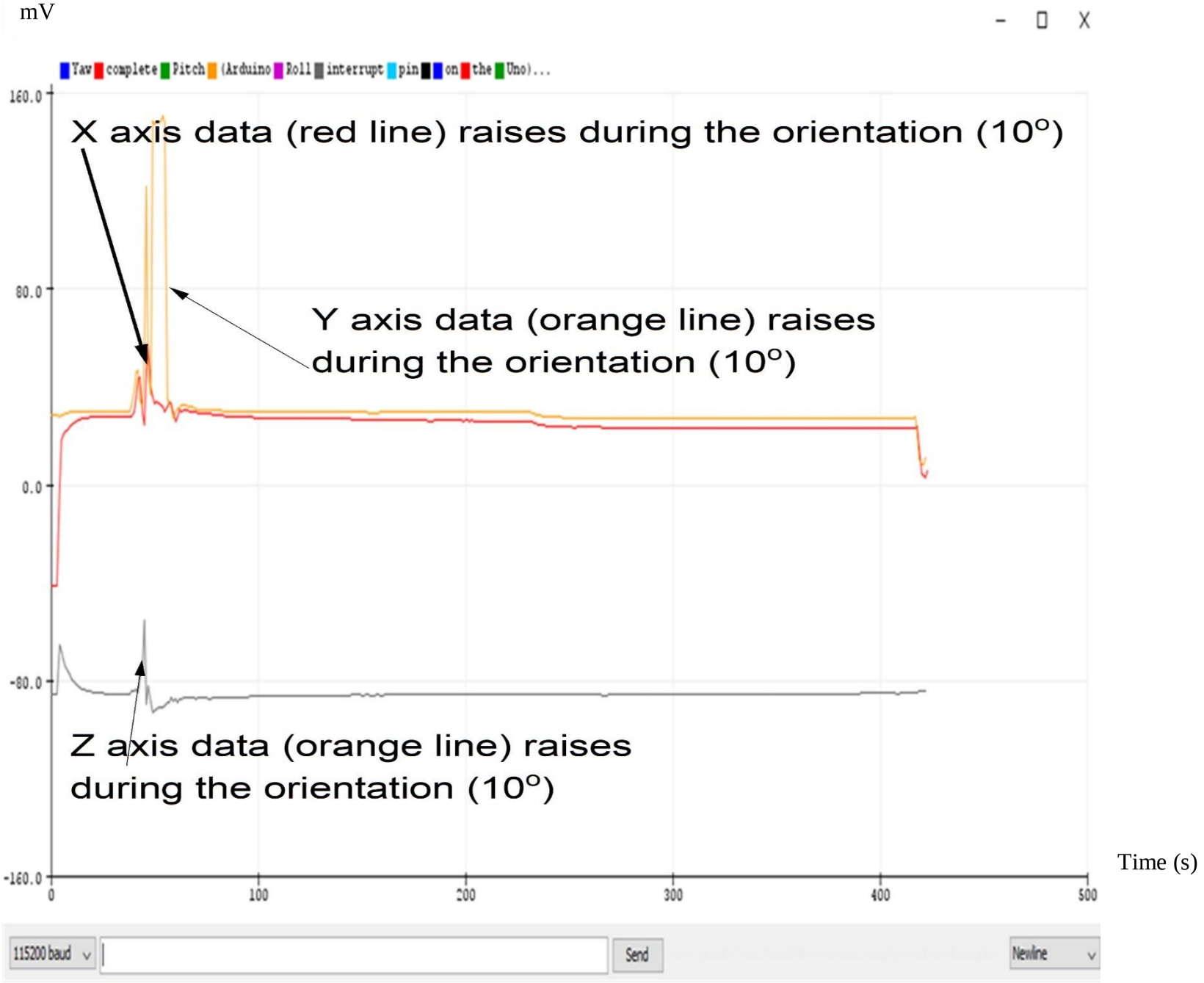

Figure 4-18 IMU 10° Orientation

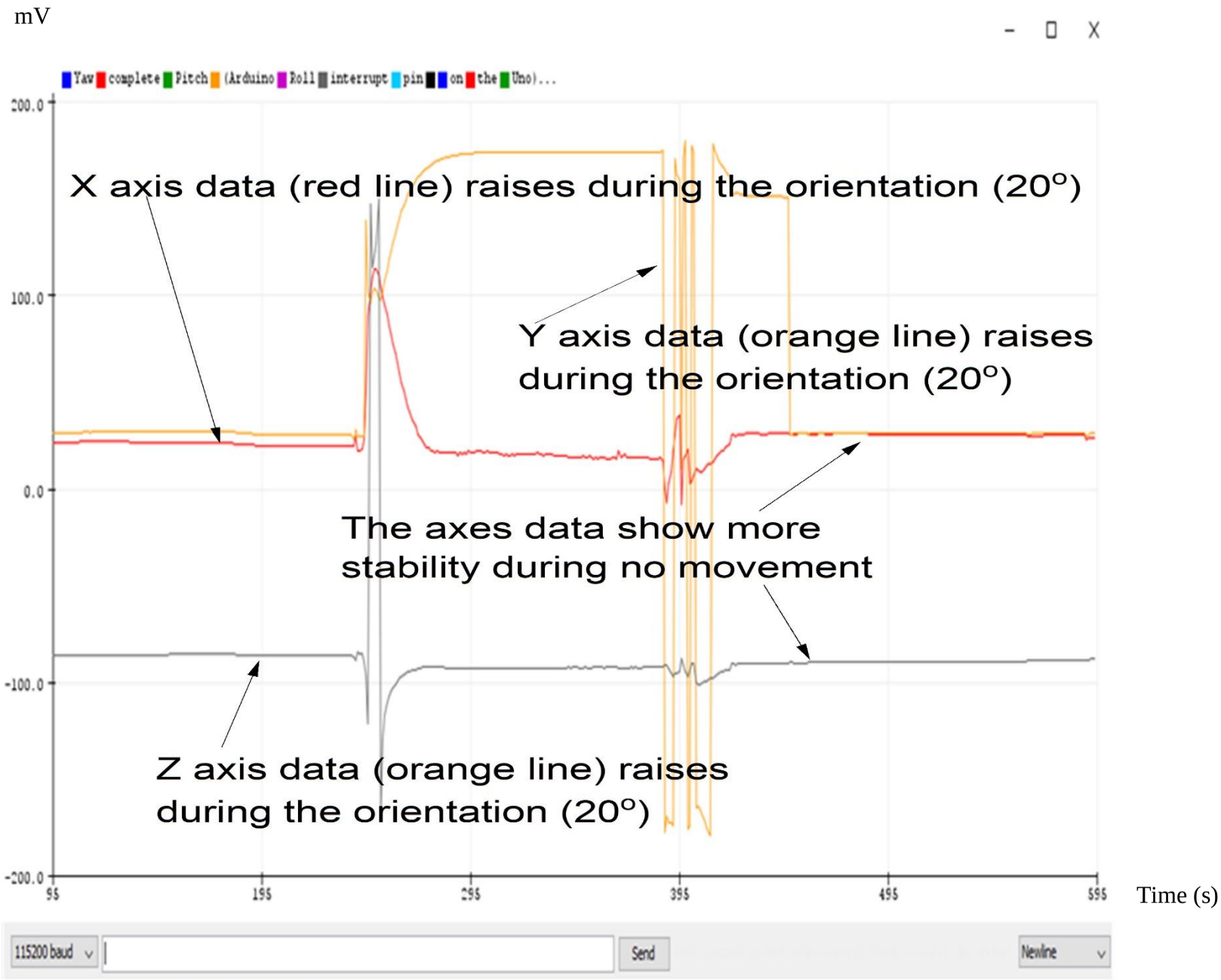

Figure 4-19 IMU 20° Orientation

Figure 4-20 IMU 30° Orientation

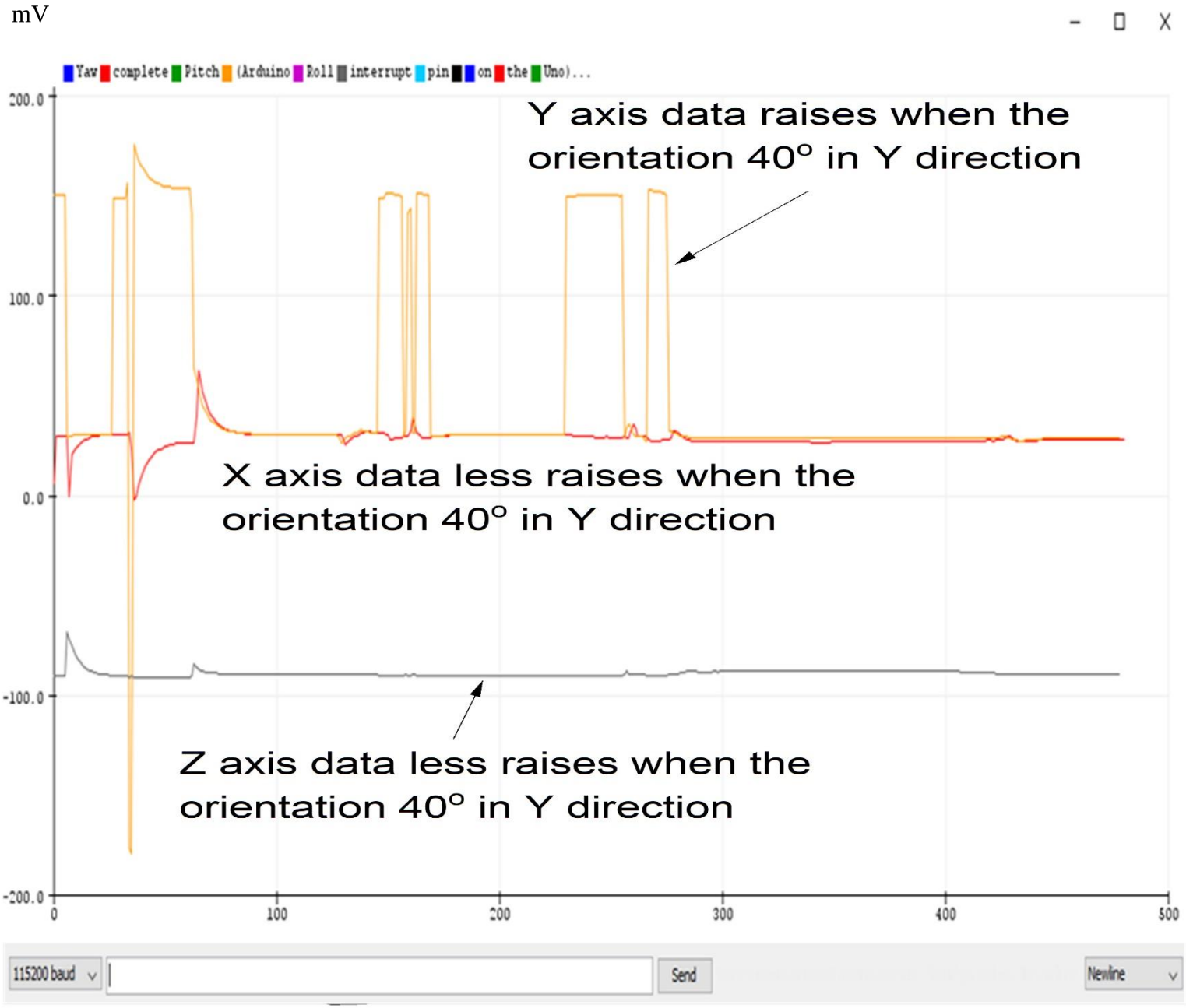

Figure 4-21 IMU 40° Orientation

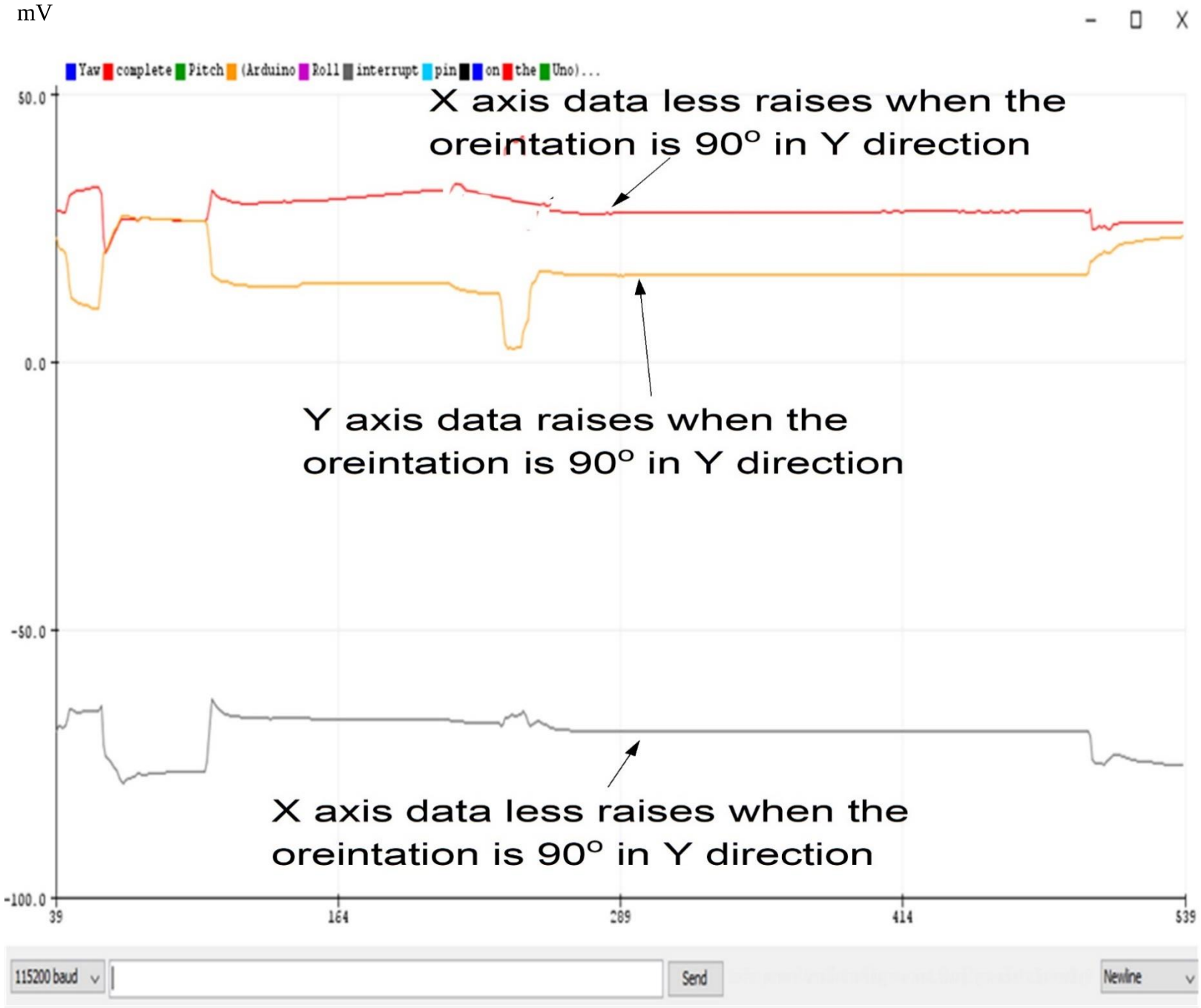

Figure 4-22 IMU 90° Orientation

CHAPTER FIVE

Conclusions and Suggested Future Work

Chapter Five: Conclusions and Suggested Future Work

5.1. Conclusions:

This chapter will summarize the important research findings and discuss their significance and contribution. It will also discuss study future research in the next section.

1. The proposed Akima interpolation algorithm that has been suggested along with other modifications could be a useful tool for eliminating overshoot in the MEMS output quickly fluctuating effectively.
2. The propose self-test and calibration method based on the Sigma-Delta modulator in conjunction with the Akima interpolation and Genetic Algorithm could be utilized in analog to digital converters for the MEMS signal after the self-test, calibration and noise removing resulted from MEMS and quantization utilizing the oversampling.
3. The lookup table used in the Akima interpolation could be a good tool for storing the number of Built In Self-Test (BIST) for the fault's compensation calculated by the GA.
4. The proposed Transformed Unscented Kalman Filter (TUKF) in conjunction with Delaunay Triangulation Algorithm can be a good estimator for the MEMS three axes accelerometer to give the best noise removing and stability. Allan deviation gave a good Angle Random Walk (ARW) and Bias Stability for this (TUKF) algorithm.
5. Any slight change in the sensing fingers or the spring dimensions and material properties could result in the MEMS proof mass displacement which makes a bias value and finally the output voltage.
6. The effect of the spring properties changes has more effect on the MEMS bias than the changes in the sensing fingers. Since the spring change has more effect on the MEMS resonance frequency, this frequency will drift as a result of the spring bias effect.

7. Each accelerometer axis movement can be achieved by the appropriate spring movement, and in the case of the three-accelerometer axis there should be three spring movement directions.

5.2. Suggestions for Future Works

1. Designing a six axes' MEMS accelerometer and gyroscope to be used as a single chip with self-test and calibration process.
2. Study the feasibility of the proposed algorithms to the gyroscope and magnetic field sensors.
3. Extending the Akima interpolation algorithm to be a more general tool for all types of accelerometers like piezoelectric, piezoresistive and thermal.
4. Designing a logical system model using the MEMS logic circuits for the self-test and calibrations utilizing the slope concept for the comparison of successive output points of the MEMS sensing element.

References

References

[1] A. S. Ahmed and Q. Al-Gayem, "Micro Accelerometer Built-In Self-Test and Calibration Using Genetic Algorithm and Interpolation Method," in *2022 IEEE International Conference on Semiconductor Electronics (ICSE)*, 2022: IEEE, pp. 49-52.

[2] A. K. Pandey, P. Pal, and L. Zentner, *Microactuators, Microsensors and Micromechanisms: MAMM 2022*. Springer Nature, 2022.

[3] G. S. Kondavitee, Y. S. Song, S. R. Karumuri, K. Guha, B. K. Kaushik, and A. Lay-Ekuakille, "Design, Fabrication and Measurement of Radio Frequency Micro-Electro-Mechanical Systems," *IEEE Open Journal of Nanotechnology*, 2023.

[4] J. Clark, "Self-calibration and performance control of MEMS with applications for IoT," *Sensors*, vol. 18, no. 12, p. 4411, 2018.

[5] M. Alzgool, Y. Tian, B. Davaji, and S. Towfighian, "Self-powered triboelectric MEMS accelerometer," *Nano Energy*, vol. 109, p. 108282, 2023.

[6] S. Scudero, A. D'Alessandro, L. Greco, and G. Vitale, "MEMS technology in seismology: A short review," in *2018 IEEE International Conference on Environmental Engineering (EE)*, 2018: IEEE, pp. 1-5.

[7] W. Liu *et al.*, "The High-Efficiency Design Method for Capacitive MEMS Accelerometer," *Micromachines*, vol. 14, no. 10, p. 1891, 2023.

[8] X. Wang, P. Zhang, and S. Ding, "A Study on the Harmonic Distortion of Seismic-Grade Sigma-Delta MEMS Accelerometers Using a Multiple Degree-of-Freedom Model," *Sensors*, vol. 23, no. 19, p. 8222, 2023.

[9] A. S. Ahmed and Q. Al-Gayem, "Self-test and calibration methods for micro electro-mechanical systems," *TELKOMNIKA (Telecommunication Computing Electronics and Control)*, vol. 21, no. 1, pp. 186-194, 2023.

[10] F. A. Mattoo, T. Nawaz, M. M. Saleem, U. S. Khan, and A. Hamza, "Deep Learning Based Multiresponse Optimization Methodology for Dual-Axis MEMS Accelerometer," *Micromachines*, vol. 14, no. 4, p. 817, 2023.

[11] H. E. Ahmed, S. Sahandabadi, Bhawya, and M. J. Ahamed, "Application of MEMS Accelerometers in Dynamic Vibration Monitoring of a Vehicle," *Micromachines*, vol. 14, no. 5, p. 923, 2023.

[12] C. Chircov and A. M. Grumezescu, "Microelectromechanical systems (MEMS) for biomedical applications," *Micromachines*, vol. 13, no. 2, p. 164, 2022.

[13] I. Frosio, F. Pedersini, and N. A. Borghese, "Autocalibration of triaxial MEMS accelerometers with automatic sensor model selection," *IEEE Sensors Journal*, vol. 12, no. 6, pp. 2100-2108, 2012.

[14] M. Gietzelt, K.-H. Wolf, M. Marschollek, and R. Haux, "Performance comparison of accelerometer calibration algorithms based on 3D-ellipsoid

fitting methods," *Computer methods and programs in biomedicine,* vol. 111, no. 1, pp. 62-71, 2013.
[15] M.-S. Kim, S.-B. Yu, and K.-S. Lee, "Development of a high-precision calibration method for inertial measurement unit," *International journal of precision engineering and manufacturing,* vol. 15, pp. 567-575, 2014.
[16] M. Jafari, M. Sahebjameyan, B. Moshiri, and T. Najafabadi, "Skew redundant MEMS IMU calibration using a Kalman filter," *Measurement science and technology,* vol. 26, no. 10, p. 105002, 2015.
[17] G. Yanning, H. Fei, D. Shaohe, M. Guangfu, and Z. Liangkuan, "Performance analysis of MEMS gyro and improvement using Kalman filter," in *2015 34th Chinese Control Conference (CCC)*, 2015: IEEE, pp. 4789-4794.
[18] X. Lu, Z. Liu, and J. He, "Maximum likelihood approach for low-cost MEMS triaxial accelerometer calibration," in *2016 8th International Conference on Intelligent Human-Machine Systems and Cybernetics (IHMSC)*, 2016, vol. 1: IEEE, pp. 179-182.
[19] L. Ye, Y. Guo, and S. W. Su, "An efficient autocalibration method for triaxial accelerometer," *IEEE Transactions on Instrumentation and Measurement,* vol. 66, no. 9, pp. 2380-2390, 2017.
[20] M. Narasimhappa, A. D. Mahindrakar, V. C. Guizilini, M. H. Terra, and S. L. Sabat, "MEMS-based IMU drift minimization: Sage Husa adaptive robust Kalman filtering," *IEEE Sensors Journal,* vol. 20, no. 1, pp. 250-260, 2019.
[21] G. Sheng, G. Gao, and B. Zhang, "Application of improved wavelet thresholding method and an RBF network in the error compensating of an MEMS gyroscope," *Micromachines,* vol. 10, no. 9, p. 608, 2019.
[22] F. Ghanipoor, M. Hashemi, and H. Salarieh, "Toward calibration of low-precision MEMS IMU using a nonlinear model and TUKF," *IEEE Sensors journal,* vol. 20, no. 8, pp. 4131-4138, 2020.
[23] X. Li *et al.*, "Closed-loop control for self-calibration of accelerometer achieved through integrated sensor and actuator system," *Microsystem Technologies,* vol. 27, no. 8, pp. 3025-3035, 2021.
[24] B. Fu *et al.*, "High-precision multicamera-assisted camera-IMU calibration: Theory and method," *IEEE Transactions on Instrumentation and Measurement,* vol. 70, pp. 1-17, 2021.
[25] X. Zhang *et al.*, "Low-cost inertial measurement unit calibration with nonlinear scale factors," *IEEE Transactions on Industrial Informatics,* vol. 18, no. 2, pp. 1028-1038, 2021.
[26] R. Li, C. Fu, W. Yi, and X. Yi, "Calib-Net: Calibrating the low-cost IMU via deep convolutional neural network," *Frontiers in Robotics and AI,* vol. 8, p. 772583, 2022.

[27] Z. Li, Z. Liu, and L. Zhao, "Improved robust Kalman filter for state model errors in GNSS-PPP/MEMS-IMU double state integrated navigation," *Advances in Space Research*, vol. 67, no. 10, pp. 3156-3168, 2021.
[28] X. Dong *et al.*, "Calibration Method of Accelerometer Based on Rotation Principle Using Double Turntable Centrifuge," *Micromachines*, vol. 13, no. 1, p. 62, 2021.
[29] T. Chen, G. Yang, Q. Cai, Z. Wen, and W. Zhang, "A novel calibration method for gyro-accelerometer asynchronous time in foot-mounted pedestrian navigation system," *Sensors*, vol. 22, no. 1, p. 209, 2022.
[30] C. Wang, Y. Cui, Y. Liu, K. Li, and C. Shen, "High-G MEMS Accelerometer Calibration Denoising Method Based on EMD and Time-Frequency Peak Filtering," *Micromachines*, vol. 14, no. 5, p. 970, 2023.
[31] O. Dürr, P.-Y. Fan, and Z.-X. Yin, "Bayesian Calibration of MEMS Accelerometers," *IEEE Sensors Journal*, 2023.
[32] Z. Zhai *et al.*, "A Scale Factor Calibration Method for MEMS Resonant Accelerometers Based on Virtual Accelerations," *Micromachines*, vol. 14, no. 7, p. 1408, 2023.
[33] D. Chen, X. Liu, L. Yin, Y. Wang, Z. Shi, and G. Zhang, "A ΣΔ closed-loop interface for a MEMS accelerometer with digital built-in self-test function," *Micromachines*, vol. 9, no. 9, p. 444, 2018.
[34] Y. Javed, M. Mansoor, and I. A. Shah, "A review of principles of MEMS pressure sensing with its aerospace applications," *Sensor Review*, vol. 39, no. 5, pp. 652-664, 2019.
[35] B. Vigna, P. Ferrari, F. F. Villa, E. Lasalandra, and S. Zerbini, *Silicon Sensors and Actuators: The Feynman Roadmap*. Springer Nature, 2022.
[36] A. S. Algamili *et al.*, "A review of actuation and sensing mechanisms in MEMS-based sensor devices," *Nanoscale research letters*, vol. 16, pp. 1-21, 2021.
[37] M. Huff, *Process variations in microsystems manufacturing*. Springer, 2020.
[38] V. Natarajan, S. Bhattacharya, and A. Chatterjee, "Alternate electrical tests for extracting mechanical parameters of MEMS accelerometer sensors," in *24th IEEE VLSI Test Symposium*, 2006: IEEE, pp. 6 pp.-199.
[39] F. Ibarra-Villegas, S. Ortega-Cisneros, F. Sandoval-Ibarra, J. Raygoza-Panduro, and J. Rivera-Domínguez, "Design of capacitive MEMS transverse-comb accelerometers with test hardware," *Superficies y vacío*, vol. 26, no. 1, pp. 4-12, 2013.
[40] S. Chen, Z. Yu, Y. Mou, and J. Shi, "Parametric Analysis of Electrostatic Comb Drive for Resonant Sensors Operating under Atmospheric Pressure," *Journal of Sensors*, vol. 2023, 2023.
[41] Á. Gómez Pau, R. Sanahuja Moliner, L. M. Balado Suárez, and J. Figueras Pàmies, "Built-In test of MEMS capacitive accelerometers for field

failures and aging degradation," in *Proceedings of XXVIIth Conference on Design of Circuits and Integrated Systems*, 2012, pp. 223-228.
[42] N. S. J. Naga, "Calibration of MEMS capacitive accelerometers using Electrical Stimulus BIST," ARIZONA STATE, ARIZONA STATE, 2014.
[43] X. Cui, C. Liu, G. Shi, and Y. Jin, "A new calibration method for MEMS accelerometers with genetic algorithm," in *2017 IEEE International Conference on Real-Time Computing and Robotics (RCAR)*, 2017: IEEE, pp. 240-245.
[44] M. Rasras, I. M. Elfadel, and H. D. Ngo, *MEMS Accelerometers*. MDPI AG, 2019.
[45] B. Boğa, "Modelling and noise analysis of closed-loop capacitive sigma-delta mems accelerometer," Middle East Technical University, 2009.
[46] S. E. Lyshevski, "Nano-and microscience, engineering, technology, and medicine series," *Nano and Molecular Electronics Handbook; CRC Press: Boca Raton, FL, USA*, 2007.
[47] L. Castañer, *Understanding MEMS: Principles and Applications*. John Wiley & Sons, 2015.
[48] D. Banks, *Microengineering, MEMS, and interfacing: a practical guide*. CRC press, 2006.
[49] S. E. Lyshevski, *MEMS and NEMS: Systems, Devices, and Structures*. CRC Press, 2018.
[50] N. Deb and R. Blanton, "Built-in self-test of MEMS accelerometers," *Journal of microelectromechanical systems*, vol. 15, no. 1, pp. 52-68, 2006.
[51] A. A. Balbola and W. Moussa, "Design, fabrication, and calibration of a Mems based sensing rosette for quantifying the influence of strain engineering on the piezoresistive coefficients," 2018.
[52] G. Hantos, D. Flynn, and M. P. Desmulliez, "Built-in self-test (BIST) methods for MEMS: A review," *Micromachines*, vol. 12, no. 1, p. 40, 2020.
[53] I. I. Basith, N. Kandalaft, and R. Rashidzadeh, "Built-in self-test for capacitive MEMS using a charge control technique," in *2010 19th IEEE Asian Test Symposium*, 2010: IEEE, pp. 135-140.
[54] I. I. Basith, N. Kandalaft, R. Rashidzadeh, and M. Ahmadi, "Charge-controlled readout and BIST circuit for MEMS sensors," *IEEE Transactions on Computer-Aided Design of Integrated Circuits and Systems*, vol. 32, no. 3, pp. 433-441, 2013.
[55] A. Dianat, A. Attaran, and R. Rashidzadeh, "Test method for capacitive MEMS devices utilizing pierce oscillator," in *2015 IEEE International Symposium on Circuits and Systems (ISCAS)*, 2015: IEEE, pp. 633-636.

[56] N. Dumas, Z. Xu, K. Georgopoulos, R. J. T. Bunyan, and A. Richardson, "Online testing of MEMS based on encoded stimulus superposition," *Journal of Electronic Testing*, vol. 24, pp. 555-566, 2008.
[57] S. Cui, L. Cui, Y. Du, S. Chai, and B. Zhang, "Calibration of MEMS accelerometer using kaiser filter and the ellipsoid fitting method," in *2018 37th Chinese Control Conference (CCC)*, 2018: IEEE, pp. 4679-4684.
[58] G. Panahandeh, I. Skog, and M. Jansson, "Calibration of the accelerometer triad of an inertial measurement unit, maximum likelihood estimation and Cramer-Rao bound," in *2010 International Conference on Indoor Positioning and Indoor Navigation*, 2010: IEEE, pp. 1-6.
[59] M. u. Hassan and Q. Bao, "A Field Calibration Method for Low-Cost MEMS Accelerometer Based on the Generalized Nonlinear Least Square Method," *Multiscale Science and Engineering*, vol. 2, pp. 135-142, 2020.
[60] Y. Sun and X. Xu, "Calibration of MEMS triaxial accelerometers based on the maximum likelihood estimation method," *Mathematical Problems in Engineering*, vol. 2020, pp. 1-10, 2020.
[61] R. Fontanella, D. Accardo, E. Caricati, S. Cimmino, and D. De Simone, "An extensive analysis for the use of back propagation neural networks to perform the calibration of MEMS gyro bias thermal drift," in *2016 IEEE/ION Position, Location and Navigation Symposium (PLANS)*, 2016: IEEE, pp. 672-680.
[62] H. Akima, "A new method of interpolation and smooth curve fitting based on local procedures," *Journal of the ACM (JACM)*, vol. 17, no. 4, pp. 589-602, 1970.
[63] L. Chang, B. Hu, A. Li, and F. Qin, "Transformed unscented Kalman filter," *IEEE Transactions on Automatic Control*, vol. 58, no. 1, pp. 252-257, 2012.
[64] G. Sobreviela-Falces *et al.*, "A navigation-grade MEMS vibrating beam accelerometer," in *2022 IEEE 35th International Conference on Micro Electro Mechanical Systems Conference (MEMS)*, 2022: IEEE, pp. 782-785.
[65] Y. Korkishko *et al.*, "Miniature Inertial Measurement Units IMU200 and IMU400 Based on FOG with MEMS-Accelerometers: Development and Studying of Characteristics," in *2022 29th Saint Petersburg International Conference on Integrated Navigation Systems (ICINS)*, 2022: IEEE, pp. 1-5.
[66] H. D. Gavcar, "A low-drift silicon MEMS resonant accelerometer," 2023.
[67] G. Liu *et al.*, "Combined Temperature Compensation Method for Closed-Loop Microelectromechanical System Capacitive Accelerometer," *Micromachines*, vol. 14, no. 8, p. 1623, 2023.

Appendix A

Experiment Setup Instruments

1- Arduino Microcontroller Board.
2- MPU6050 Sensor.
3- Laptop.
4- Orientation Board.
5- Oven Chamber.

Appendix B

$$\frac{(VB+VF)^2}{(do-x)^2}-\frac{(VB-VF)^2}{(d+x)^2}$$

$$=\frac{(VB+VF)^2(x+d)^2}{(x+d)^2(do-x)^2}-\frac{(VB-VF)^2(do-x)^2}{(x+d)^2(do-x)^2}$$

$$=\frac{(VB+VF)^2(x+d)^2-(VB-VF)^2(do-x)^2}{(x+d)^2(do-x)^2}$$

الخلاصة

إن خطأ الانحياز الصفري وخطأ عامل القياس في النظام الكهروميكانيكي الدقيق (MEMS) والنظام الكهروميكانيكي النانوي (NEMS)، ناتج عن عيوب فنية والتقادم في العمر. يمكن أن تتضرر دقة نظام الملاحة بالقصور الذاتي بشكل كبير من خلال القراءات الأولية دون المعايرة. لاستخدام مقياس التسارع ثلاثي المحاور MEMS، يلزم إجراء اختبار ذاتي ومعالجة معايرة.

ويجب أن يتم إنتاج هذه الأنظمة بموثوقية عالية لإنجاز المهمة المطلوبة التي تم إعدادها لها. ولذلك أصبح الاختبار الذاتي والمعايرة مسألة مهمة للباحث. في هذا العمل، تم اقتراح التصميم والمحاكاة وتنفيذ الأجهزة للاختبار الذاتي المدمج ومعايرة ثلاث خوارزميات وتقديمها لغرض المعايرة للتعويض عن الأخطاء والعيوب في MEMS وNEMS.

يتم تنفيذ هذه الخوارزميات الثلاثة المقترحة باستخدام برنامج COMSOL Multiphysics بالاشتراك مع MATLAB. تم أخذ القراءات العملية من خلال المتحكم الصغير Arduino و حساس MPU6050 وتمت البرمجة بلغة C.

استخدمت الخوارزمية الأولى المقترحة استيفاء Akima لجعل القراءات في حالة العطل أو الانحراف من عنصر الاستشعار أقرب إلى القراءات المعوضة المحسوبة بواسطة GA والمحفوظة في جدول البحث Lookup table. مفتاح هذه الخوارزمية هو الدالة المتعددة التعريف، وهي عبارة عن مجموعة من متعددات الحدود بدرجات لا تزيد عن ثلاث والتي يمكن تطبيقها على فترات زمنية أكبر بشكل متزايد بين النقاط المعطاة. باستخدام هذه التقنية، تبلغ أخطاء معايرة عامل القياس 0.41%، 0.42%، 0.43% للمحاور X، Y، Z على التوالي، في حين أن أخطاء التحيز هي 0.026، 0.025، 0.024 للمحاور X، Y، Z على التوالي. ويبلغ استقرار التحيز 2.216 µg و2.22 µg و2.23 µg للمحاور X وY وZ على التوالي.

استخدمت خوارزمية المعايرة المقترحة الثانية استيفاء Akima بالتزامن مع مُعدِّل Sigma-Delta (ΣΔ) للواجهة الرقمية. تم استخدام مبدأ المعاينة المفرطة لغرض إزالة مصادر الضوضاء المتعلقة بعنصر الاستشعار ودائرة التكميم. هذه المصادر هي الضوضاء البراونية، الناتجة عن الحركة العشوائية لجزيئات المادة في كتلة الإثبات واستشعار الأصابع، والتضخيم، والتبديل، والتكميم لتحسين الدقة الفعالة لجهاز القياس المستخدم في هذه الطريقة. يستقبل هذا النظام إشارة تناظرية ويخرجها كإشارة رقمية منفصلة. تشكل عمليات التصفية، وأجهزة أخذ العينات، وجهاز قياس الكميات الحد الأدنى. باستخدام هذه

التقنية، تبلغ أخطاء معايرة عامل القياس 0.32%، 0.33%، 0.31% للمحاور X، Y، Z على التوالي، في حين أن أخطاء التحيز هي 0.011، 0.014، 0.012 للمحاور X، Y، Z على التوالي. قيم استقرار التحيز هي 1.34 ميكروجرام، 1.23 ميكروجرام، 1.12 ميكروجرام للمحاور X، Y، Z على التوالي.

الخوارزمية الثالثة تعتمد على مرشح كالمان (KF) مع التعديل للحصول على مرشح كالمان غير المعطر (TUKF) لمقياس تسارع المحاور الثلاثة MPU6050 مع التثليث على الاخراج للحصول على أفضل مخرجات ثبات للمحاور X، Y، Z. تم استخدام مرشح كالمان المعدّل بالإضافة إلى تثليث ديلوناي ليكون بمثابة متتبع لمقياس التسارع ثلاثي المحاور. يتم إزالة التحيز والضوضاء بشكل جيد مع استقرار جيد. وتمت قراءة النتائج العملية باستخدام متحكم Arduino من مقياس التسارع MPU6050 في نطاق درجات الحرارة من (-15 درجة مئوية) إلى (80 درجة مئوية) مما أعطى متانة الخوارزمية المستخدمة لإظهار فعالية هذه الطريقة. باستخدام هذه التقنية، تكون أخطاء معايرة عامل القياس 0.22%، 0.24%، 0.26% للمحاور X، Y، Z على التوالي، في حين أن أخطاء التحيز هي 0.017، 0.0115، 0.014 للمحاور X، Y، Z على التوالي. يبلغ استقرار التحيز 0.116 ميكروجرام و0.12 ميكروجرام و0.18 ميكروجرام للمحاور X وY وZ على التوالي.

لذا وكما يتبين أن الخوارزمية الثالثة (باستخدام TUKF) هي الأفضل فيما يتعلق بنتائج أخطاء التحيز واستقرار التحيز.

جمهورية العراق
وزارة التعليم العالي والبحث العلمي
جامعة بابل / كلية الهندسة
قسم الهندسة الكهربائية

تقنيات دقيقة ـ للفحص الذاتي للأنظمة الكهروميكانيكية الدقيقة

اطروحة

مقدمة إلى جامعة بابل / كلية الهندسة وهي جزء من متطلبات الحصول على درجة الدكتوراه فلسفة في الهندسة / الهندسة الكهربائية / الكترونيك واتصالات

من قبل
أنور صباح أحمد شيال

باشراف
أ.د. قيس كريم عمران

١٤٤٥هـ ٢٠٢٣م